Global magneto-convection models of stars with varying rotation rate

Dissertation
zur Erlangung des mathematisch-naturwissenschaftlichen Doktorgrades

"Doctor rerum naturalium"

der Georg-August-Universität Göttingen

im Promotionsprogramm PROPHYS
der Georg-August University School of Science (GAUSS)

vorgelegt von

Mariangela Viviani

aus Cosenza, Italien

Göttingen, 2019

Betreuungsausschuss

Prof. Dr. Maarit J. Käpylä
Max-Planck-Institut für Sonnensystemforschung, Göttingen, Germany

Dr. Robert Cameron
Max-Planck-Institut für Sonnensystemforschung, Göttingen, Germany

Prof. Dr. Ansgar Reiners
Institut für Astrophysik, Georg-August-Universität Göttingen, Göttingen, Germany

Mitglieder der Prüfungskommision

Referent: Prof. Dr. Maarit J. Käpylä
Max-Planck-Institut für Sonnensystemforschung, Göttingen, Germany

Korreferent: Prof. Dr. Andreas Tilgner
Institut für Geophysik, Georg-August-Universität Göttingen, Göttingen, Germany

2. Korreferent: Prof. Dr. Paul Charbonneau
Département de Physique, Université de Montréal, Montréal, Canada

Weitere Mitglieder der Prüfungskommission:

Prof. Dr. Ansgar Reiners
Institut für Astrophysik, Georg-August-Universität Göttingen, Göttingen, Germany

Prof. Dr. Laura Covi
Institut für Theoretische Physik, Georg-August-Universität Göttingen, Göttingen, Germany

Prof. Dr. Stefan Dreizler
Institut für Astrophysik, Georg-August-Universität Göttingen, Göttingen, Germany

PD. Dr. Olga Shishkina
Max Planck Institute for Dynamics and Self-Organization

Tag der mündlichen Prüfung:

Contents

Summary

The solar magnetic field is mostly axisymmetric at the largest scale. Latitudinal dynamo waves propagate from mid-latitudes towards the equator, as can be seen, for example, from sunspot observations. Reproducing this pattern is one of the main demands that a numerical model of the solar dynamo has to satisfy.

One of the most common theories to explain the solar cycle is the $\alpha\Omega$ dynamo mechanism, that depicts dynamo action in the Sun as an interplay of differential rotation (Ω effect) and helical turbulence (α effect). As the rotation rate increases, the turbulence effects increase, hence the $\alpha-$effect increases. As a consequence, the dynamo moves from the $\alpha\Omega-$ regime to the α^2-regime, where the inductive effects from turbulence are the dominant source for the toroidal and poloidal components of the magnetic field. This is postulated to lead to the emergence of non-axisymmetric solutions, but the details on how this transition occurs are not yet clear. The aim of this project is to quantitatively study how and why the types of the dynamo solutions and their cyclicity change as a function of rotation rate, together with some other important governing system parameters.

In Section 5.1, we first compare semi-global models at increasing rotation rates: models covering $1/4$ of the full longitudinal extent and models covering the full longitude. We find that only when the longitudinal wedge assumption is relaxed, non-axisymmetric modes can develop and produce azimuthal dynamo waves. However, due to numerical constraints, our models lack the polar caps. We therefore expect that full-sphere models will show features more close to stellar observations, such as more dipolar magnetic fields at higher rotation, that cannot develop now because of the missing poles. We also find out that high enough resolution is necessary to reach the non-axisymmetric regime.

In the axisymmetric regime, we find two different kind of solutions: one oscillatory in the presence of a solar-like differential rotation, where the equator rotates faster than the poles, and the other one still oscillatory, but in combination with an anti-solar differential rotation profile, with the equator slower than the poles. The main difference between the two solutions is the migration direction of the magnetic field, equatorward in the first case and poleward in the second one. The solar-like solutions were already analyzed with the test-field method, hence, here we concentrate on the oscillating solution in the anti-solar differential rotation regime. In Section 5.2 we study the turbulent transport coefficients in the axisymmetric models with the test-field module and analyze the dynamo operating in this regime.

An important aspect of the model is the description of heat conduction in the convection zone, and the aim in this study was to make it as realistic as possible. The common approach is to prescribe it according to mixing-length theory, so that the depth of the convection zone is fixed. Recent local models have shown that, in a more realistic non-linear setup, where heat conduction is a function of temperature and density, the depth of the

convection zone can considerably vary, and the bottom of the domain can become sub-adiabatic. Thus, the actual extent of the convective layer cannot be determined a priori, but is an output result of the simulations. We therefore also investigate the nature of dynamo solutions using such a non-linear model in Section 5.3 by adopting Kramers opacity law and compare with the results of Section 5.1. The different form of heat transport affects the azimuthal dynamo wave propagation direction. Also, the transition point to the non-axisymmetric regime is shifted towards a higher rotation rate, moving the simulations transition closer to the observed one.

1 Introduction

Quinci rivolse inver' lo cielo il viso.
Dante Alighieri, Paradiso, I, 142, Divina Commedia

1.1 Sun and solar-like stars

The Sun is just one among the many magnetically active stars in the Universe. It has a special place only in our perspective, because its magnetic activity can directly influence life on our planet through what is called *space weather*: the solar magnetic activity can affect satellite communications and cause power grid failures through e.g., flares and coronal mass ejections (CME), but is also the source of stunning aurorae. The magnetic field of the Sun manifests itself on the solar surface in the form of dark spots, called sunspots, bright features, like faculae, and more explosive phenomena, such as flares and CME. Tracing the location of appearance of the sunspots in latitude and time (Figure 1.1), a cyclic pattern can be recognized. The spots appear first at mid-latitudes (±30°). Then,

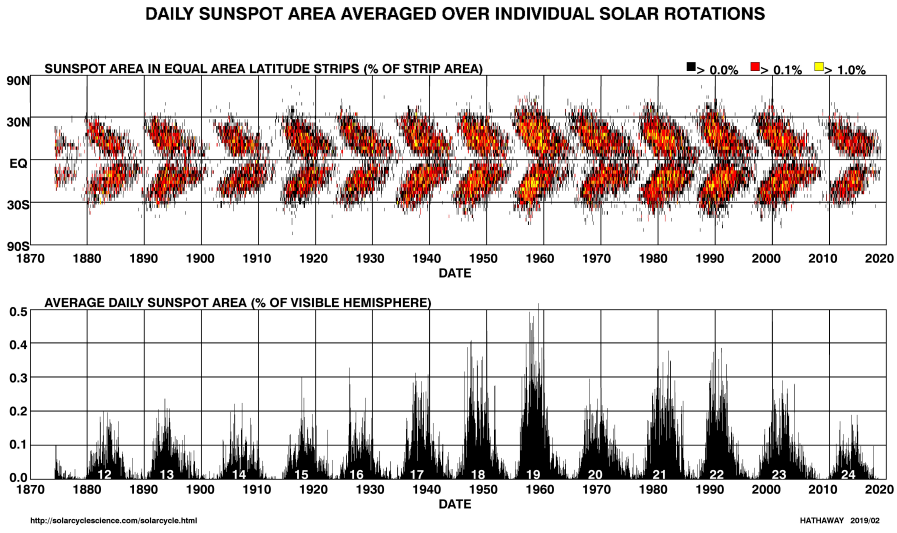

Figure 1.1: Sunspot area, averaged over each solar rotation, in latitude and time (top panel) and average daily sunspot area in the visible hemisphere (bottom panel). Courtesy of David Hathaway. http://solarcyclescience.com/solarcycle.html.

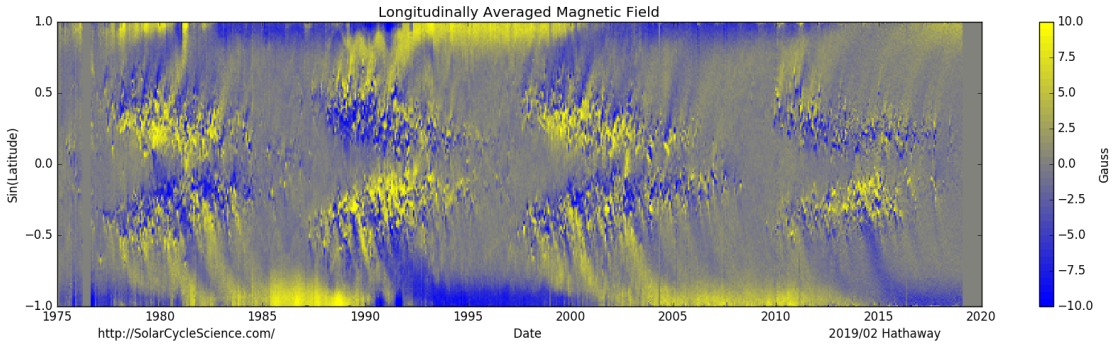

Figure 1.2: Longitudinally averaged radial magnetic field plotted in latitude and time at the solar surface. Courtesy of David Hathaway.

as the number of spots per day increases, they emerge progressively nearer to the equator, where their daily emergence rate reaches a minimum. This traces what is generally called the *butterfly diagram*, given the resemblance of the sunspots emergence pattern with butterfly wings (see, top panel in Figure 1.1), each wing pattern having a time span of 11 years. Figure 1.2 shows the longitudinally averaged radial magnetic field at the surface of the Sun over time. Comparing it with Figure 1.1, we see now that each consecutive wing carries the opposite polarity of magnetic field, forming a magnetic cycle with a period of roughly 22 years. These cycles thus constitute the Schwabe's (activity) and Hale's (magnetic) cycle, respectively, being the manifestations of the cyclic dynamo operating inside the solar convection zone.

1.1.1 Origin of the solar magnetic field

The present-day large-scale magnetic field of the Sun could be the relic of the nebula from which the Sun contracted. To verify it, we can estimate the magnetic field resulting from the contraction and evaluate the loss due just to resistive dissipation. The magnetic flux of the nebula is $\phi = BR^2$, where B is the average magnetic field and R the characteristic length. If we suppose the magnetic field to be "frozen" in the plasma, as in the ideal plasma approximation, then the flux is conserved. Also the mass of the contracting nebula has to be conserved, $M = \rho V \approx \rho R^3$. Then, following Moffatt (1978), we have $B \approx \phi\,(\rho/M)^{2/3}$ and, using the average values for the magnetic field in the Sun ($\sim 10^{-4}$ T) and the galactic field ($\sim 10^{-10}$ T), $10^6 \approx B_\odot/B_{\rm neb} \approx (\rho_\odot/\rho_{\rm neb})^{2/3}$. A compression factor of 10^{15} is necessary to justify the observed magnetic field ratio. The ratio $\rho_\odot/\rho_{\rm neb}$ is actually enough to support this explanation. If we now consider the characteristic dissipation time, $\tau_D = L^2/\eta$, where L is the characteristic length scale and η is the molecular magnetic resistivity, we can estimate the time that it would take the Sun to diffuse away its original magnetic field. We consider as L the solar radius, $R_\odot \approx 7 \cdot 10^8$ m, and $\eta \approx 1$ m^{2}s^{-1} for a gas constituted of hydrogen (Stix 2002). Then $\tau_D \approx 4.9 \cdot 10^{17}$ s $\approx 10^{10}$ yr, which is consistent with the the relic field hypothesis.

The solar convection zone, however, is in a highly turbulent regime, and we should account for the enhanced dissipation due to turbulence in the calculation. Thus, we consider the characteristic scale and velocity of granulation, $l \approx 10^3$ km and $u \approx 1$ km s^{-1},

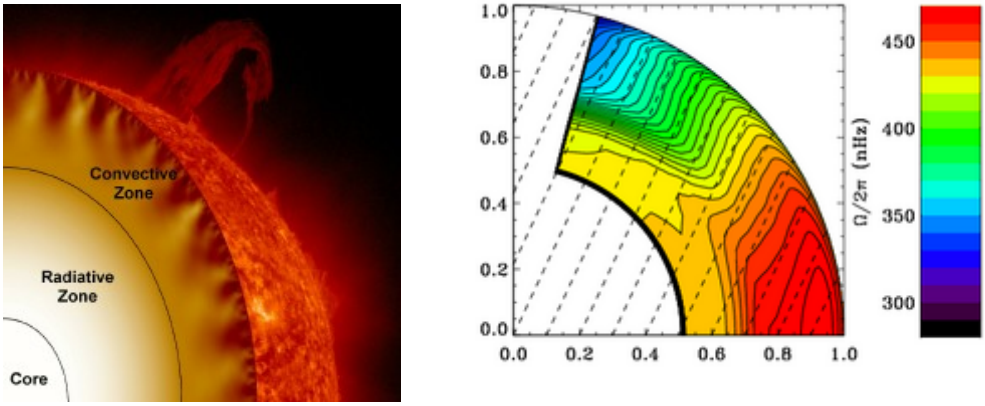

Figure 1.3: *Left panel*: internal structure of the Sun. Source: NASA. *Right panel*: solar differential rotation measured by GONG. Credits: GONG/NSO/AURA/NSF.

respectively. We can derive a typical viscosity $\nu \sim lu \approx 10^3$ km^2 s^{-1} $= 10^9$ m^2 s^{-1} (see, e.g., Stix 2002), finally arriving at a characteristic time of about $\tau_\nu \approx 4.9 \cdot 10^8$ s ≈ 15 yr. This estimate is consistent with the solar activity cycle, in which timescale the field has to be regenerated inside the Sun.

Even though the present large-scale magnetic field of the Sun could be the result of a fossil magnetic field, the almost regular polarity reversals cannot be explained by the fossil field hypothesis. The existence of a dynamo effect in the Sun is therefore necessary to explain the reorganization of the large-scale magnetic field and its cyclic nature.

1.1.2 Structure, convection zone and differential rotation in the Sun

The internal structure of the Sun is shown in the left panel of Figure 1.3. In the core, nuclear fusion burns hydrogen and produces helium and, in the radiative zone, energy is transported mainly through radiation. The convective zone constitutes the outer 30% of the solar radius and is the place where dynamo action occurs. In this region, the plasma is opaque to radiation and convection is transporting most of the energy. As a result of rotation and density stratification, the plasma in the convection zone is rotating differentially, as shown in Figure 1.3, right panel, from helioseismic measurements: the rotation is faster at the equator, with a period of 25 days, and slower at the poles, where it has a 30-days rotation period. Differential rotation (DR) constitutes one of the main ingredients of the solar dynamo. The convection zone is enclosed in between two layers of strong shear: the tachocline at the base and the near-surface shear layer at the top. Solar (and stellar) convection has many length and time scales: from the small scales of granulation near the surface (1 Mm and 10 min), to the larger scales of supergranulation deeper down (30 Mm and 1 day). Moreover, Bumba (1970) and Hathaway et al. (2013) reported also on the presence of giant cells (200 Mm and 1 month); the first using synoptic maps, the latter through supergranulation tracking. However, the analysis of Bogart et al. (2015) attributed such supergranular motions to the effect of magnetic fields or torsional oscillations. Moreover, the results of Hanasoge et al. (2012) show a lack of power at the length scales corresponding to giant cells' motions.

Moving up, the first visible layer of the solar atmosphere is the photosphere. From the photosphere, we can track the granulation and observe the sunspots. Some spectral lines, such as Ca II H & K, transition to an optically thin state higher up in the atmosphere. This region is called chromosphere. The emission in Ca II H & K is closely related to magnetic activity (Skumanich 1972, Stix 2002). The temperature increases with height in the chromosphere, and the chromospheric network, related to the granulation in the photosphere below, gradually disappears, until, in the transition region, the temperature sharply increases from 10^4 K to 10^6 K. Above the transition region, the solar corona starts. Stars emit X-ray radiation from the corona and also this emission is associated to magnetic activity (Wright et al. 2011, and references therein).

1.1.3 Solar-like stars

When talking about solar-like stars, we mean main-sequence stars with convective envelopes (F, G, K stars). Solar-like stars with convective envelopes also show latitudinal DR at the surface. The dependence on rotation rate has been reported to be slightly increasing (Reinhold and Gizon 2015) or slightly decreasing (Lehtinen et al. 2016) with rotation in photometric studies, while models (e.g., Kitchatinov and Rüdiger 1999) show a very weak dependence on rotation. On the other hand, asteroseismology studies (Benomar et al. 2018), inferred a much higher DR ($\approx$ 60% equator-mid-latitudes difference) in solar-like stars observed by *Kepler*.

Observations of other stars reveal that they also have activity cycles (see, e.g., Baliunas et al. 1995, Saar and Brandenburg 1999, Boro Saikia et al. 2018, Olspert et al. 2018) and that the cycle period can be related to their age and their rotation period (Skumanich 1972, Noyes et al. 1984b), with young, fast rotating stars having shorter activity cycles. Brandenburg et al. (1998) plotted the ratio between cycle and rotation frequency (ω_{cyc}/Ω) against magnetic activity, a proxy of which is the emission in Ca II H & K. It was shown that stars were clustering in "branches": one for old stars, called Inactive branch, one for younger stars, called Active branch. For both of them ω_{cyc}/Ω increases with activity. Later on, Saar and Brandenburg (1999) identified the Superactive branch for more active stars, in which ω_{cyc}/Ω decreases with increasing activity. However, when put in the stellar context, the Sun was more of an outlier, occupying the space between the Inactive and Active branches (Vaughan and Preston 1980, Noyes et al. 1984a). More recent observations, taking into account much longer time series, show that the Sun is now fitting among the other stars, and even question the existence of the Active branch, while the Inactive branch seems robust against different time series analysis method and extent of the data (see, e.g., Distefano et al. 2017, Boro Saikia et al. 2018, Olspert et al. 2018).

As mentioned in Section 1.1.2, another index to measure stellar magnetic activity is the X-ray fraction of stellar luminosity, quantified by the ratio $L_x/L_{\rm bol}$, where $L_{\rm bol}$ is the integrated luminosity. Like for the emission in Ca II H & K, the emission in X-ray depends on the rotation rate of the star. This is visible in Figure 1.4, where the rotation is represented by the Rossby number, Ro = $P_{\rm rot}/\tau$, with τ, the convective turnover time, determined through empirical relations and stellar evolution models, as an estimate of convective turbulence. For over one order of magnitude in Ro, the activity increases with decreasing rotation period, until it reaches the so-called "saturation regime" around Ro = 0.1, where the emission in X-rays remains roughly constant with rotation. The

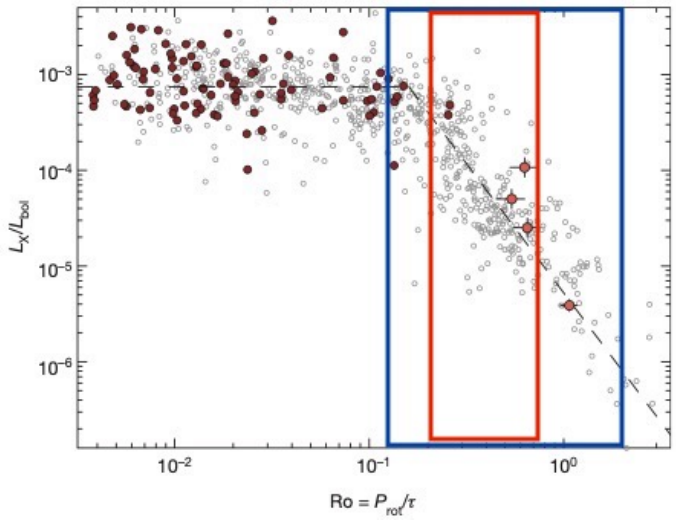

Figure 1.4: Ratio between luminosity in X-rays (L_x) and bolometric luminosity ($L_{\rm bol}$) as a function of the Rossby number (Ro = $P_{\rm rot}/\tau$), for solar-like stars (gray dots) and fully convective stars (red and orange dots). The red and blue boxes indicate the range in Rossby number explored in Strugarek et al. (2017) and Viviani et al. (2018), respectively. Reprinted and adapted by permission from Springer Nature: © Wright and Drake (2016).

term "saturation" refers to the saturation as a function of rotation period and, therefore, to the flat slope in the diagram. The $L_x/L_{\rm bol}$ − Ro relation is valid for stars with convective envelopes, represented in the figure by grey dots, but also for fully convective stars (Wright and Drake 2016), displayed with red and orange dots, suggesting a common mechanism for magnetic field generation in a wide range of spectral types. The red box in Figure 1.4 displays the range of Rossby numbers explored in the numerical simulations of Strugarek et al. (2017), as a representation of the state-of-the-art of numerical studies. In Section 5.1, we probed a larger parameters' regime and extended the examined range to cover the blue box in Figure 1.4. Even though some simulations are located in the region of large rotation periods corresponding to the Inactive (and Active) branch, the models in these studies do not show a positive slope in the $\omega_{cyc}/\Omega-{\rm Ro}^{-1}$ diagram. Their results lie in the region of the merged Active-Superactive population, called Transitional branch (Saar and Brandenburg 1999, Lehtinen et al. 2016, Distefano et al. 2017) and show a decreasing trend as a function of decreasing Rossby number. The only exception to the general trend in numerical results is the work of Guerrero et al. (2019) on partially convective stars with a convectively stable layer at the bottom. In these simulations, a positive trend is present for the cases in which the dynamo originates in the convection zone, while, for dynamos generating in the stable layer, their results are consistent with the other models. Their positive trend, though, is still located at too low Ro, far from the observed inactive population. The discrepancy between simulations and observations could depend on the convective turnover time and, hence, on the Rossby number, indicating that the models are still too laminar to reproduce stellar behaviours.

A thorough analysis and comparison between observations and simulations was performed in Olspert et al. (2018). In their analysis, only the Inactive branch appears robust

against all time series analysis method and length of the data set used, while stars that belonged to the Active and Superactive populations now form an indistinct cloud in the diagram. They also tried to explain the positive slope of the Inactive branch using scaling laws derived from the most common dynamo models, flux-transport (see, also, Jouve et al. 2010) and $\alpha\Omega$ dynamo (see, for example, Brandenburg and Subramanian 2005). For flux-transport dynamos, the cycle period is determined by the meridional circulation (Jouve et al. 2010). Numerical models show that the amplitude of meridional circulation decreases with increasing rotation, hence $\omega_{cyc} \propto \Omega^{-k}$ and $k > 0$. This means that the ratio ω_{cyc}/Ω will acquire a scaling proportional to Ω^{-k-1}. Hence, the slope predicted by flux-transport dynamos in the $\omega_{cyc}/\Omega - \mathrm{Ro}^{-1}$ is negative, which is opposite to the trend observed for the Inactive branch. For an $\alpha\Omega$ dynamo, the dependence of the cycle frequency is $\propto |\alpha\Delta\Omega|^{1/2}$ (Brandenburg and Subramanian 2005). Then, applying the scaling laws $\alpha \propto \Omega^a$ and $\Delta\Omega \propto \Omega^b$ (Olspert et al. 2018), we obtain that the observed slope, ν, is given by $\nu = +a/2 + b/2 - 1$. We can constrain b using observations (e.g., Reinhold and Gizon 2015, Lehtinen et al. 2016) or numerical models (e.g. Kitchatinov and Rüdiger 1999). In order to obtain $\nu > 0$, the dependence of the α effect on rotation must be unrealistically strong: $a \approx 3.3 - 4.3$. Therefore none of the two main paradigms is able to predict the positive slope of the Inactive population. In the case of an $\alpha\Omega$ model, one way to obtain a positive slope would be to admit a varying depth of the convective layer with rotation. This could be obtained with the development of a sub-adiabatic layer at the bottom of the convection zone, a result that has been reported on in recent numerical studies (e.g., Käpylä et al. 2017, Karak et al. 2018).

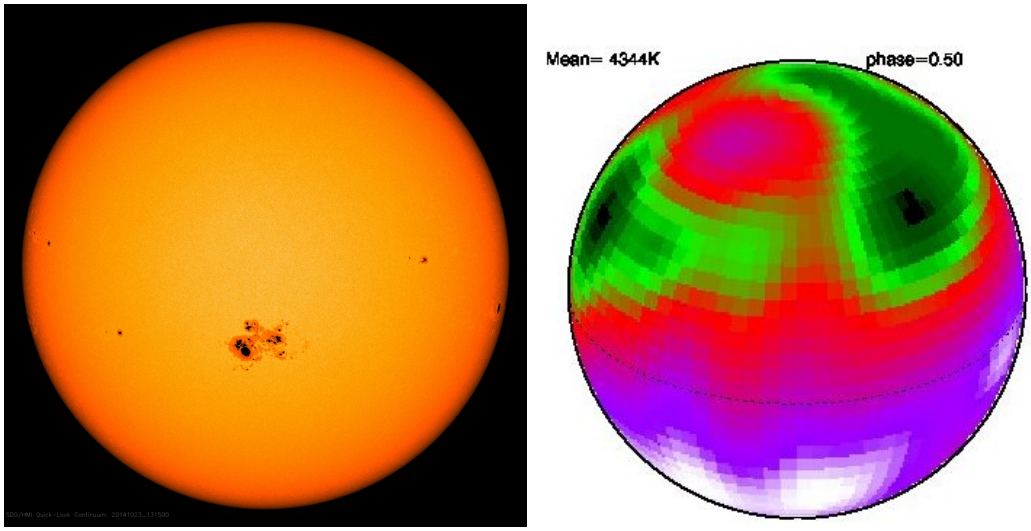

Figure 1.5: *Left panel*: sunspots on the solar surface in a continuum image from SDO/HMI. Image credit: NASA. *Right panel*: Doppler Imaging of an active star, II Peg, with a rotational period of roughly 6 days. Data from Lindborg et al. (2011).

Younger, faster rotating stars than the Sun show a higher level of surface magnetic activity and also a different magnetic field topology. For the Sun, spot emergence is restricted to middle to low latitudes and is rather axisymmetric with respect to the rotation axis (Figure 1.5, left panel), meaning that the spots do not show a preferential longitude

for their appearance (Pelt et al. 2006). On more active stars, the spots tend to appear at higher latitudes, or even in the polar regions, and form non-axisymmetric structures (with two main polarities in longitude) that migrate on the stellar surface at a different speed than the plasma (see, e.g., Berdyugina and Tuominen 1998, Lehtinen et al. 2016), constituting azimuthal dynamo waves (ADW). In their photometric study, Lehtinen et al. (2016) found that ADWs appear beyond a certain threshold in activity and detected mainly prograde waves, that is waves which are moving in the same direction as the rotation. However, also cases for retrograde waves (progressively lagging behind the rotating flow) or standing waves (non-migrating active longitudes) have been found (e.g., Berdyugina and Tuominen 1998). The magnetic field configuration on the surface of an active star, reconstructed using the Doppler imaging technique, is shown in Figure 1.5, right panel. The two darker (cooler) spots are close to the pole and separated by roughly 180^o degrees.

1.2 Numerical modeling

The variety and complexity of stellar behaviors calls for adequate numerical models which are able to reproduce solar and stellar observational results. A model capturing all the spatial and temporal scales present in the Sun, from the giant cells to the very small scales of granulation, is not feasible at the moment. Two types of modelling strategies are being used. The first one models local surface regions using radiative magnetohydrodynamics (RMHD, for a review, see Nordlund et al. 2009). The second one uses semi-global or global models neglecting RMHD and focusing on the deeper parts. In this thesis, we use a model belonging to the second category and, therefore, we review in more details these types of models.

Early models applied the mean-field concept (Steenbeck et al. 1966, Moffatt 1978, Krause and Rädler 1980, and also Section 2.2), where only the equation for the large-scale magnetic field or velocity field was solved for. The range of scales that can be resolved is much smaller than in a setup solving for the full magnetohydrodynamic (MHD) equations and, with suitable simplifications, some problems can be solved semi-analytically. As we discuss in Section 2.2.2.2, mean-field theory is the toolbox employed to discover Parker's oscillatory $\alpha\Omega$ dynamo mechanism, and it is still a widely used and applicable framework in modern astrophysics (see, e.g., Warnecke et al. 2018, and, also, Section 4.1 and Section 5.2). Mean-field theory relies on the parametrization of turbulent effects.

Another way to address the problem is to employ direct numerical simulations (DNS), where the MHD equations are solved employing explicit diffusivity and viscosity, albeit with much higher values than the ones for real objects, without any turbulence parametrization. The equations are solved in 2 or 3 dimensions, in Cartesian or spherical geometry. Especially in the 3D case, solving a system of non-linear equations is computationally expensive, therefore simplifications are often made, such as taking into account just a box in Cartesian geometry or a fraction of a sphere (wedge geometry), or stabilizing the numerical scheme by means of sub-grid scale (SGS) models that take care of the dissipation at small scales. If this is done at the grid scales, then these models are called implicit large-eddy simulations (ILES). SGS schemes can also parametrize some unresolved physical processes, such as heat flux (see, also, Chapter 4, Equation (4.5)). Even with the best supercomputers available at the moment we are not close to simulate the Sun realistically,

but have to resort to models using enhanced viscosity and diffusivity.

Simplifications can also be applied to the equations and not just to the extent of the simulation domain. One of the most stringent constraints on the timestep for numerical convection calculations is due to sound waves, which are pressure waves propagating with the speed of sound, c_s. The sound speed is increasing as a function of depth, while the convective velocity decreases. Hence, in the deeper parts, the timestep is constrained by c_s. Near the surface, however, the convective velocity increases and the Mach number, the ratio between the velocity and c_s, becomes close to one, indicating that the flow is transonic. Here, the convective velocity puts a restriction on the timestep. Capturing both these effects is very challenging for numerical schemes.

The simplest way to circumvent these restrictions consists in not allowing the density to vary. In this approximation, the fluid is incompressible ($\nabla \cdot \boldsymbol{U} = 0$), and, if the variations of density are considered just in the buoyancy term, we talk about Boussinesq approximation. Boussinesq flows are very common in nature and industrial applications but this approximation is not very suitable to stellar conditions. We note, however, that it is used for benchmarking different geo- and astrophysical codes (e.g., Christensen et al. 2001, Jackson et al. 2014).

A more widely used approximation in stellar convection is the anelastic approximation. In this case, temporal density variations are neglected, while density can vary spatially. The continuity equation, hence, becomes

$$\nabla \cdot (\overline{\rho}\boldsymbol{U}) = 0. \tag{1.1}$$

In the anelastic approximation, the thermodynamic variables are linearised around the adiabatic state. An infinite speed of sound is assumed, resulting in an instantaneous balancing of pressure perturbations. The expression (1.1) allows to simulate mildly stratified domains through variations of the reference density $\overline{\rho}$, while still neglecting the sound waves, and is one of the most used approximations for simulating planetary and stellar convection and dynamos (e.g., Brun et al. 2004, Jones et al. 2011, Smolarkiewicz and Charbonneau 2013, Duarte et al. 2016). The approximation breaks down near the surface, where the departures from the adiabatic state become large (Stix 2002).

Keeping sound waves could be useful to compare simulation results with observations or to put constraints on and compare results from different helioseismology (or asteroseismology) models. Then, the full continuity equation ($\partial_t \rho + \nabla \cdot (\rho \boldsymbol{U}) = 0$) has to be solved for. Different approaches can be used for keeping a reasonable timestep. For example, a much higher luminosity than the solar value can be used (Käpylä et al. 2013, Mabuchi et al. 2015). This leads to an increased, but still less than unity, Mach number and, therefore, to higher velocities. The rotational effects are then enhanced and it is necessary to neglect the centrifugal force, that would be much larger than in real stars. Unfortunately, this approach results in solar rotation profiles being still anti-solar with the solar rotation rate. Another technique to have high stratification is the reduced sound speed technique (Rempel 2005, Hotta et al. 2012), which consists in modifying the continuity equation by means of a parameter, ξ:

$$\frac{\partial \rho}{\partial t} = -\frac{1}{\xi^2} \nabla \cdot (\rho \boldsymbol{U}) \,. \tag{1.2}$$

Using values of ξ between 0 and 1, the Mach number scales by a factor of ξ but is still subsonic.

All these restrictions in modeling lead to discrepancies when comparing to observations. DNS of convective envelopes in solar-like stars can obtain anti-solar DR profiles, with faster poles and slower equator, for the solar rotation rate (e.g., Gastine et al. 2014, Käpylä et al. 2014, Karak et al. 2015). These results may also indicate that the Sun itself is in transition between these two DR regimes (Käpylä et al. 2014, Metcalfe et al. 2016). On the other hand, the numerical models of Guerrero et al. (2016, 2019), which include also a stable tachocline and SGS viscosity model, always show solar-like DR, although with, in general, lower values for the convective velocities. Also, as an effect of the SGS viscosity, the actual convective layer in the latter models is somewhat shallower than the real depth of the domain. In addition, the isocontours of DR in DNS are more aligned with the tangent cylinder than the isocontours actually observed through helioseismology (Schou et al. 1998), indicating that the flow is close to the Taylor-Proudman balance (Chandrasekhar 1961). Moreover, velocity spectra measurements from simulations reports far higher power at large scales (indicating the presence of giant cells) than the values inferred through helioseismic inversions (Hanasoge et al. 2012). The failure in reproducing solar-like DR, the almost cylindrical isocontours and the too high convective velocities in simulations constitute the elements of the *convective conundrum*.

It is currently not completely clear how to crack this conundrum. Even more, it is not yet fully observationally established how big the discrepancy between the models and the observations really is. Greer et al. (2015), using a different data analysis method than Hanasoge et al. (2012), arrived at a significantly higher upper limit for convective velocities at the giant cells scale. Also, numerical models have identified some pathways to reduce convective velocities. For example, Featherstone and Hindman (2016a,b) used the rotational influence on deep convection, while O'Mara et al. (2016) employed a decreased thermal conductivity. Finally, Hotta et al. (2015b) utilized high enough resolution to capture small-scale dynamo action.

One of the most used approaches to describe stellar convection is the mixing length theory (MLT, see also Section 3.1). In MLT, all the quantities are calculated using a characteristic length, that is the distance that a convective blob can travel in the convection zone before dissolving in its surroundings. MLT predicts the existence of giant cells, with a diameter of the order of the convection zone itself. Their existence, however, has not been observationally confirmed, especially in view of the results of Hanasoge et al. (2012), showing low power at the corresponding length scales in the horizontal velocity spectra. Non-local effects in MLT have been considered by e.g., Spruit (1997), and the relative MLT extension has been calculated by Brandenburg (2016), including a non-gradient term in the enthalpy flux (Deardorff 1966), proportional to entropy fluctuations. This term would drive upward flux even in a stably stratified medium. Moreover, the depth of the convectively unstable layer is reduced, meaning that giant cells might not be excited in such setups. Such subadiabatic layers have indeed been found by e.g., Käpylä et al. (2017) and Karak et al. (2018), the former through the use of Kramers-like opacity laws instead than MLT-motivated setups. In spherical geometry, both in the hydrodynamic and in the magnetohydrodynamic runs, Käpylä et al. (2019b) obtained reduced velocities at large length scales and isocontours for the DR less aligned with the tangent cylinder, but the differences were not sufficient to solve the conundrum.

Even with all the discrepancies with observations mentioned above, numerical models are our best chance to understand solar and stellar dynamos. New supercomputers

allow for more and more complex numerical simulations that, if not yet realistic, are increasingly reliable. The equatorward migration of the solar magnetic field (as shown in Figure 1.2) has been reproduced by many numerical models (Ghizaru et al. 2010, Käpylä et al. 2012b, Augustson et al. 2015), as well as the long-term variations in the solar cycle (e.g., Passos and Charbonneau 2014, Käpylä et al. 2016). These solar-like solutions, though, seem to emerge from imperfections in the rotation profiles (as discussed in Section 2.2.2.2). However, a broad agreement between different numerical codes using various approximations, was found in Augustson et al. (2019). They also pointed out the importance of keeping the same level of supercriticality of convection in simulations.

A proper stellar dynamo theory should be able to explain stellar magnetic fields in general and the Sun as a particular case. However, until recently, the Sun was considered as a "special" case in the context of stellar observations and, for long time, it was the only star for which we could have such detailed observations. Now that long-term observations are finally becoming available, they show increasing evidence of the Sun not being so special. Comparisons of modelling efforts versus observations are now emerging, and it is evident that the match to other solar-like stars' magnetic cycles is rather poor (see, e.g., Section 5.1). Even those mean-field models that provide a perfect fit to the Sun fail these tests (Olspert et al. 2018, and discussion therein).

1.3 Outline of the thesis

The aim of this thesis is to investigate the nature of the dynamo solutions and their variations as a function of rotation rate and heat conduction. We introduce dynamo theory in Chapter 2 and the theory of turbulent convection in Chapter 3. In Chapter 4 we examine the employed numerical methods. We discuss the dependence of the surface magnetic field configuration on rotation in Section 5.1, and the need of more realistic mechanisms for heat conduction in the convection zone in Section 3.2 and Section 5.3. In Section 5.2, we analyze in detail an axisymmetric simulation by means of the *test-field method*, introduced in Section 4.1.

2 Dynamo theory

Facesti come quei che va di notte,
che porta il lume dietro e sé non giova,
ma dopo sé fa le persone dotte.
Dante Alighieri, Purgatorio, XXII, 67-69, Divina Commedia

A more complete description of dynamo theory can be found, e.g., in Brandenburg and Subramanian (2005) and Charbonneau (2013). Here, we will only present a brief overview of the topics relevant to this thesis.

Most of the ordinary matter in the Universe is in the state of plasma, hot gas composed of ions and free electrons. If the collision rate between particles of the same species in the plasma is high enough so that it can be considered to be in thermal equilibrium (the particles' distribution function is well described by a Maxwell-Boltzmann distribution at all times), then we can use the fluid approximation to describe the plasma. This means that if the mean-free-path of particles in a fluid element is shorter than the extent of the fluid element itself, we can consider the collective behaviour of the particles as a fluid. In principle, we should write the fluid equations separately for electrons and ions, but if the charge separation is negligible, we can consider a one fluid model. This is established by comparing the length scale we are considering with the Debye length, $\lambda_\mathrm{D} = \left(\epsilon_0 k_B T / n q^2\right)^{1/2}$, i.e., the distance at which a charged particle is electrically screened by the other particles, where ϵ_0 is the permittivity of free space, k_B the Boltzmann constant, n the particle density and q the electric charge. Using the values of temperature ($T \approx 5000$ K) and particle density ($n \approx 10^{15}$ m^{-3}) at the base of the photosphere, the Debye length for particles in the Sun is approximately $\lambda_\mathrm{D} \sim 10^{-14}$ m, while the granulation scale is $l \approx 10^3$ km. At the bottom of the convection zone, the convection scales become larger, while λ_D gets shorter because of the increase in density n.

We can use the following set of MHD equations:

$$\frac{\partial \rho}{\partial t} + \nabla \cdot (\rho \boldsymbol{U}) = 0, \tag{2.1}$$

$$\frac{\mathrm{D}\boldsymbol{U}}{\mathrm{D}t} = -\frac{\nabla p}{\rho} + \boldsymbol{g} + \frac{\boldsymbol{J} \times \boldsymbol{B}}{\rho} + \frac{1}{\rho}\nabla \cdot 2\nu\rho\mathbf{S} + \boldsymbol{F}, \tag{2.2}$$

$$T\frac{\mathrm{D}s}{\mathrm{D}t} = -\frac{1}{\rho}\nabla \cdot \boldsymbol{F}^\mathrm{rad} + \frac{\mu_0 \eta}{\rho}\boldsymbol{J}^2 + 2\nu\mathbf{S}^2, \tag{2.3}$$

$$\frac{\partial \boldsymbol{B}}{\partial t} = \nabla \times (\boldsymbol{U} \times \boldsymbol{B} - \mu_0 \eta \boldsymbol{J}), \tag{2.4}$$

together with $\nabla \cdot \boldsymbol{B} = 0$ and an equation of state that relates the pressure p, the density ρ and the temperature T. Equation (2.1) is the continuity equation and describes the conservation of mass, where $\boldsymbol{U}$ is the velocity. Equation (2.2) is the equation for the conservation of momentum, where $\boldsymbol{g} = -GM\boldsymbol{r}/r^3$ is the gravitational acceleration, with G and M as the gravitational constant and the mass of the star, respectively. It includes also the Lorentz force $\boldsymbol{J} \times \boldsymbol{B}$, where $\boldsymbol{J}$ is the current density and $\boldsymbol{B}$ the magnetic field. The advective time derivative is:

$$\frac{\mathrm{D}f}{\mathrm{D}t} = \frac{\partial f}{\partial t} + (\boldsymbol{U} \cdot \nabla) f, \tag{2.5}$$

where f is a generic function. ν is the constant viscosity. S is the traceless rate-of strain tensor, that can be expressed as:

$$\mathsf{S}_{ij} = \frac{1}{2}\left(U_{i;j} + U_{j;i}\right) - \frac{1}{3}\delta_{ij}\nabla \cdot \boldsymbol{U}, \tag{2.6}$$

where δ_{ij} is the Kronecker delta and the semicolon expresses covariant derivative (Mitra et al. 2009). $\boldsymbol{F}$ includes other forces, such as the centrifugal or the Coriolis forces. In Equation (2.3) (conservation of internal energy), written in terms of the specific entropy s, $\boldsymbol{F}^{\mathrm{rad}} = -K\nabla T$ is the radiative flux, and K the radiative heat conductivity, which will be examined in more detail in Section 4.2. Equation (2.4) is the induction equation for the magnetic field $\boldsymbol{B}$, in which μ_0 and η are the magnetic permeability in vacuum and constant magnetic diffusivity. The equation is obtained using Maxwell's equations and Ohm's law ignoring the displacement currents, and assuming that motions are non-relativistic:

$$\boldsymbol{J} = \frac{\nabla \times \boldsymbol{B}}{\mu_0}. \tag{2.7}$$

2.1 Non-dimensional parameters

Non-dimensionalization of the set of Equations (2.1) to (2.4) results in a series of parameters that are useful to characterize the system under study. To this end, we define a characteristic velocity, U, and a characteristic length, L, in the system. A comparison in between advective ($(\boldsymbol{U} \cdot \nabla)\boldsymbol{U}$) and dissipative ($\nu\nabla^2\boldsymbol{U}$, resulting from S) terms in Equation (2.2) leads to the Reynolds number:

$$\mathrm{Re} = \frac{LU}{\nu}. \tag{2.8}$$

A high Reynolds number, as in the case of astrophysical objects (for the Sun, $\mathrm{Re} \approx 10^{13}$), indicates a highly turbulent regime. In Equation (2.4), the ratio of the term $\nabla \times (\boldsymbol{U} \times \boldsymbol{B})$ and the dissipative term, $\eta\nabla^2\boldsymbol{B}$, coming from $\nabla \times \eta\mu_0\boldsymbol{J}$ (considering constant magnetic diffusivity and Equation (2.7)), analogously gives the magnetic Reynolds number:

$$\mathrm{Rm} = \frac{LU}{\eta}. \tag{2.9}$$

Also here, a high magnetic Reynolds number is characteristic of (magnetized) astrophysical flows (for the convection zone of the Sun, $\mathrm{Rm} \approx 10^6 - 10^9$) and indicates that, if a

mechanism capable of producing magnetic field exists, the plasma can sustain this magnetic field against diffusion. The ratio of the two Reynolds numbers can tell us about the relative importance of viscosity and magnetic diffusion, defining, thus, the magnetic Prandtl number:

$$\mathrm{Pr_M} = \frac{\mathrm{Rm}}{\mathrm{Re}} = \frac{\nu}{\eta}. \tag{2.10}$$

Another important non-dimensional parameter is the thermal Prandtl number, that quantifies the relative importance of viscosity and thermal diffusivity:

$$\mathrm{Pr} = \frac{\nu}{\kappa} \tag{2.11}$$

In the Sun Pr ranges from 10^{-10} at the surface to 10^{-3} at the bottom of the CZ. Finally, in a rotating fluid, the ratio of the Coriolis force ($2\Omega \times \boldsymbol{U}$) and the advective term in Equation (2.2) defines the Coriolis number, or inverse Rossby number:

$$\mathrm{Co} = \frac{1}{\mathrm{Ro}} = \frac{2\Omega L}{U}. \tag{2.12}$$

A Coriolis number larger than unity tells us that rotational effects are more relevant to the dynamics of the system than convection; for the Sun Co $\approx 10^{-3} - 1$, (surface – bottom of CZ, e.g., Stix 2002).

2.2 Mean-field theory

Mean-field theory (Steenbeck et al. 1966, Moffatt 1978, Krause and Rädler 1980) is one of the most successful and widely used theories to explain stellar magnetism. It is based on the definition of suitable averages to determine the mean fields that will be used to describe the large-scale fields. Sometimes a further simplification is made by assuming the mean velocity field given - this is called the kinematic approach. The problem then reduces to solving the system for the mean magnetic field.

We can define an ensemble average so that all the quantities, f, can be written as the sum of a mean and a fluctuating component:

$$f = \overline{f} + f' \tag{2.13}$$

where $\overline{f'} = 0$. It is usually required that the Reynolds averaging rules apply for the averaging operator. The ensemble average is an averaging operation defined over many realizations of the same macrosystem, that is a number of microsystems sharing the same thermodynamic properties, such as temperature, density and pressure. In the case of the Sun, we have only one single realization and we witness just a brief instant of its life but, thanks to the ergodic theorem, we can substitute the ensemble average with a time or a spatial average. This is legitimate if also the time or length scales of the fluctuations (τ and λ, respectively) are smaller than the ones of the mean fields (t and l): $\lambda \ll l$ and $\tau \ll t$.

In the case of the Sun, considering the symmetry of its magnetic activity along the rotation axis, it makes sense to use the average in the longitudinal direction, ϕ, to define the mean fields: $\overline{f} = \langle f \rangle_\phi$. This average is meaningful as long as we are dealing with axisymmetric quantities, that is fields for which $\partial_\phi = 0$. We will encounter examples

when this averaging is not suitable anymore in Section 2.3 and Section 5.1. For the time being we will stick with this definition of mean fields and have a look at how these were used to explain dynamo action in the Sun. A much more detailed discussion on mean-field theory can be found, for example, in the books of Moffatt (1978) or Krause and Rädler (1980).

Applying the definition (2.13) to magnetic and velocity fields ($\boldsymbol{B} = \overline{\boldsymbol{B}} + \boldsymbol{b}'$ and $\boldsymbol{U} = \overline{\boldsymbol{U}} + \boldsymbol{u}'$) in the induction equation (2.4), we obtain the evolution equation for the mean magnetic field, $\overline{\boldsymbol{B}}$:

$$\frac{\partial \overline{\boldsymbol{B}}}{\partial t} = \boldsymbol{\nabla} \times \left(\overline{\boldsymbol{U}} \times \overline{\boldsymbol{B}} + \overline{\boldsymbol{u}' \times \boldsymbol{b}'} \right) - \boldsymbol{\nabla} \times \eta \boldsymbol{\nabla} \times \overline{\boldsymbol{B}} \tag{2.14}$$

The equation describes the dynamics of the mean magnetic field through $\overline{\boldsymbol{U}}$, $\boldsymbol{u}'$ and $\boldsymbol{b}'$. In the kinematic case there is no back-reaction of the magnetic field on the velocity field. In this case, the velocity (Equation (2.2)) and magnetic field (Equation (2.4)) evolution equations are decoupled. The fluctuating magnetic field is the only other unknown and, in principle, we should solve the corresponding equation, obtained subtracting Equation (2.14) from the equation for $\boldsymbol{B} = \overline{\boldsymbol{B}} + \boldsymbol{b}'$ in Equation (2.4):

$$\frac{\partial \boldsymbol{b}'}{\partial t} = \boldsymbol{\nabla} \times \left(\boldsymbol{u}' \times \overline{\boldsymbol{B}} + \overline{\boldsymbol{U}} \times \boldsymbol{b}' \right) + \nabla \times \left(\boldsymbol{u}' \times \boldsymbol{b}' - \overline{\boldsymbol{u}' \times \boldsymbol{b}'} \right) - \boldsymbol{\nabla} \times \eta \boldsymbol{\nabla} \times \boldsymbol{b}' \tag{2.15}$$

An additional simplification is assuming locality in space and time, and write the term involving the fluctuating magnetic and velocity fields, the turbulent electromotive force (EMF), $\overline{\mathcal{E}} = \overline{\boldsymbol{u}' \times \boldsymbol{b}'}$, as a function of $\overline{\boldsymbol{B}}$ and its spatial derivatives:

$$\overline{\mathcal{E}}_i = a_{ij} \overline{B}_j + b_{ijk} \frac{\partial \overline{B}_j}{\partial x_k} + ... \tag{2.16}$$

The tensors a_{ij} and b_{ijk} are functions of $\overline{\boldsymbol{U}}$ and $\boldsymbol{u}'$. It is convenient to separate the tensors $\boldsymbol{a}$ and $\boldsymbol{b}$ in their symmetric and anti-symmetric parts and obtain the following expression for the turbulent EMF:

$$\overline{\mathcal{E}} = \boldsymbol{\alpha} \cdot \overline{\boldsymbol{B}} + \boldsymbol{\gamma} \times \overline{\boldsymbol{B}} - \boldsymbol{\beta} \cdot \left(\nabla \times \overline{\boldsymbol{B}} \right) - \boldsymbol{\delta} \times \left(\nabla \times \overline{\boldsymbol{B}} \right) - \boldsymbol{\kappa} \cdot \left(\nabla \overline{\boldsymbol{B}} \right)^{(s)} + ... \tag{2.17}$$

where $\boldsymbol{\alpha}$ is the symmetric part of $\boldsymbol{a}$ and can generate magnetic field (α effect), $\boldsymbol{\gamma}$ is the anti-symmetric part of $\boldsymbol{a}$ and represents turbulent transport (turbulent pumping). $\boldsymbol{\beta}$ is a turbulent diffusion, while $\boldsymbol{\delta}$, in combination with other generating effects, can also generate magnetic field through, for example, $\boldsymbol{\Omega} \times \boldsymbol{J}$ (or Rädler) effect (Rädler 1969), where $\boldsymbol{\Omega}$ is the angular velocity. The physical interpretation of $\boldsymbol{\kappa}$ is still unclear, but it is generally treated as a diffusion term. The term $(\nabla \boldsymbol{B})^{(s)}$ indicates the symmetric part of the tensor $\nabla \boldsymbol{B}$.

Now, all we have to do is to solve the system for the 27 unknown tensorial components in Equation (2.17). The most often used approached employs analytic or semi-analytic calculations of the coefficients using closure methods. An example of which is the second order correlation approximation (SOCA) or, equivalently, first order smoothing approximation (FOSA): it involves neglecting all the moments higher than the second order, like the second term on the right hand side of Equation (2.15). In order for this assumption to

be valid, the term $\nabla \times \left(\boldsymbol{u}' \times \boldsymbol{b}' - \overline{\boldsymbol{u}' \times \boldsymbol{b}'}\right)$ must be smaller than the time derivative, $\partial_t \boldsymbol{b}'$, or the diffusive term contained in $\boldsymbol{\nabla} \times \eta \boldsymbol{\nabla} \times \boldsymbol{b}'$. These translate in a condition on the Strouhal number, defined as $\mathrm{St} = \tau_c U k_f$ (where τ_c is the correlation time of turbulence and k_f the convection scale) or on Rm: $\min\{\mathrm{St}, \mathrm{Rm}\} \ll 1$. Although none of the two conditions is valid in astrophysical systems (for which $\mathrm{Rm} \gg 1$ and $\mathrm{St} \approx 1$), the results derived with FOSA seem to be accurate enough and have been confirmed in DNS (see, e.g., Käpylä et al. 2006, and references therein).

Another way of determining the turbulent transport coefficients is provided by DNS simulations, that solve for the mean fields and fluctuations, the electromotive force itself being an output, combined with data analysis tools to infer the coefficients (e.g., Brandenburg and Sokoloff 2002, Racine et al. 2011, Simard et al. 2013, Schrinner et al. 2005, 2007, Warnecke et al. 2018).

2.2.1 Toroidal and poloidal fields

The following representation will turn out to be useful for the description of FOSA results and possible mechanisms to sustain stellar magnetic fields.

Under the assumption of axisymmetry, a vector field, $\boldsymbol{F}$, can be decomposed in a poloidal, $\boldsymbol{F}_\mathrm{p}$, and a toroidal, $\boldsymbol{F}_\mathrm{t}$, field (Chandrasekhar 1961, Krause and Rädler 1980), so that:

$$\boldsymbol{F} = \boldsymbol{F}_\mathrm{t} + \boldsymbol{F}_\mathrm{p}, \quad \boldsymbol{F}_\mathrm{t} = F_\phi \hat{\boldsymbol{e}}_\phi = \boldsymbol{r} \times \nabla \mathcal{U}, \quad \boldsymbol{F}_\mathrm{p} = F_\mathrm{r} \hat{\boldsymbol{e}}_\mathrm{r} + F_\theta \hat{\boldsymbol{e}}_\theta = \boldsymbol{r} \mathcal{V} + \nabla \mathcal{W}. \tag{2.18}$$

The rightmost expression for $\boldsymbol{F}_\mathrm{t}$ and $\boldsymbol{F}_\mathrm{p}$ is valid also without the axisymmetric assumption. $\mathcal{U}$, $\mathcal{V}$ and $\mathcal{W}$ are scalar superpotentials and can be expanded in spherical harmonics as:

$$\mathcal{F} = \sum_{l,m} \tilde{\mathcal{F}}_l^m(r)\, \Upsilon_l^m(\theta, \phi), \quad \Upsilon_l^m(\theta, \phi) = P_l^{|m|}(\cos\theta)\, e^{im\phi}, \tag{2.19}$$

with $\Upsilon_l^m(\theta, \phi)$ being the spherical harmonic of degree (l, m), $P_l^{|m|}$ the Legendre polynomial of degree l, and $\tilde{\mathcal{F}}_l^m(r)$ the coefficients of the expansion that can be computed if we know the scalar superpotential $\mathcal{F}$ at a specific radius r:

$$\tilde{\mathcal{F}}_l^m(r) = \int_0^{2\pi} \int_0^{\pi} \mathcal{F}(r, \theta, \phi)\, \Upsilon_l^m(\theta, \phi) \sin\theta \, \mathrm{d}\theta \mathrm{d}\phi. \tag{2.20}$$

2.2.2 Mean-field dynamos

Under the FOSA assumption, and in the case of homogeneous and isotropic turbulence, the EMF can be written as

$$\overline{\mathcal{E}} = \alpha \overline{\boldsymbol{B}} - \beta \nabla \times \overline{\boldsymbol{B}} \tag{2.21}$$

where α and β are now scalars and, in the case of no mean flow ($\overline{\boldsymbol{U}} = 0$), depend only on the fluctuating velocity $\boldsymbol{u}'$. Their form in the kinematic case is:

$$\begin{aligned} \alpha &= -\frac{\tau_c}{3} \overline{\boldsymbol{\omega} \cdot \boldsymbol{u}'}, \quad \boldsymbol{\omega} = \nabla \times \boldsymbol{u}' \\ \beta &= \frac{\tau_c}{3} \overline{\boldsymbol{u}'^2}. \end{aligned} \tag{2.22}$$

α is proportional to the kinetic helicity and, therefore, related to the cyclonic turbulence described by Parker (Parker 1955a,b), while β is a turbulent diffusivity and can be regarded as a significant enhancement to the molecular diffusivity:

$$\eta_{\mathrm{T}} = \eta + \beta. \tag{2.23}$$

2.2.2.1 α^2 dynamo

Introducing α and β in Equation (2.14) and separating the magnetic field in toroidal and poloidal fields as described in Section 2.2.1 and considering the axisymmetric case, still considering $\overline{\boldsymbol{U}} = 0$, we obtain a system of two equations:

$$\begin{aligned} \frac{\partial \overline{\boldsymbol{B}}_t}{\partial t} &= \alpha \left(\nabla \times \overline{\boldsymbol{B}}\right)_p - \eta_{\mathrm{T}} \nabla^2 \overline{\boldsymbol{B}}_t \\ \frac{\partial \overline{\boldsymbol{B}}_p}{\partial t} &= \alpha \left(\nabla \times \overline{\boldsymbol{B}}\right)_t - \eta_{\mathrm{T}} \nabla^2 \overline{\boldsymbol{B}}_p \end{aligned} \tag{2.24}$$

in which the poloidal field acts as a source term for the toroidal field and the toroidal field is the source term in the poloidal field equation. This system allows for exponentially growing solutions and shows that, even in the absence of a mean flow, an isotropic homogenous turbulent flow with kinetic helicity can generate and uphold dynamo action. As only the α effect is responsible for generating the toroidal magnetic field from the poloidal one and viceversa, the set of equations Equation (2.24) is called as an α^2 dynamo.

Magnetic fields in fast rotating stars, for which helical turbulence is thought to play a dominant role over differential rotation (gradient of a mean flow), are believed to be generated by an α^2 dynamo or, in the case when the DR is not totally negligible, by an $\alpha^2\Omega$ dynamo. Next, we turn to discuss the role of the differential rotation.

2.2.2.2 $\alpha\Omega$ dynamo

To include the DR, we define $\overline{\boldsymbol{U}} = \overline{\boldsymbol{U}}_t = (0, 0, \Omega r \sin\theta)$. Then, we insert the expression in the induction equation for $\overline{\boldsymbol{B}}_t$ and $\overline{\boldsymbol{B}}_p$:

$$\begin{aligned} \frac{\partial \overline{\boldsymbol{B}}_t}{\partial t} &= \nabla \times \left(\overline{\boldsymbol{U}}_t \times \overline{\boldsymbol{B}}_p\right) + \alpha \left(\nabla \times \overline{\boldsymbol{B}}\right)_p - \eta_{\mathrm{T}} \nabla^2 \overline{\boldsymbol{B}}_t \\ \frac{\partial \overline{\boldsymbol{B}}_p}{\partial t} &= \alpha \left(\nabla \times \overline{\boldsymbol{B}}\right)_t - \eta_{\mathrm{T}} \nabla^2 \overline{\boldsymbol{B}}_p \end{aligned} \tag{2.25}$$

This time, there is an additional source term in the equation for $\overline{\boldsymbol{B}}_t$ that describes the conversion of the poloidal field into toroidal one through DR, a process that is referred to as Ω-effect. If this term dominates over the α effect in generating the toroidal field, the model is called $\alpha\Omega$ dynamo (Parker 1955a,b).

Figure 2.1 depicts a sketch of the model. The poloidal magnetic field is sheared by differential rotation, generating thus toroidal magnetic field. Cyclonic turbulent convection pushes the blobs of gas, and the magnetic field with it, up and down in the stratified CZ. The rising blobs expand and the toroidal magnetic field lines are twisted by the Coriolis force, generating poloidal magnetic field. The process of generating poloidal field from

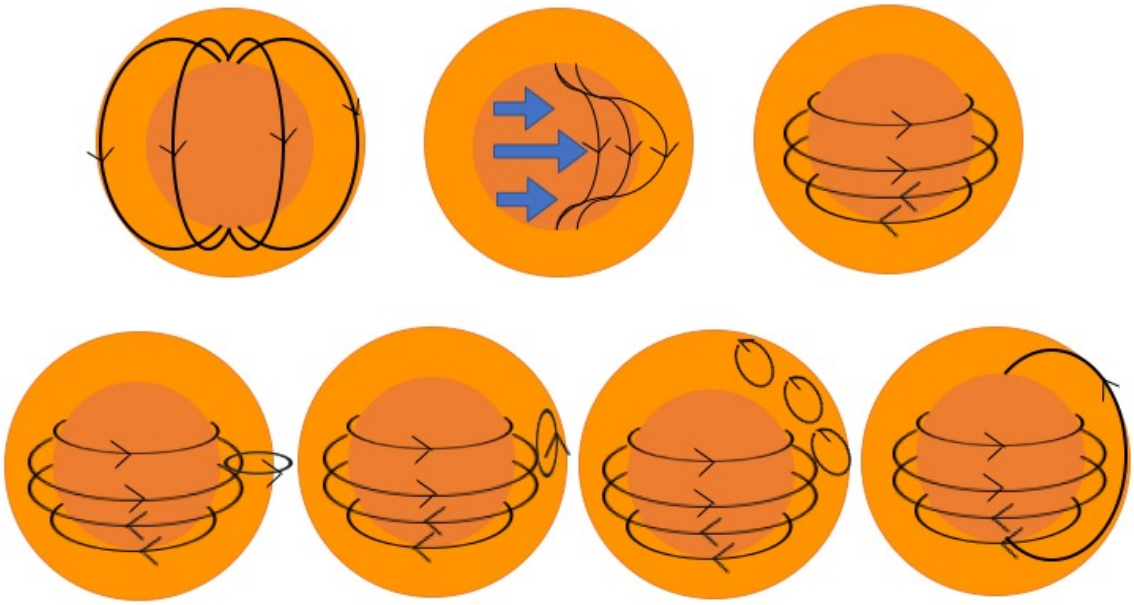

Figure 2.1: Schematic representation of $\alpha\Omega$ dynamo model.

the toroidal one takes the name of α-effect. The sign of the α-effect is the same in each hemisphere, so that the poloidal loops merge as a result of turbulent reconnection and add up, creating poloidal magnetic field. The generated poloidal field has the opposite sign with respect to the original one, hence, two such cycles are needed to obtain again a poloidal field in the original configuration, completing the dynamo cycle.

As for the α^2 dynamo in Section 2.2.2.1, the helical nature of the α-effect is able to overcome Cowling's anti-dynamo theorem (Cowling 1933). The α-effect breaks the axisymmetry on short time and length scales, creating an electromotive force with an azimuthal component.

The appearance of spots at progressively lower latitudes in the course of the solar cycle can also be explained by $\alpha\Omega$ dynamo as a latitudinal dynamo wave. The direction of propagation of the wave (poleward or equatorward) is given by the Parker-Yoshimura sign rule (Yoshimura 1975):

$$\boldsymbol{\xi}(r,\theta) = -\alpha\hat{\boldsymbol{e}}_\phi \times \nabla\boldsymbol{\Omega}, \tag{2.26}$$

where the relevant component of the shear is the radial one ($\nabla_r\Omega$). However, helioseismology results (e.g., Schou et al. (1998) and also, Fig 1.3, right panel) have shown that the solar DR does not vary as much in radius as it does in latitude, and it decreases slightly from the surface to the bottom of the CZ. To have an equatorward dynamo wave with a positive radial shear, the α-effect must be negative in the northern hemisphere and positive in the southern hemishpere. In simulations, however, the sign of the α-effect is positive (negative) in the northern (southern) hemisphere (see, e.g., Warnecke et al. 2018), which would lead to a poleward wave. Nonetheless, numerical models reproduce the equatorward propagation. A reversal in the sign of α in radius could invert the propagation direction. Such reversals have been found by Duarte et al. (2016), as a consequence of weaker density stratification in the interior and faster rotation. Alternative explanations

for the equatorward propagation in simulations, in spite of the wrong sign of α, are localized regions of negative shear at mid-latitudes (e.g., Warnecke et al. 2014), non-linear feedback of the magnetic field on the velocity field (e.g., Augustson et al. 2015), or a return meridional flow (e.g., Choudhuri et al. 1995). The latter possibility is explored further in the Section 2.2.2.3.

2.2.2.3 Babcock-Leighton models

An alternative and more empirical scenario to the turbulent dynamo theory presented in Sections 2.2.2.1 and 2.2.2.2 are the "Babcock-Leighton dynamos", developed from the works of Babcock (1961) and Leighton (1969). These models gained popularity after helioseismology uncovered the internal DR of the Sun: the theory of Parker waves to explain the equatorial propagation of sunspots was shaken by the weak radial gradient of Ω and its wrong sign in the bulk of the CZ. Moreover, the results of Vainshtein and Cattaneo (1992) and Cattaneo and Hughes (1996) indicated a catastrophic quenching of the α-effect ($\propto \mathrm{Rm}^{-1}$) in the nonlinear regime. Because of the α-quenching, the large-scale magnetic field would not be able to reach dynamically significant values in high-Rm objects, leading to the "death" of the dynamo.

In these models (see, e.g., Dikpati and Charbonneau 1999), the toroidal field is stored below the base of the convection zone, where a strong shear layer, the tachocline, is known to reside, and rises buoyantly in the form of thin flux tubes, once it has reached a certain threshold in strength. During their rise or when they appear at the surface, the Coriolis force imposes a tilt in the north-south direction and thus generates poloidal field. The thin flux tubes appear as sunspot pairs, in which leading and following spots have the opposite polarity. Meridional circulation advects the magnetic field of the following spot polarity towards the poles, while turbulent magnetic diffusivity leads to polarity cancellation of the leading spots towards the equator. Magnetic field of the opposite sign with respect to the already existing poloidal field accumulates at the poles until the poloidal field changes its sign. The field at the poles is then pushed down to the tachocline by meridional circulation. In the tachocline it is amplified again by shear. An equatorward meridional circulation at the bottom of the CZ is responsible for the equatorward migration of the emerging flux tubes at the surface. The origin of this explanation lies in the systematic tilt observed in sunspots emergence: when a spot pair appears at the surface, the following spot emerges with a certain angle with respect to the leading spot, this angle depending on the latitude of emergence of the leading spot (Joy's law, Hale et al. 1919). This effect is not related to turbulence at all, and is working at a much larger scale of the expanded flux tubes. The effect of Joy's law in the model is parametrized similarly to its turbulent counterpart in mean-field models. In this sense, Babcock-Leighton dynamos are a subclass of mean-field models, where the α-effect occurs only near the surface and for which the cycle period is set by the meridional circulation (Jouve et al. 2010).

Early models relying on the Babcock-Leighton mechanism prescribed a single cell meridional circulation (see e.g., Choudhuri et al. 1995, Dikpati and Charbonneau 1999) and relied on the helioseismic measures of it just below the surface, enclosing it in the interval of $6 - 20$ m/s (Duvall 1979, Hathaway 1996, Zhi-Chao et al. 2018). DNS results, however, show multiple cells and also helioseismology inferences suggest that the return flow may be less deep than what was expected (Hathaway 2011). Therefore, recent

models (see, e.g., Jouve and Brun 2007) include multi-cellular pattern for the meridional circulation and obtain shorter activity periods.

A recent update on this model from Cameron and Schüssler (2017) considers the radial magnetic field at the surface and the integrated toroidal flux in the CZ. Hence, the location and the structure of the toroidal field do not need to be specified. Moreover, this model includes a parametrization of turbulent diffusion and of convective pumping pointing in the negative radial direction.

2.3 Azimuthal dynamo waves in observations and simulations

We already mentioned in Section 1.1 that spots tend to appear on the same location in longitude in active stars, in what are called active longitudes. These active longitudes also migrate with respect to the surface, constituting azimuthal dynamo waves (ADW).

ADWs are predicted by mean-field theory in the rapid rotation regime (Krause and Rädler 1980). To to demonstrate what ADWs formally are, we decompose the mean magnetic field $\overline{\boldsymbol{B}}$ in complex modes:

$$\overline{\boldsymbol{B}} = \sum_m \hat{\mathbf{B}}, \quad \hat{\mathbf{B}} = C^m \mathrm{e}^{im\phi+(\lambda-i\Omega)t} \tag{2.27}$$

where C^m is a time-independent axisymmetric complex vector field. We can rewrite the exponential to highlight the different contributions:

$$\mathrm{e}^{im\phi+(\lambda-i\Omega)t} = \cos(m\phi - \Omega t)\,\mathrm{e}^{\lambda t} + i\sin(m\phi - \Omega t)\,\mathrm{e}^{\lambda t} \tag{2.28}$$

Employing this decomposition in the evolution equation for $\overline{\boldsymbol{B}}$, only one mode will grow. The case $m = 0$ is the axisymmetric mode, and oscillations are either damped (if the growth rate $\lambda < 0$) or amplified ($\lambda > 0$). The cases for which $m \neq 0$ correspond to ADWs rigidly rotating with velocity Ω/m, where Ω is the angular velocity of the wave. The direction of propagation can be prograde ($\Omega < 0$) or retrograde ($\Omega > 0$), and it is also possible to find a reference frame in which $\Omega = 0$. In the latter case, we will have a standing wave.

Dynamo solutions that show migrating pattern with respect to the rotation of the fluid that can be related to an ADW have been detected in the numerical studies of Käpylä et al. (2013) and Cole et al. (2014). In Section 5.1, we identified a transition from axisymmetric dynamo modes at moderate rotation to non-axisymmetric ones at faster rotation, similar to the observed transition, albeit the values are off, with the simulation transition happening at a lower rotation rate than the observed one.

For these models, a mean-field averaging procedure as described in 2.2 is not appropriate anymore to describe the large-scale magnetic field, as an average over longitude would cancel the contribution from the non-axisymmetric field. A decomposition in spherical harmonics, as shown in Section 2.2.1, is more convenient. In this case, the contribution to the axisymmetric field will be contained in the coefficients of Υ_l^0, while the contribution of the non-axisymmetric field will result from the coefficients of Υ_l^m, $m \geq 1$.

3 Theory of turbulent convection

Poca favilla gran fiamma seconda.
Dante Alighieri, Paradiso I, 34, Divina Commedia

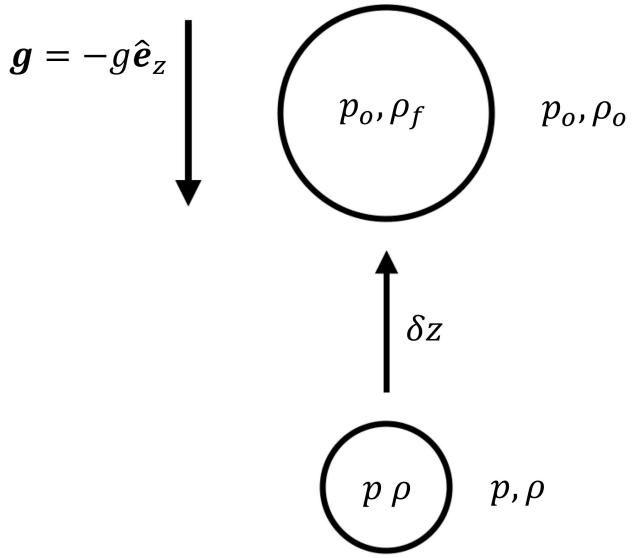

Figure 3.1: Schematic representation of the convective instability.

Heat can be transmitted by conduction, convection and radiation. In the high collisionality limit, ions and electrons will statistically have the same temperature and conduction is a very inefficient mechanisms for heat transfer. Stellar convection zones are opaque to radiation and the stratification is close to the adiabatic one (see, e.g. Stix 2002), hence radiation is also not efficient. Therefore, the most effective way to transport energy is by convection. However, a complete description of fully developed turbulence, which is ubiquitous in convection zones of cosmic objects, is not possible, because of their high Re.

The criterion for convective instability was derived first by Schwarzschild (1906) in a simplified system. Here, we follow the derivation of Stix (2002). A simple model of convection is sketched in Figure 3.1. Suppose we have a fluid subject to gravity in the negative z direction: $\boldsymbol{g} = -g\hat{\boldsymbol{e}}_z$. A parcel of fluid at position z, initially at equilibrium with its surroundings at pressure p and density ρ, is perturbed and displaced by a distance δz. We assume that the rise is fast enough so that there is no exchange of heat during the process (adiabatic displacement), but also slow enough that the pressure inside and outside the blob is the same at every instant (the blob will expand during the rise). To

have an instability, the density of the fluid element at $z + \delta z$, ρ_f, must be less than the density outside, ρ_o, so that the blob continues to rise. In the case $\rho_o < \rho_f$ the parcel sinks again and the instability is damped. If the displacement δz is infinitesimal, we can expand:

$$0 > \rho_f - \rho_o \cong \left[\left(\frac{d\rho}{dz}\right)_a - \frac{d\rho}{dz}\right]\delta z, \tag{3.1}$$

where the subscript a stands for adiabatic. We assume the fluid being a perfect gas, $p = \rho T\mathcal{R}/\mu$, where p is the pressure, T the temperature, $\mathcal{R}$ the gas constant and μ is the mean molecular weight. The pressure is the same inside and outside the fluid element, and in the CZ, μ is a function of p and T. However, we will neglect the variations of molecular weight, because the timescales we are considering are short in comparison to the time the star spends on the main sequence, during which it is mainly burning hydrogen and enriching in helium. Then, we can substitute the perfect gas law in Equation (3.1) and obtain:

$$\frac{dT}{dz} < \left(\frac{dT}{dz}\right)_a \tag{3.2}$$

The expression above is the Schwarzschild's criterion for convective instability and states that for convection to set in, the temperature gradient must be steeper than the adiabatic temperature gradient. Other forms of the Schwarzschild's criterion are:

$$\begin{aligned} \frac{\partial s}{\partial z} < 0 \quad &\text{(unstable)}, \quad \text{or} \\ \nabla > \nabla_{\rm ad} \quad &\text{(unstable)} \\ \text{where} \quad &\nabla = \frac{\partial \ln T}{\partial \ln p} \end{aligned} \tag{3.3}$$

and $\nabla_{\rm ad} = 1 - 1/\gamma$ is the adiabatic gradient. A convectively unstable layer is one in which the specific entropy decreases with height or, equivalently, one in which ∇ is steeper than the adiabatic gradient. When considering also the variations in the molecular weight, μ, Equation (3.3) becomes the Ledoux criterion (Ledoux 1947): $\nabla > \nabla_{\rm ad} + \nabla_\mu$, where $\nabla_\mu = \partial \ln\mu / \partial \ln p$. The effect of the gradient in μ is stabilizing, as the heavier elements will move towards the center.

An evaluation of Equation (3.3) using solar values leads to $\nabla - \nabla_{\rm ad} \sim 0.1 - 10^{-8}$ (from the top to the bottom of the CZ, Stix 2002), which means that the temperature gradient can be only slightly higher than the adiabatic one for convection to carry most of the flux. Therefore, the stratification in the convection zone can be considered nearly adiabatic and simplified theories can be used to handle the problem.

3.1 Mixing length theory (MLT)

A simplified theory describing convection is the mixing length theory (MLT), developed in the context of stellar convection by Vitense (1953) and Böhm-Vitense (1958). MLT considers stellar convection zones in hydrostatic equilibrium and defines all the relevant quantities, such as convective velocities and temperature gradients, through the mixing length. The mixing length is the distance that a parcel of fluid can travel before it mingles

with its surroundings, releasing its heat or absorbing heat from the medium. In Vitense (1953), this characteristic length, l, is assumed to be proportional to the pressure scale height, $H_p = -(\partial_r p/p)^{-1}$:

$$l = \alpha_{\rm MLT} H_p, \tag{3.4}$$

where $\alpha_{\rm MLT}$ is the mixing length parameter, that has to be calibrated through observations. Values of the order of 1 have been proposed for $\alpha_{\rm MLT}$ (see e.g., Stix 2002). The goal now is to calculate the amount of flux carried by convection:

$$F_{\rm conv} = v_c \rho c_p \Delta T. \tag{3.5}$$

v_c is the convective velocity, hence $v_c\rho$ is the mass flux, and c_p is the specific heat at constant pressure. The temperature gradient can be obtained considering small displacements, δr (Stix 2002):

$$\Delta T = \left[\left(\frac{dT}{dr}\right)' - \frac{dT}{dr}\right]\delta r = \frac{T}{H_p}\left(\nabla - \nabla'\right)\delta r, \tag{3.6}$$

where the primes denote the gradients of quantities related to the parcel rise. The convective velocity can be obtained considering the acceleration of the parcel due to buoyancy and, by substituting the perfect gas equation, we have:

$$v_c^2 \approx \frac{g\delta}{H_p}\left(\nabla - \nabla'\right)\delta r^2, \tag{3.7}$$

where $\delta = 1 - \partial\left(\ln\mu\right)/\partial\left(\ln T\right)$ considers the variations in mean molecular weight. We recall, however, that variations in μ are considered negligible in our case. We can approximate δr by half a mixing length, $l/2$, and consider another $1/2$ factor to account for losses during the process. Hence, the convective flux is:

$$F_{\rm conv} \approx \rho c_p \left(\frac{g\delta H_p}{8}\right)^{1/2} \left(\nabla - \nabla'\right)^{3/2} \frac{T\alpha_{\rm MLT}^2}{2}. \tag{3.8}$$

MLT has been very successful in predicting the existence of convective cells of different sizes in the CZ, namely granulation and supergranulation. Its construction, though, assumes that convection is driven at all scales. Therefore, it also predicts the existence of convective cells of the size of the entire CZ (giant cells). Helioseismic inferences (Hanasoge et al. 2012), however, show only very little power at such large length scales, marking the incompleteness of this simple theory. But exactly because of its simplicity, people have been reluctant to completely abandon MLT and rather tried to extend and improve it to include more effects. Canuto (1989) extended MLT to include anisotropies in the largest eddies and found that MLT overestimates convective velocities by a factor of 2 and underestimates the superadiabaticity by almost two orders of magnitudes. Standard MLT does not allow for overshooting or convective penetration: the boundaries of the CZ are rigid and the motion of the convective elements cannot extend to subadiabatic layers. Zahn (1991) included convective penetration in a simple model by means of a new free parameter, ζ, also of the order of unity as $\alpha_{\rm MLT}$. He estimated the extent of the subadiabatic region to be of the order of H_p. Helioseismology results, tracking the variations of

the speed of sound inside the Sun, put an upper limit for the overshoot extent of 0.1 H_p (e.g., Monteiro et al. 1994, Christensen-Dalsgaard et al. 1995).

Evidences for non-localities were found in laboratory experiments of convection between two plates (see, e.g, Tilgner et al. 1993, Spruit 1997, and references therein). In these experiments, the state of "hard turbulence" is characterized by scaling laws for statistical properties, such as heat flux and velocities, as a function of the Rayleigh number. The Rayleigh number, $\mathrm{Ra} = g\alpha\Delta T d^3/\nu\chi$, where g is the gravitational acceleration and α the thermal expansion coefficient, is a measure of the turbulence of the system. For convection to set in, a critical value of Ra must be exceeded and, in rotating systems, this value is an increasing function of rotation (Chandrasekhar 1961), if all the other parameters are kept fixed. At large Ra, the flow between the plates is non-local, with narrow downdraft and upflows from the upper and lower boundaries and nearly no flow from the core of the cell. We will discuss a similar phenomenon that could be relevant for stellar convection and the corresponding extension of MLT (Brandenburg 2016) in Section 3.2.

3.2 MLT extension through non-gradient flux

The derivation of MLT in Section 3.1 does not consider fluctuations in density or entropy. It is precisely the entropy fluctuations that can introduce a new term contributing to the energy flux. The existence of this contribution to the heat flux originated in the context of metereology (see, e.g., Deardorff 1966) and was first calculated by Deardorff (1972), using measurements of temperature fluctuations. In the stellar context, an expression for the Deardorff flux and the corresponding MLT extension was derived in Brandenburg (2016).

The vertical heat flux can be expressed in terms of the horizontally averaged enthalpy flux:

$$F_{\mathrm{enth}} = \overline{\rho U_z c_p T} \tag{3.9}$$

In standard MLT, the enthalpy flux corresponds to the convective flux, F_{conv}, because the kinetic energy flux, F_{kin}, that would also be part of F_{conv}, is zero due to balance of up- and down-flows. We can rewrite F_{enth} using the entropy s and the pressure P, taking advantage of the fact that pressure perturbations will disappear because sound waves will counter balance them quickly. Moreover, we use FOSA, so that the only relevant term will be proportional to $\overline{s'u_z'}$. Then, we can rewrite $c_p T' = T s'$ and the expression for the enthalpy flux will be (Brandenburg 2016):

$$F_{\mathrm{enth}} = \overline{\rho}\,\overline{T}\,\overline{u_z' s'}. \tag{3.10}$$

Now we can look at the term $\overline{u_z' s'}$: in the case of marginal stability ($\partial_z s \approx 0$), a positive entropy perturbation ($s' > 0$) is associated with a positive temperature perturbation and, accordingly, to a negative perturbation in density. The parcel of fluid will be less dense than its surroundings and it will move upward ($u_z' > 0$), for which $F_{\mathrm{enth}} > 0$. If the entropy perturbation is negative ($s' < 0$), the density of the parcel will increase and the parcel will sink ($u_z' < 0$), and this leads to $F_{\mathrm{enth}} > 0$. In any case, an entropy perturbation will produce instability and convection, even if the Schwarzschild's criterion would not be satisfied. In the case of the Sun, cool down-flows can be driven by radiative cooling in the upper layer.

The resulting plumes, or "threads" (Spruit 1997), will extend the depth of the convective layer, but their correlated length scales will correspond to the upper layers, therefore to granulation or supergranulation (Cossette and Rast 2016), thus capable of explaining the lack of power at large scales in horizontal velocity in helioseismic results. As a consequence, convection will be non-locally driven only in a layer much more shallow than the measured depth of the convection zone, $(0.713 \pm 0.001)R_\odot$ (Christensen-Dalsgaard et al. 1985, Basu and Antia 1997). The mechanism illustrated above is different from *overshooting*, that describes the penetration of fluid particles in the stable layer due to their inertia.

4 Numerical Methods

Noi veggiam, come quei c'ha mala luce.
Dante Alighieri, Inferno, X, 100, Divina Commedia.

To model the dynamics of the convection zone (CZ) of solar-like stars, we use the Pencil Code[1], that uses a 6th order finite-difference scheme for spatial discretization and 3rd order Runge-Kutta method for time integration. This model has been extensively used to study stars with convective envelopes (e.g., Käpylä et al. 2010, 2012a, 2013, Cole et al. 2014, Warnecke et al. 2014, Cole et al. 2016, Warnecke 2018).

We model a spherical shell without polar caps, where $0.7R \leq r \leq R$ is the radial extent, R being the stellar radius, and $\theta_0 \leq \theta \leq \pi - \theta_0$, with $\theta_0 = 15^{\circ}$, is the latitudinal extent. For the azimuthal extent, in most of the models we cover the full longitude, $0 \leq \phi \leq 2\pi$, but we also perform some wedge simulations ($0 \leq \phi \leq \pi/2$) for comparison. The domain is filled

[1] https://github.com/pencil-code/

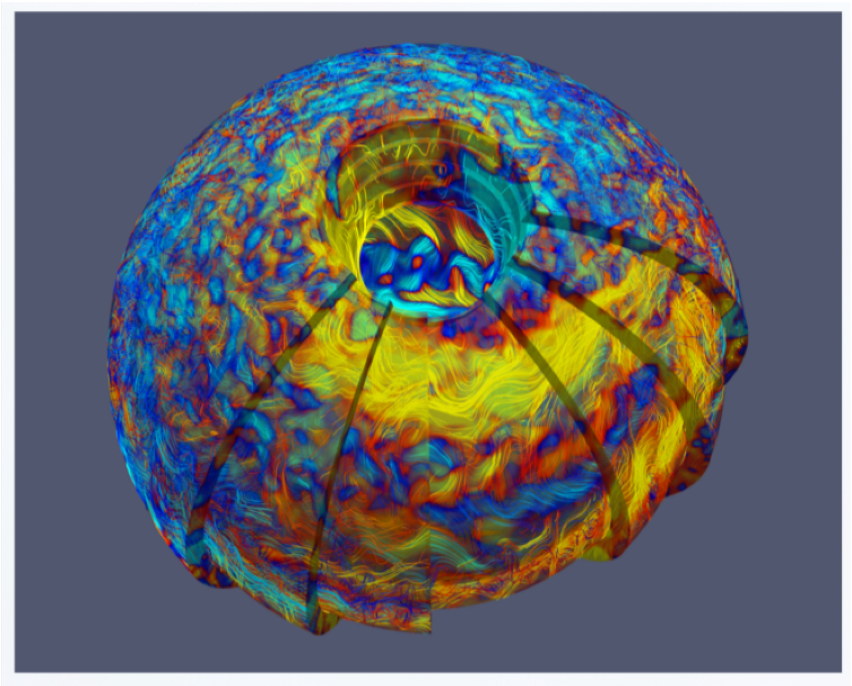

Figure 4.1: Magnetic field lines in a simulation rotating 7 times faster than the Sun, colour-coded with the magnitude of the azimuthal field, $\boldsymbol{B}_{\phi}$. Data from Viviani et al. (2018).

with a stratified fluid, heated at the bottom and cooled at the top. We apply an initially uniform rotation to a random weak flow and convection sets in, generating differential rotation and meridional circulation. In the right parameter regime, a seed magnetic field is able to excite a dynamo instability, and the magnetic field will grow until saturation. An example of the magnetic field configuration inside the shell in the saturation regime is shown in Fig 4.1.

In order to obtain such kind of solutions, we solve the compressible MHD equations:

$$\frac{\mathrm{D}\ln\rho}{\mathrm{D}t} + \nabla \cdot \boldsymbol{U} = 0, \tag{4.1}$$

$$\frac{\mathrm{D}\boldsymbol{U}}{\mathrm{D}t} = \boldsymbol{g} - 2\boldsymbol{\Omega}_0 \times \boldsymbol{U} + \frac{1}{\rho}\left(\boldsymbol{J} \times \boldsymbol{B} - \nabla p + \nabla \cdot 2\nu\rho\mathbf{S}\right), \tag{4.2}$$

$$T\frac{\mathrm{D}s}{\mathrm{D}t} = \frac{1}{\rho}\left[-\nabla \cdot \left(\boldsymbol{F}^{\mathrm{rad}} + \boldsymbol{F}^{\mathrm{SGS}}\right) + \mu_0\eta\boldsymbol{J}^2\right] + 2\nu\mathbf{S}^2, \tag{4.3}$$

$$\frac{\partial \boldsymbol{A}}{\partial t} = \boldsymbol{U} \times \boldsymbol{B} - \mu_0\eta\boldsymbol{J}, \tag{4.4}$$

$\mathrm{D}/\mathrm{D}t = \partial/\partial t + (\boldsymbol{U} \cdot \nabla)$ is the advective time derivative, $\boldsymbol{\Omega}_0 = \Omega_0\,(\cos\theta, -\sin\theta, 0)$ is the bulk rotation vector and the magnetic field is expressed through the magnetic vector potential, $\boldsymbol{B} = \nabla \times \boldsymbol{A}$, The expression of the rate-of-strain tensor is the same as in Equation 2.6. s is the specific entropy. $\boldsymbol{F}^{\mathrm{rad}}$ and $\boldsymbol{F}^{\mathrm{SGS}}$ are the radiative and sub-grid-scale fluxes:

$$\boldsymbol{F}^{\mathrm{rad}} = -K\nabla T, \quad \boldsymbol{F}^{\mathrm{SGS}} = -\chi_{\mathrm{SGS}}\rho T\nabla s \tag{4.5}$$

K is the radiative heat conductivity and χ_{SGS} is the sub-grid-scale heat diffusivity. $\boldsymbol{F}^{\mathrm{SGS}}$ takes care of the dissipation of energy at the finest scale, that cannot be captured by the finite resolution of the grid. It represents, therefore, the unresolved convective heat flux of the simulation. χ_{SGS} is a radial function, piece-wise constant and smoothly connecting the boundaries: $\chi_{\mathrm{SGS}}\,(0.7R) = 0$ and $\chi_{\mathrm{SGS}}\,(R) = 12.5\chi^m_{\mathrm{SGS}}$, where $\chi^m_{\mathrm{SGS}} = \chi_{\mathrm{SGS}}\,(0.85R)$. The much higher value of χ_{SGS} at the surface is chosen so that the input luminosity carries all the flux at the beginning of the simulation.

To close the system of equations, we choose an ideal gas equation of state for the pressure, $p = (\gamma - 1)\rho e$, where $\gamma = c_{\mathrm{P}}/c_{\mathrm{V}} = 5/3$ is the ratio of specific heat at constant pressure and volume, and $e = c_{\mathrm{V}}T$ is the internal energy.

The initial condition for the magnetic and velocity fields is a weak random seed field. Stratification is initially isentropic and the value of the hydrostatic temperature gradient at the bottom is fixed, while it follows a profile in the CZ:

$$\frac{\partial T}{\partial r} = -\frac{GM/r^2}{c_{\mathrm{V}}\,(\gamma - 1)\,(n_{\mathrm{ad}} + 1)} \tag{4.6}$$

$n_{\mathrm{ad}} = 1.5$ being the adiabatic index. The density profile is defined by the hydrostatic equilibrium state.

The input parameters defining the simulations are the bulk rotation in the frame of reference, Ω_0, ν, η, χ, χ_{SGS} and the energy flux at the bottom, $F_{\mathrm{bot}} = -(K\partial T/\partial r)_{r=r_0}$. From them we can derive the following non-dimensional input parameters:

$$\mathrm{Ta} = \left(\frac{2\Omega_0\Delta R^2}{\nu}\right), \quad \mathrm{Pr} = \frac{\nu}{\chi^m}, \quad \mathrm{Pr_M} = \frac{\nu}{\eta}, \quad \mathrm{Pr_{SGS}} = \frac{\nu}{\chi^m_{\mathrm{SGS}}} \tag{4.7}$$

where Ta is the Taylor number and ΔR is the thickness of the shell. Pr, $\mathrm{Pr_M}$ and $\mathrm{Pr_{SGS}}$ are the fluid, magnetic and sub-grid-scale Prandtl numbers, and $\chi^m = K/\left(c_p \rho^m\right)$ is the heat diffusivity evaluated at $r = 0.85R$. ρ^m is the value of the density at the same depth. Output parameters are the Coriolis and Reynolds numbers

$$\mathrm{Co} = \frac{2\Omega_0}{u_{\mathrm{rms}} k_f}, \quad \mathrm{Re} = \frac{u_{\mathrm{rms}}}{\nu k_f}, \quad \mathrm{Rm} = \frac{u_{\mathrm{rms}}}{\eta k_f}, \tag{4.8}$$

with $u_{\mathrm{rms}} = \sqrt{3/2 \left\langle U_r^2 + U_\theta^2 \right\rangle_{r\theta\phi t}}$ the rms velocity, where we omitted the $U_\phi-$term because it is dominated by the differential rotation, and accounted for it using the factor $3/2$. $k_f = 2\pi/\Delta R \approx 21 R^{-1}$ is the wavenumber of the largest eddy. The physical units are given by the solar values for angular velocity ($\Omega_\odot = 2.7 \cdot 10^{-6}$ s^{-1}), radius ($R = R_\odot = 7 \cdot 10^8$ m), and density at the bottom of the CZ ($\rho\,(0.7 R_\odot) = 200$ kg/m^3), and by the vacuum permeability, $\mu_0 = 4\pi \cdot 10^{-7}$ Hm^{-1}.

All the quantities are periodic in ϕ. For the velocity field we choose impenetrable and stress free boundary conditions (BC). At the bottom of the domain, we apply perfect-conductor BC for the magnetic field and the same condition is applied at the latitudinal boundaries, while at the top of the domain the field is radial. The BC for the magnetic field are enforced on the vector potential, so that the divergence-free condition is always satisfied. A constant heat flux supplies the energy from the bottom of the CZ, while a zero heat flux is prescribed at the latitudinal boundaries. A black body condition for the temperature is applied at the top boundary:

$$\sigma_{\mathrm{SB}} T^4 = -K \frac{\partial T}{\partial r} - \chi_{\mathrm{SGS}} \rho T \frac{\partial s}{\partial r}. \tag{4.9}$$

σ_{SB} is the modified Stefan-Boltzmann constant, that takes into account that the luminosity in our simulations is much larger than in the Sun. This modification is necessary because of our modelling strategy: since we are solving the compressible set of MHD equations, sound waves are not filtered and the advective timestep would be severely constrained by the speed of sound, c_s. We choose σ_{SB} so that, in the initial non-convective state, the surface flux carries the total luminosity.

4.1 The test-field method

In Section 5.2 we analyzed in more detail one of the simulations presented in Section 5.1. For the analysis we used the test-field method (Schrinner et al. 2005, 2007). The method is used to calculate the turbulent transport coefficients, $\boldsymbol{\alpha}, \boldsymbol{\beta}, \boldsymbol{\gamma}, \boldsymbol{\delta}$ and $\boldsymbol{\kappa}$ in Equation (2.17).

Mean-field dynamo theory, introduced in Section 2.2.2, relied on FOSA approximation, which consists in neglecting terms higher than second order in the fluctuations in the equation for the fluctuating magnetic field, Equation (2.15). The test-field method, in its most general form, is an attempt to go beyond the FOSA assumption, by retaining the higher-order terms and numerically solving the equation for the fluctuating magnetic field using test problems for $\overline{\boldsymbol{B}}$. In this thesis, we employed the currently existing form of the test-field method for spherical coordinates, truncating the series expansion of the EMF at second order, but solving for the full Equation (2.15), that is, not neglecting the term

$\nabla \times \left(\boldsymbol{u}' \times \boldsymbol{b}' - \overline{\boldsymbol{u}' \times \boldsymbol{b}'}\right)$, as is usually done when employing FOSA. Hence, our approach here is more general than FOSA, but not yet including the high-order terms in the series expansion. This would require to account for k- and time dependent test fields, but was out of the scope of the present thesis.

The general form for the EMF, taking into account non-localities in space and memory effects, is:

$$\overline{\mathcal{E}} = \overline{\mathcal{E}}_0 + \mathbf{K} \circ \overline{\boldsymbol{B}}, \tag{4.10}$$

where $\overline{\mathcal{E}}_0$ is the part of the EMF that does not depend on the mean magnetic field. Usually, one assumes that the EMF is homogeneous in $\overline{\boldsymbol{B}}$, therefore justifying $\overline{\mathcal{E}}_0 = 0$. The term $\mathbf{K} \circ \overline{\boldsymbol{B}}$ is a convolution integral, where $\mathbf{K}$ is a kernel that represents a spatial and temporal neighborhood of $\overline{\boldsymbol{B}}$:

$$\left(\mathbf{K} \circ \overline{\boldsymbol{B}}\right)_i = \int K_{ij}\left(\boldsymbol{x}, \boldsymbol{x}', t, t'\right) \overline{B}_j\left(\boldsymbol{x}', t'\right) d^3x' dt' \tag{4.11}$$

Brandenburg et al. (2008) considered the effects of non-locality in space on homogeneous and isotropic turbulence in Cartesian geometry, and found that the shape of the kernels for the tensors $\boldsymbol{a}$ and $\boldsymbol{b}$ are Lorentzian in spectral space and decaying exponentially in real space. Memory effects were addressed in Hubbard and Brandenburg (2009) and Rheinhardt and Brandenburg (2012), also in Cartesian geometry, considering statistically steady and homogeneous turbulence.

In the case of spherical coordinates, non-locality and memory effects have not been implemented yet, therefore we need to make some assumptions on the dependence of the EMF on $\overline{\boldsymbol{B}}$. We consider the dependency of $\overline{\mathcal{E}}$ from $\overline{\boldsymbol{B}}$ to be restricted to a narrow space interval (locality) and instantaneous (no memory effects). Moreover, we assume $\overline{\boldsymbol{B}}$ to vary slowly in time. Then, we can expand the EMF in terms of the mean magnetic field and its first order spatial derivatives, as in Equation (2.17). To calculate the coefficients, we introduce test fields in the equation for the fluctuating magnetic field (see, also Schrinner et al. 2007, Warnecke et al. 2018):

$$\frac{\partial \boldsymbol{b}'_T}{\partial t} = \boldsymbol{\nabla} \times \left(\boldsymbol{u}' \times \overline{\boldsymbol{B}}_T + \overline{\boldsymbol{U}} \times \boldsymbol{b}'_T\right) + \nabla \times \left(\boldsymbol{u}' \times \boldsymbol{b}'_T - \overline{\boldsymbol{u}' \times \boldsymbol{b}'_T}\right) - \boldsymbol{\nabla} \times \eta \boldsymbol{\nabla} \times \boldsymbol{b}'_T. \tag{4.12}$$

Here, $\boldsymbol{b}'_T$ is the fluctuating magnetic field calculated for each test field $\overline{\boldsymbol{B}}_T$. These test fields do not back-react on the flow. The number of test fields needed is set by the number of free parameters in Equation (2.17). In the axisymmetric case, we have 3 linear equations, each one containing 9 free parameters, therefore 9 test fields are needed. $\overline{\boldsymbol{U}}$ and $\boldsymbol{u}'$ are taken from the simulation for which we want to calculate the turbulent transport coefficients. The $\boldsymbol{b}'_T$ are used to calculate the EMF, $\overline{\mathcal{E}}_T = \overline{\boldsymbol{u}' \times \boldsymbol{b}'_T}$. To obtain the coefficients, we then invert the relation:

$$\overline{\mathcal{E}}_T = a_{ij} \overline{B}_{Tj} + b_{ijk} \frac{\partial \overline{B}_{Tj}}{\partial x_k} \tag{4.13}$$

for all the test fields.

The $\overline{\boldsymbol{B}}_T$s must be axisymmetric, linearly independent, with derivatives not higher than first order in space and slowly varying in time. The constraint on the coordinate derivatives can be relaxed, if the values of the test-fields do not exceed unity. Since the $\overline{\boldsymbol{B}}_T$s do not obey an evolution equation, they do not have to satisfy any boundary condition.

Equation (2.16) is valid in Cartesian coordinates. The corresponding form in spherical geometry is:

$$\overline{\mathcal{E}}_i = \tilde{a}_{ij}\overline{B}_j + \tilde{b}_{ijr}\frac{\partial \overline{B}_j}{\partial r} + \tilde{b}_{ij\theta}\frac{1}{r}\frac{\partial \overline{B}_j}{\partial \theta} \tag{4.14}$$

where $\tilde{a}_{ij}$, $\tilde{b}_{ijr}$ and $\tilde{b}_{ij\theta}$ are now not in covariant form, that is they are not coordinate independent. Once the coefficients are rewritten in covariant form, we obtain again the expression (2.17), which is still local and instantaneous.

In relating the expressions (4.14) and (2.17) to each other we have some degrees of freedom because of axisymmetry: the coefficients $b_{ij\phi}$ are not determined. Since they do not affect the EMF, we can choose them arbitrarily. In Schrinner et al. (2005, 2007) and Warnecke et al. (2018), the choice $b_{ij\phi} = 0$ was made, while we chose $b_{ij\phi} = -b_{i\phi j}$. The resulting expressions for the coefficients α_{ij}, β_{ij}, γ_i, δ_i and κ_{ijk} are shown in Appendix A.2 of Section 5.2. One of the advantages of choosing this decomposition is that in the isotropic case the diagonal components of $\boldsymbol{\beta}$ become equal.

4.2 Heat conduction

In models based on MLT, the radiative heat conductivity K in Equation (4.5) has a fixed profile, so that the whole bulk of the simulated domain is made convectively unstable. Such a configuration, motivated by mixing-length arguments, will excite convection at the largest scales possible and, therefore, the wavenumber of the largest eddy will correspond to the depth of the CZ, $k_f = 2\pi/\,(0.3R)$.

In Sections 5.1 and 5.2, we used a prescribed profile for K, as described in Käpylä et al. (2013): at the bottom of the CZ, we impose an energy flux $F_{\rm bot} = -K\partial_r T\,|_{r=0.7R}$, where the temperature gradient is given by Equation (4.6), with the polytropic index $n_{\rm ad} = 1.5$. n varies from the adiabatic value to the value $n = 1$ at the surface. The radiative heat conductivity is responsible for delivering energy flux into the domain and towards the surface. Its profile decreases strongly in radius, in order for convection to carry most of the flux through the bulk of the domain. Such a profile is described by

$$\begin{aligned} n &= 2.5\left(\frac{r}{0.7R}\right)^{-15} - 1 \\ K &= (n+1)\,K_0 \\ K_0 &= \frac{\mathcal{L}}{4\pi} c_v\,(\gamma-1)\,(n_{\rm ad}+1)\,\rho_0\,\sqrt{GMR} \\ \mathcal{L} &= \frac{L_0}{\rho_0\,(GM)^{3/2}\,R^{1/2}}, \end{aligned} \tag{4.15}$$

where ρ_0 is a reference value for the density, and $\mathcal{L}$ is the non-dimensional luminosity and L_0 is the input luminosity.

To identify the contributions to the energy transport, we define the longitudinally av-

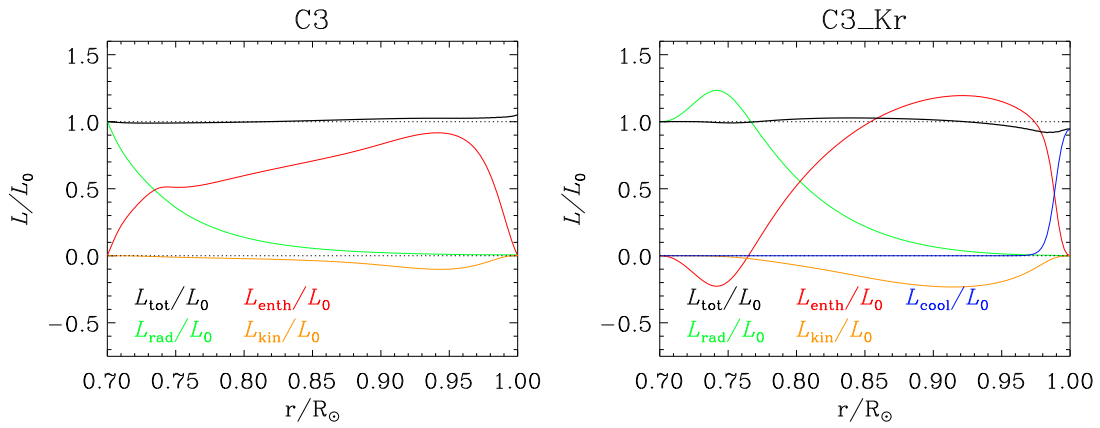

Figure 4.2: Total (black), radiative (green), enthalpy (red), kinetic (yellow) and cooling (blue) normalized luminosities, averaged over latitude and longitude, as a function of radius for a semi-spherical run with prescribed heat conductivity (Run C3 of Section 5.1, left panel) and its counterpart using Kramers opacity law (right panel, see, also, Section 5.3). In the left panel $L_{\rm cool} = 0$.

eraged vertical fluxes:

$$\begin{aligned} \overline{F}_{\rm enth} &= \overline{c_p \left(\rho \boldsymbol{u}_r\right)' T} \\ \overline{F}_{\rm rad} &= -\overline{K \partial_r T} \\ \overline{F}_{\rm kin} &= \frac{1}{2}\overline{\rho \boldsymbol{U}^2 U_r} \\ \overline{F}_{\rm tot} &= \sum_i \overline{F}_i. \end{aligned} \tag{4.16}$$

From the fluxes, we define the corresponding luminosities as $L_i = 4\pi r^2 F_i$. Typical energy transport for a simulation using MLT-based heat conduction profile is shown in Figure 4.2, left panel. The radiative flux, in green, supplies the energy at the bottom and then strongly decreases throughout the CZ. In the major part of the CZ, all the luminosity is carried by convection, while, since in MLT approximation upflows and downflows are balanced, the kinetic flux is almost zero.

Right panel of Figure 4.2 depicts energy transport in a simulation with the same initial parameters as Run C3, but with a different treatment for heat conduction, which is now a function of density and temperature, $K(\rho, T)$. In this case:

$$\begin{aligned} K &= \frac{16\sigma_{\rm SB} T^3}{3\kappa\rho}, \\ \text{with} \quad \kappa &= \kappa_0 \left(\frac{\rho}{\rho_0}\right)^a \left(\frac{T}{T_0}\right)^b, \end{aligned} \tag{4.17}$$

where $\sigma_{\rm SB}$ is the modified Stefan-Boltzmann constant and κ is the opacity, with κ_0, ρ_0 and T_0 reference values for opacity, density and temperature, respectively. Inserting the expression for the opacity in K (Barekat and Brandenburg 2014), we obtain:

$$K = K_0 \left(\frac{\rho}{\rho_0}\right)^{(a+1)} \left(\frac{T}{T_0}\right)^{3-b}, \tag{4.18}$$

where K_0 subsumes all the constants. The choice $a = 1$ and $b = -7/2$ corresponds to Kramers opacity law for bound-free and free-free transitions. With this description, Equation (4.3) needs a cooling term depending only on radius (see, e.g., Käpylä et al. 2019b), $\Gamma_{\rm cool}$, to prevent a subadiabatic layer to develop near the surface:

$$T\frac{\mathrm{D}s}{\mathrm{D}t} = \frac{1}{\rho}\left[-\nabla\cdot\left(\boldsymbol{F}^{\rm rad}+\boldsymbol{F}^{\rm SGS}\right)+\mu_0\eta\boldsymbol{J}^2-\Gamma_{\rm cool}\right]+2\nu\mathsf{S}^2. \tag{4.19}$$

The corresponding flux is:

$$\overline{F}_{\rm cool} = \int_{0.7R}^{R}\Gamma_{\rm cool}dr \tag{4.20}$$

and the associated luminosity is shown in blue in the right panel of Figure 4.2. Numerical setups using this heat conduction description have been used is Cartesian coordinates (Brandenburg et al. 2000, Brandenburg 2016, Käpylä et al. 2017, Käpylä 2018) as well as in spherical wedge simulations (Käpylä et al. 2019a,b). In Section 5.3 we used this same setup in a semi-spherical domain, spanning the full longitudinal extent.

In the right panel of Figure 4.2, convection is suppressed at the bottom of the domain and the kinetic flux is no longer negligible. The structure of the CZ is completely changed with respect to the MLT picture. Therefore, we need to redefine the total convective flux as the sum of enthalpy and kinetic fluxes (Cattaneo et al. 1991, Käpylä 2018):

$$F_{\rm conv} = F_{\rm enth} + F_{\rm kin} \tag{4.21}$$

where the enthalpy flux was defined in Equation (3.10).

Using the values of $F_{\rm enth}$ and the superadiabaticity $\nabla - \nabla_{\rm ad}$, Käpylä et al. (2017) redefined the CZ. The classical convective layer according to MLT is defined by $F_{\rm enth} > 0$ and $\nabla - \nabla_{\rm ad} > 0$: this zone was renamed buoyancy zone (BZ). The Kramers opacity law generates a layer in which $F_{\rm enth} > 0$ but $\nabla - \nabla_{\rm ad} < 0$: here, the medium is subadiabatic but still convecting. This is the effect of the Deardorff term, including the entropy fluctuations, that we discussed in Section 3.2, and that contributes positively to the flux whatever the sign of the entropy fluctuations. This layer is named as Deardorff zone (DZ). The new redefined convection zone is the union of BZ and DZ. The overshoot zone is defined by $F_{\rm enth} < 0$ and $\nabla - \nabla_{\rm ad} < 0$: here, the fluid parcels descending from above, but with enough entropy content, can penetrate and generate weak upflows. Lastly, the layer in which $F_{\rm enth} \approx 0$ and $\nabla - \nabla_{\rm ad} < 0$ is the radiative zone (RZ). In this new scenario, convection is driven by the cool downflows from the convectively unstable layer at the surface, a phenomenon known as *entropy rain* (see, Stein and Nordlund 1989, Brandenburg 2016, for the theoretical description), whose numerical evidence was found for the first time in the study of Käpylä et al. (2017).

5 Results

Di lor cagion m'accesero un disio
mai non sentito di cotanto acume.
Dante Alighieri, Paradiso, I, 82-84, Divina Commedia

In this chapter we present two already published manuscript (Section 5.1 and 5.2) and a third one (Section 5.3) that will be submitted for publication in the near future. The aim of these studies was to understand how the dynamo solutions in global simulations change as a function of different parameters. We used a setup covering the full longitudinal extent, but still missing the poles. We examine the role of rotation rate on the dynamo solutions (Section 5.1), and later we focus on the origin of the oscillating magnetic field in a particular case (Section 5.2). We also consider the importance of heat conduction and its numerical implementation (Section 5.3) and how this affects the results of Section 5.1.

Section 5.1 reports on an extensive study on rotation rate that allowed us to mark the transition from axisymmetric to non-axisymmetric dynamos in numerical simulations. This transition was observed also in photometric studies (Lehtinen et al. 2016) and was related to drifting dynamo waves in the azimuthal direction, which we also find in our study. We also describe the necessity of maintaining the supercriticality of convection in numerical models in order for the results to be representative of the turbulent fluids present in stellar convection zones.

Section 5.2 is a more in-depth study of a simulation from Section 5.1, by means of the test-field method. We were interested in finding the origin of the oscillating magnetic field of the solution and tested it against the two main dynamo paradigms: Parker waves or advection-dominated flux-transport models. We found that neither of the two gives a satisfactory explanation, but rather turbulent effects, such as the α or δ effect, are responsible for the generation of the magnetic field in this simulation.

Section 5.3 presents the results of models using Kramers opacity law. We found that the new prescription in heat transfer affects the rotational profiles and the propagation direction of the azimuthal waves found in Section 5.1. Lehtinen et al. (2016) reported on a preference for prograde azimuthal waves, which we found in this Section, while mostly retrograde waves were found in Section 5.1. The results of this Section are, therefore, more compatible with magnetic field proxies in active stars. On the other hand, the convective velocities in the Kramers cases are higher than with a fixed profile for heat conduction and, hence, the Coriolis numbers are reduced, which accentuates the discrepancies between observations and simulations regarding the velocity field.

5.1 Transition from axi- to nonaxisymmetric dynamo modes in spherical convection models of solar-like stars

Contribution to the paper: I run complementary simulations, in particular at high resolution. I performed all the data analysis and participated in the development of the spherical harmonics decomposition routine. I wrote the Results section in the manuscript and participated in the writing of the manuscript.

A&A 616, A160 (2018)
https://doi.org/10.1051/0004-6361/201732191

Astronomy & Astrophysics

Transition from axi- to nonaxisymmetric dynamo modes in spherical convection models of solar-like stars

M. Viviani[1], J. Warnecke[1,2], M. J. Käpylä[1,2], P. J. Käpylä[3,2,1,4], N. Olspert[2], E. M. Cole-Kodikara[5], J. J. Lehtinen[1,2], and A. Brandenburg[4,6,7,8]

[1] Max Planck Institute for Solar System Research, Justus-von-Liebig-Weg 3, 37077 Göttingen, Germany
e-mail: viviani@mps.mpg.de
[2] ReSoLVE Centre of Excellence, Department of Computer Science, Aalto University, PO Box 15400, 00076 Aalto, Finland
[3] Leibniz Institute for Astrophysics Potsdam, An der Sternwarte 16, 14482 Potsdam, Germany
[4] NORDITA, KTH Royal Institute of Technology and Stockholm University, Roslagstullsbacken 23, 10691 Stockholm, Sweden
[5] Department of Physics, University of Helsinki, Gustaf Hällströmin katu 2a, PO Box 64, 00014 Helsinki, Finland
[6] Department of Astronomy, AlbaNova University Center, Stockholm University, 10691 Stockholm, Sweden
[7] JILA and Department of Astrophysical and Planetary Sciences, University of Colorado Box 440, Boulder, CO 80303, USA
[8] Laboratory for Atmospheric and Space Physics, 3665 Discovery Drive, Boulder, CO 80303, USA

Received 27 October 2017 / Accepted 23 April 2018

ABSTRACT

Context. Both dynamo theory and observations of stellar large-scale magnetic fields suggest a change from nearly axisymmetric configurations at solar rotation rates to nonaxisymmetric configurations for rapid rotation.
Aims. We seek to understand this transition using numerical simulations.
Methods. We use three-dimensional simulations of turbulent magnetohydrodynamic convection in spherical shell wedges and considered rotation rates between 1 and 31 times the solar value.
Results. We find a transition from axi- to nonaxisymmetric solutions at around 1.8 times the solar rotation rate. This transition coincides with a change in the rotation profile from antisolar- to solar-like differential rotation with a faster equator and slow poles. In the solar-like rotation regime, the field configuration consists of an axisymmetric oscillatory field accompanied by an $m = 1$ azimuthal mode (two active longitudes), which also shows temporal variability. At slow (rapid) rotation, the axisymmetric (nonaxisymmetric) mode dominates. The axisymmetric mode produces latitudinal dynamo waves with polarity reversals, while the nonaxisymmetric mode often exhibits a slow drift in the rotating reference frame and the strength of the active longitudes changes cyclically over time between the different hemispheres. In the majority of cases we find retrograde waves, while prograde waves are more often found from observations. Most of the obtained dynamo solutions exhibit cyclic variability either caused by latitudinal or azimuthal dynamo waves. In an activity-period diagram, the cycle lengths normalized by the rotation period form two different populations as a function of rotation rate or magnetic activity level. The slowly rotating axisymmetric population lies close to what in observations is called the inactive branch, where the stars are believed to have solar-like differential rotation, while the rapidly rotating models are close to the superactive branch with a declining cycle to rotation frequency ratio and an increasing rotation rate.
Conclusions. We can successfully reproduce the transition from axi- to nonaxisymmetric dynamo solutions for high rotation rates, but high-resolution simulations are required to limit the effect of rotational quenching of convection at rotation rates above 20 times the solar value.

Key words. convection – Sun: activity – magnetohydrodynamics (MHD) – dynamo – turbulence – Sun: rotation

1. Introduction

Large-scale magnetic fields in late-type stars are thought to be maintained by a dynamo process within or just below the convection zone (e.g., Ossendrijver 2003; Charbonneau 2013). In the relatively slowly rotating and magnetically inactive Sun, the dynamo process is often described by a classical $\alpha\Omega$ dynamo, where shearing due to differential rotation produces a toroidal magnetic field from a poloidal magnetic field (Ω effect), and cyclonic convection (α effect) is responsible for regenerating the poloidal field (Parker 1955). Younger late-type stars rotate much faster than the Sun and they also exhibit more vigorous magnetic activity. Theoretical models have long indicated that the differential rotation stays roughly constant as a function of rotation (e.g., Kitchatinov & Rüdiger 1999). The interpretation of observational data is much more challenging. Recent studies show either a mild decrease (e.g., Lehtinen et al. 2016) or a mild increase (Reinhold et al. 2013; Reinhold & Gizon 2015; Distefano et al. 2017) of the relative latitudinal differential rotation, indicating a broad agreement with the theoretical expectation. Therefore, the main effect of increased rotation is a relative dominance of the α effect compared with differential rotation in maintaining the toroidal field. Hence, in view of dynamo theory (e.g., Krause & Rädler 1980), dynamos in rapidly rotating stars operate in a regime in which dynamo action is nearly fully maintained by cyclonic convection (α^2 dynamo). Since the early theoretical work it has been known that in the rapid rotation regime the α effect becomes increasingly anisotropic (Rüdiger 1978). An indication of this has been seen at moderate rotation rates (Warnecke et al. 2018). Such an anisotropic α effect can promote nonaxisymmetric large-scale magnetic field configurations (e.g., Rädler et al. 1990; Moss & Brandenburg 1995; Moss et al. 1995; Pipin 2017).

Solar and stellar dynamos tend to manifest themselves very differently in observations. The solar magnetic field exhibits cyclic behavior, in which the activity indicators vary over an approximate 11 yr cycle; during each activity cycle the polarity of the field reverses, resulting in a magnetic cycle of roughly 22 yr. During one activity cycle, the location in which sunspots appear migrates from mid-latitudes toward the equator. This is commonly thought to trace the latitudinal dynamo wave, that is, a predominantly toroidal component of the large-scale magnetic field that migrates toward the equator. In the Sun, the longitudinal distribution of sunspots indicates that the solar large-scale magnetic field is mostly axisymmetric (e.g., Pelt et al. 2006). In late-type stars with rapid rotation, by contrast, much larger spots located at high latitudes or even polar regions have been observed using Doppler imaging (DI), Zeeman Doppler imaging (ZDI), and interferometry (e.g., Järvinen et al. 2008; Hackman et al. 2016; Roettenbacher et al. 2016). Many studies have reported on highly nonaxisymmetric spot configurations (e.g., Jetsu 1996; Berdyugina & Tuominen 1998), referred to as active longitudes, while especially the indirect imaging of the surface magnetic field using ZDI tends to yield more axisymmetric configurations (Rosén et al. 2016; See et al. 2016).

Especially interesting are the recent results by Lehtinen et al. (2016) regarding a sample of solar-like stars obtained by analyzing photometric light curves. They show a rather sharp transition from stars with magnetic cycles and no active longitudes to stars with both cycles and active longitudes, as the activity level or rotation rate of the stars increases. This result can be interpreted in terms of rapid rotators hosting nonaxisymmetric dynamos and moderate rotators axisymmetric ones. Furthermore, some studies have reported cyclic behavior related to the active longitudes in the form of the activity periodically switching from one longitude to the other on the same hemisphere (Berdyugina et al. 2002) in an abrupt flip-flop event (Jetsu et al. 1993). Other studies report irregular polarity changes between the two longitudes; these are not necessarily connected to the overall cyclic variability of the star (Hackman et al. 2013; Olspert et al. 2015).

The stellar cycles remain poorly characterized, however. Nevertheless, it is clear that many late-type stars exhibit time variability that appears cyclic. This is especially well manifested by studies of stellar samples, such as the intensively investigated Mount Wilson chromospheric activity data base (Baliunas et al. 1995; Oláh et al. 2016; Boro Saikia et al. 2018; Olspert et al. 2018). Even if the range of periods that can be studied is severely limited by the nature of the data because it is too short to study long cycles while the rotational and seasonal timescales limit the periods at the short end, it is clear that stellar cycles are common and even multiple superimposed cycles can occur in one and the same object (Oláh et al. 2009; Lehtinen et al. 2016). There are also indications that the stars tend to cluster into distinct activity branches in a diagram in which the ratio of the cycle period over rotation period is plotted against the rotation rate or activity level (Saar & Brandenburg 1999; Lehtinen et al. 2016; Brandenburg et al. 2017), but the existence of these branches continues to raise debate (Reinhold et al. 2017; Distefano et al. 2017; Boro Saikia et al. 2018; Olspert et al. 2018).

The steadily increasing computational resources have enabled large-scale use of self-consistent three-dimensional (3D) convection simulations to study the mechanisms that drive dynamo action in stars. Recent 3D numerical simulations have been successful in reproducing many aspects of the solar dynamo, such as cyclic magnetic activity and equatorward migration (e.g., Ghizaru et al. 2010; Käpylä et al. 2012; Augustson et al. 2015), the existence of multiple dynamo modes (Käpylä et al. 2016; Beaudoin et al. 2016), and irregular behavior (Augustson et al. 2015; Käpylä et al. 2016, 2017). There are also studies that investigate the dependence of the dynamo solutions on rotation rate, but these have so far either been limited to wedges with limited longitudinal extent (Käpylä et al. 2013, 2017; Warnecke et al. 2016; Warnecke 2018) or the range of rotation rates investigated have been restricted to narrow regions in the vicinity of the solar rotation rate (Strugarek et al. 2017) or three times the solar rotation rate (Nelson et al. 2013). The first indications of stellar dynamos changing from axisymmetric to nonaxisymmetric were reported by Käpylä et al. (2013), Cole et al. (2014), and Yadav et al. (2015b), occurring in the regime of moderate rotation. However, the parameter ranges were rather limited in these studies.

Planetary dynamo simulations (e.g., Ishihara & Kida 2000; Schrinner et al. 2012; Gastine et al. 2012), which typically have much lower density stratification than their stellar counterparts, show that a transition from multipolar to dipolar magnetic field configurations exists at sufficiently rapid rotation. Dipolar solutions have also been found in models with high density stratification and low Prandtl number (Jones 2014; Yadav et al. 2015a; Duarte et al. 2018). Simulations of fully convective stars also favored the occurrence of dipolar solutions (Dobler et al. 2006), but with a transition to multipolar solutions at slower rotation (Browning 2008).

Intriguingly, some ZDI studies suggest that both weak multipolar and strong dipolar magnetic field configurations can occur with very similar stellar parameters in rapidly rotating low-mass (spectral type M) stars (e.g., Morin et al. 2010; Stassun et al. 2011). These observations challenge the simple picture that the M-star dynamos are classical α^2 type. Namely, in this case the theoretical expectation is that because the Coriolis number is large owing to long convective turnover times, the α effect becomes strongly anisotropic and results in nonaxisymmetric (multipolar) fields (e.g., Rädler et al. 1990; Moss & Brandenburg 1995; Moss et al. 1995; Pipin 2017). Numerical simulations have revealed bistable dynamo solutions in the rapid rotation regime in which both configurations can be found with the same system parameters but different initial conditions (e.g., Schrinner et al. 2012; Gastine et al. 2012). However, the dipolar solution is typically realized only with a strong initial field.

The goal of the present paper is to carry out a systematic survey of convective dynamo simulations in an attempt to understand the change of magnetic field generation from a young rapidly rotating Sun to its present rotation rate. We are specifically studying the transition of the dynamo solutions from axisymmetric to nonaxisymmetric solutions.

2. Model and setup

We used spherical polar coordinates (r, θ, ϕ) to model the magnetohydrodynamics (MHD) in convective envelopes of solar-like stars. The general model and setup are detailed in Käpylä et al. (2013). For most of the runs we used the full azimuthal extent ($0 \le \phi \le 2\pi$). However, for some runs we considered only a quarter of the full range ($0 \le \phi \le \pi/2$), which we call $\pi/2$ wedges for short. We omitted the poles and thus modeled the star between $\pm 75°$ latitude ($\theta_0 \le \theta \le \pi - \theta_0$, with $\theta_0 = 15°$) and modeled only the convection zone of the star in radius ($0.7R \le r \le R$, where R is the radius of the star).

2.1. Basic equations

We solve the compressible MHD equations

$$\frac{\partial \boldsymbol{A}}{\partial t} = \boldsymbol{u} \times \boldsymbol{B} - \mu_0 \eta \boldsymbol{J}, \tag{1}$$

$$\frac{D \ln \rho}{Dt} = -\boldsymbol{\nabla} \cdot \boldsymbol{u}, \tag{2}$$

$$\frac{D\boldsymbol{u}}{Dt} = \boldsymbol{g} - 2\boldsymbol{\Omega}_0 \times \boldsymbol{u} + \frac{1}{\rho}(\boldsymbol{J} \times \boldsymbol{B} - \boldsymbol{\nabla} p + \boldsymbol{\nabla} \cdot 2\nu\rho \mathbf{S}), \tag{3}$$

$$T \frac{Ds}{Dt} = \frac{1}{\rho}\left[-\boldsymbol{\nabla} \cdot \left(\boldsymbol{F}^{\rm rad} + \boldsymbol{F}^{\rm SGS}\right) + \mu_0 \eta \boldsymbol{J}^2\right] + 2\nu \mathbf{S}^2, \tag{4}$$

where $\boldsymbol{A}$ is the magnetic vector potential, $\boldsymbol{u}$ is the velocity, $D/Dt = \partial/\partial t + \boldsymbol{u} \cdot \boldsymbol{\nabla}$ is the Lagrangian time derivative, $\boldsymbol{B} = \boldsymbol{\nabla} \times \boldsymbol{A}$ is the magnetic field, $\boldsymbol{J} = \mu_0^{-1} \boldsymbol{\nabla} \times \boldsymbol{B}$ is the current density, μ_0 and ρ are the vacuum permeability and plasma density, respectively, ν and η are the constant kinematic viscosity and magnetic diffusivity, respectively, $\boldsymbol{g} = -GM\boldsymbol{r}/r^3$ is the gravitational acceleration where G is the gravitational constant and M is the mass of the star, $\boldsymbol{\Omega}_0 = \Omega_0(\cos\theta, -\sin\theta, 0)$ is the rotation vector, where Ω_0 is the rotation rate of the frame of reference, $\mathbf{S}$ is the rate-of-strain tensor, s is the specific entropy; the equations above are solved together with an equation of state for the pressure p, assuming an ideal gas $p = (\gamma - 1)\rho e$, where $e = c_V T$ is the internal energy, T is the temperature, and $\gamma = c_P/c_V$ is the ratio of specific heats at constant pressure and volume, respectively. The radiative and subgrid-scale (SGS) heat fluxes are given by $\boldsymbol{F}^{\rm rad} = -K\boldsymbol{\nabla} T$ and $\boldsymbol{F}^{\rm SGS} = -\chi_{\rm SGS}\rho T \boldsymbol{\nabla} s$, respectively, where K is the radiative heat conductivity and $\chi_{\rm SGS}$ is the SGS heat diffusivity.

2.2. Setup characteristics

The initial stratification is isentropic, where the hydrostatic temperature gradient is defined via an adiabatic polytropic index of $n_{\rm ad} = 1.5$. We initialize the magnetic field with a weak white-noise Gaussian seed field. More details about our initial setup can be found in Käpylä et al. (2013).

Most of our runs use a grid covering the full azimuthal extent, but we perform some comparison runs, labelled with superscript "W" for $\pi/2$ wedges with reduced longitudinal extent. In all cases, we assume periodicity in the azimuthal direction for all quantities. For the magnetic field, we apply perfect conductor boundary conditions at the bottom and both latitudinal boundaries, and at the top boundary we use a radial field condition. Stress-free, impenetrable boundaries are used for the velocity on all radial and latitudinal boundaries. The boundary condition of entropy is set by assuming a constant radiative heat flux at the bottom of the computational domain. The thermodynamic quantities have zero first derivatives on both latitudinal boundaries, leading to zero energy fluxes there. At the top boundary, the temperature follows a black body condition. The exact equations for these conditions are described in Käpylä et al. (2013, 2017).

Our simulations are defined by the following nondimensional parameters. As input parameters we quote the Taylor number

$$\mathrm{Ta} = \left[2\Omega_0 (0.3R)^2/\nu\right]^2, \tag{5}$$

the fluid, SGS, and magnetic Prandtl numbers

$$\mathrm{Pr} = \frac{\nu}{\chi_{\rm m}}, \quad \mathrm{Pr_{SGS}} = \frac{\nu}{\chi^{\rm m}_{\rm SGS}}, \quad \mathrm{Pr_M} = \frac{\nu}{\eta}, \tag{6}$$

where $\chi_{\rm m} = K(r_{\rm m})/c_P \rho(r_{\rm m})$ and $\chi^{\rm m}_{\rm SGS} = \chi_{\rm SGS}(r_{\rm m})$ are evaluated at $r_{\rm m} = 0.85R$. The Rayleigh number is obtained from the hydrostatic stratification, evolving a one-dimensional (1D) model, and is given by

$$\mathrm{Ra} = \frac{GM(0.3R)^4}{\nu \chi^{\rm m}_{\rm SGS} R^2}\left(-\frac{1}{c_{\rm P}}\frac{{\rm d}s_{\rm hs}}{{\rm d}r}\right)_{(r=0.85R)}, \tag{7}$$

where $s_{\rm hs}$ is the hydrostatic entropy.

Useful diagnostic parameters are the density contrast

$$\Gamma_\rho \equiv \rho(r = 0.7R)/\rho(R), \tag{8}$$

fluid and magnetic Reynolds numbers and the Péclet number,

$$\mathrm{Re} = \frac{u_{\rm rms}}{\nu k_{\rm f}}, \quad \mathrm{Re_M} = \frac{u_{\rm rms}}{\eta k_{\rm f}}, \quad \mathrm{Pe} = \frac{u_{\rm rms}}{\chi^{\rm m}_{\rm SGS} k_{\rm f}}, \tag{9}$$

where $k_{\rm f} = 2\pi/0.3R \approx 21/R$ is an estimate of the wavenumber of the largest eddies. The Coriolis number is defined as

$$\mathrm{Co} = \frac{2\Omega_0}{u_{\rm rms} k_{\rm f}}, \tag{10}$$

where $u_{\rm rms} = \sqrt{(3/2)\langle u_r^2 + u_\theta^2 \rangle_{r\theta\phi t}}$ is the rms velocity and the subscripts indicate averaging over r, θ, ϕ, and a time interval during which the run is thermally relaxed and typically covers at least one magnetic diffusion time.

We define mean quantities as averages over the ϕ-coordinate and denote these by an overbar, for example $\langle \boldsymbol{B} \rangle_\phi = \overline{\boldsymbol{B}}$. The difference between the total and the mean, for example $\boldsymbol{B}' = \boldsymbol{B} - \overline{\boldsymbol{B}}$, are the fluctuations. Furthermore, we indicate volume averages using $\langle \cdot \rangle_V$.

For the purpose of this paper, it is convenient to normalize the rotation rate by the solar value, so we define

$$\tilde{\Omega} \equiv \Omega_0/\Omega_\odot, \tag{11}$$

where $\Omega_\odot$ is the solar rotation rate. Moreover, we use $\Omega_\odot = 2.7 \times 10^{-6}\,{\rm s}^{-1}$, the solar radius $R = 7 \times 10^8\,{\rm m}$, $\rho(0.7R) = 200\,{\rm kg\ m^{-3}}$, and $\mu_0 = 4\pi \times 10^{-7}\,{\rm H\ m^{-1}}$ to normalize our quantities to physical units.

The simulations were performed using the Pencil Code[1]. The code employs a high-order finite difference method for solving the compressible equations of MHD.

3. Results

We consider a number of runs that probe the rotational dependence in the range $\tilde{\Omega} = 1$–31, corresponding to Co = 1.6–126.5; see Table 1. The range in Co is larger than that in $\tilde{\Omega}$ because faster rotation leads to lower supercriticality of convection, resulting in a decreased $u_{\rm rms}$ and increased Co; see Eq. (10). For some rotation rates we consider different values of the SGS Prandtl number, resulting in different Rayleigh and Péclet numbers and different levels of supercriticality. Runs E, F1, and H are direct continuations of Runs A, B, and C of Cole et al. (2014) and Run F1 was already discussed as Run E4 (Käpylä et al. 2013). Run $\mathrm{G^W}$ has been analyzed as Run I in Warnecke et al. (2014), as Run A1 in Warnecke et al. (2016), as Run D3 in Käpylä et al. (2016) and in Warnecke et al. (2018). Furthermore, Runs A1 and A2 correspond to 2π extensions of the $\pi/2$ wedges of Set F in

[1] https://github.com/pencil-code/

Table 1. Summary of the runs.

Run	Grid	$\tilde{\Omega}$	Pr	$\mathrm{Pr_{SGS}}$	$\mathrm{Pr_M}$	Ta	Ra	Re	Pe	$\mathrm{Re_M}$	Co	Γ_ρ	Δt	$\Delta_\Omega^{(r)}$	$\Delta_\Omega^{(\theta)}$	$\lvert\Delta\Omega_r\rvert$	$\lvert\Delta\Omega_\theta\rvert$
A1	$144\times288\times576$	1.0	58	2.50	1.00	6.32×10^6	6.54×10^7	40	100	40	1.6	22	22	–0.26	–0.37	0.26	0.37
A2	$144\times288\times576$	1.0	69	0.30	1.00	4.39×10^6	8.00×10^5	36	10	36	1.4	21	23	–0.22	–0.24	0.22	0.24
B	$144\times288\times576$	1.5	58	2.50	1.00	1.42×10^7	6.54×10^7	40	100	40	2.4	22	32	–0.11	–0.17	0.22	0.24
C1	$144\times288\times576$	1.8	58	2.50	1.00	2.03×10^7	6.54×10^7	41	102	41	2.8	22	26	–0.08	–0.11	0.14	0.20
C2	$144\times288\times576$	1.8	58	1.00	1.00	2.03×10^7	1.29×10^7	43	43	43	2.6	22	45	0.78	–0.35	0.13	0.17
C3	$144\times288\times576$	1.8	77	0.33	1.00	1.14×10^7	7.00×10^5	28	9	28	3.0	20	88	0.07	0.17	0.12	0.30
D	$128\times256\times512$	2.1	67	3.00	1.00	2.03×10^7	4.55×10^7	32	98	32	3.5	26	29	0.003	0.007	0.008	0.01
E	$128\times256\times512$	2.9	78	3.50	1.00	2.64×10^7	3.11×10^7	25	90	25	5.0	24	87	0.06	0.06	0.18	0.17
F1	$128\times256\times512$	4.3	66	3.00	1.00	8.10×10^7	3.31×10^7	28	86	28	7.9	23	33	0.01	0.04	0.06	0.15
F2	$144\times288\times576$	4.3	57	1.00	1.00	1.17×10^8	1.29×10^7	33	33	33	8.3	19	37	0.03	0.06	0.13	0.24
F3	$144\times288\times576$	4.3	58	0.25	1.00	1.17×10^8	9.00×10^5	27	6	27	9.8	18	49	0.02	0.07	0.10	0.28
G^a	$256\times512\times1024$	4.9	43	1.20	1.00	3.47×10^8	4.55×10^7	50	61	50	9.3	21	37	0.03	0.04	0.03	0.10
G^W	$180\times256\times128$	4.8	67	2.00	1.00	1.25×10^8	4.00×10^7	34	68	34	8.3	31	22	0.05	0.07	0.21	0.29
H	$128\times256\times512$	7.1	69	3.00	1.00	2.25×10^8	2.04×10^7	24	72	24	15.6	21	200	0.01	0.03	0.10	0.20
H^a	$256\times512\times1024$	7.8	51	1.40	1.00	6.61×10^8	5.21×10^7	40	56	40	16.1	18	36	0.004	0.014	0.03	0.10
I	$128\times256\times512$	9.6	71	2.08	1.04	4.63×10^8	3.93×10^7	26	55	27	20.4	28	52	0.01	0.03	0.11	0.23
I^W	$128\times256\times128$	9.6	71	2.08	1.04	4.63×10^8	3.83×10^7	27	56	28	19.9	28	20	0.01	0.02	0.11	0.20
J	$128\times256\times512$	14.5	62	2.50	1.00	1.30×10^9	1.12×10^7	25	63	25	36.1	18	62	–0.001	0.01	0.01	0.14
J^W	$180\times256\times128$	15.5	69	2.00	1.00	1.30×10^9	3.93×10^7	21	43	21	41.7	26	53	0.004	0.009	0.05	0.13
K1	$128\times256\times512$	21.4	74	3.00	1.00	2.03×10^9	1.00×10^7	16	50	16	67.5	13	18	–0.001	0.007	0.03	0.15
K2	$128\times256\times512$	21.4	55	2.25	1.00	3.60×10^9	1.56×10^7	21	48	21	71.2	13	18	–0.001	0.005	0.03	0.11
L^a	$256\times512\times1024$	23.3	60	1.60	1.00	4.6×10^9	4.58×10^7	21	32	21	83.4	15	51	1×10^{-4}	0.002	0.003	0.04
L^W	$180\times256\times128$	23.3	70	2.00	1.00	2.92×10^9	4.00×10^7	16	33	16	82.4	24	53	-1×10^{-4}	0.003	0.002	0.07
M	$128\times256\times512$	28.5	61	2.50	1.00	5.18×10^9	6.00×10^6	18	46	18	98.7	9	24	–0.001	0.003	0.02	0.10
M^a	$256\times512\times1024$	28.5	31	2.50	1.00	2.07×10^{10}	1.48×10^5	33	82	33	109.9	15	33	-7×10^{-5}	9×10^{-4}	0.002	0.03
M^W	$180\times256\times128$	31.0	71	2.00	1.00	5.18×10^9	1.03×10^8	14	28	14	126.5	21	49	-1×10^{-4}	0.002	0.003	0.07

Notes. The quantities in the Cols. (2) to (8) are input parameters of the runs whereas the quantities from Cols. (9) to (18) are outcomes of the simulations. Superscripts a denote high-resolution runs and superscripts W denote $\pi/2$ wedges. The horizontal line denotes the transition from axisymmetric (antisolar) magnetic field (rotation profile) to a nonaxisymmetric (solar) field (rotation profile). The Δt value indicates the time span of the saturated stage in years. The $\Delta_\Omega^{(r)}$ and $\Delta_\Omega^{(\theta)}$ values indicate the relative radial and latitudinal differential rotation, see Eq. (16), whereas $|\Delta\Omega_r|$ and $|\Delta\Omega_\theta|$ are the absolute radial and latitudinal differential rotation; see Eq. (17).

Käpylä et al. (2017), whereas Run E corresponds to Set E in Käpylä et al. (2017) and Run B1 in Warnecke et al. (2016). We also include a selection of models (Runs A2, C3, F3) with a lower $\mathrm{Pr_{SGS}}$ to compare with other studies in which such parameter regimes are explored (e.g., Brown et al. 2010; Nelson et al. 2013; Fan & Fang 2014; Hotta et al. 2016). The numerical studies were carried out over an extended period of time, during which the setups have been continuously refined. This, and the aim to compare to other studies, explains the heterogeneity in the choice of parameters. The physical run time of the saturated stage is denoted by Δt.

3.1. Overview of convective states

All our models have a density stratification that is much smaller than in the Sun. Therefore, the effects of small-scale convection near the surface and the resulting low local Coriolis numbers in those layers are not captured. This can be achieved only at very high resolution (e.g., Hotta et al. 2014) and is not feasible for parameter studies, such as those carried out in this work. Thus, the effects of rotation are more strongly imprinted in the velocity field near the surfaces of our models than what is expected in actual stars. This is manifested in Fig. 1 where the radial velocity u_r is shown for several runs with increasing rotation rate. The size of the convection cells at high latitudes decreases as the rotation rate is increased. Also, we observe the appearance of elongated in latitude columnar structures near the equator at about twice the solar rotation rate. These structures, often referred to as banana cells, persist for all higher rotation rates investigated, their azimuthal and radial extents reducing as a function of rotation, while the latitudinal extent remains roughly constant. The reason for their emergence is the strong rotational influence on the flow and the geometry of the system. Strong rotation tries to force convection into Taylor–Proudman balance resulting in columnar cells that are aligned with the rotation vector. Such cells are connected over the equator only outside the tangent cylinder in a spherical shell, manifesting themselves as elongated structures at low latitudes. Such convective modes can also lead to equatorial acceleration as observed in the simulations and in the Sun (Busse 1970). In the Sun, the small-scale granulation near the surface masks direct observation of larger scale convective modes. However, helioseismic results also suggest that large-scale convective structures exceeding the supergranular scale of 20–30 Mm are weak (e.g., Hanasoge et al. 2012).

To quantify the size of convective structures as a function of rotation we compute the power spectra of the radial velocity near the surface; see Fig. 2. We use a spherical harmonics decomposition to calculate the coefficients $\hat{u}_r^{\ell m}$, where ℓ, m are the order of the spherical harmonics and the azimuthal number, respectively. The details on the decomposition can be found in Appendix A. The power at each ℓ is

$$P = \frac{E_{\rm kin}^{(\ell)}}{\sum_\ell E_{\rm kin}^{(\ell)}}, \quad E_{\rm kin}^{(\ell)} = \sum_{m=0}^{\ell} C_m |\hat{u}_r^{\ell m}|^2, \tag{12}$$

where $C_m = 2 - \delta_{m0}$. We find that for more rapid rotation the radial kinetic energy peaks at smaller scales (higher ℓ, close

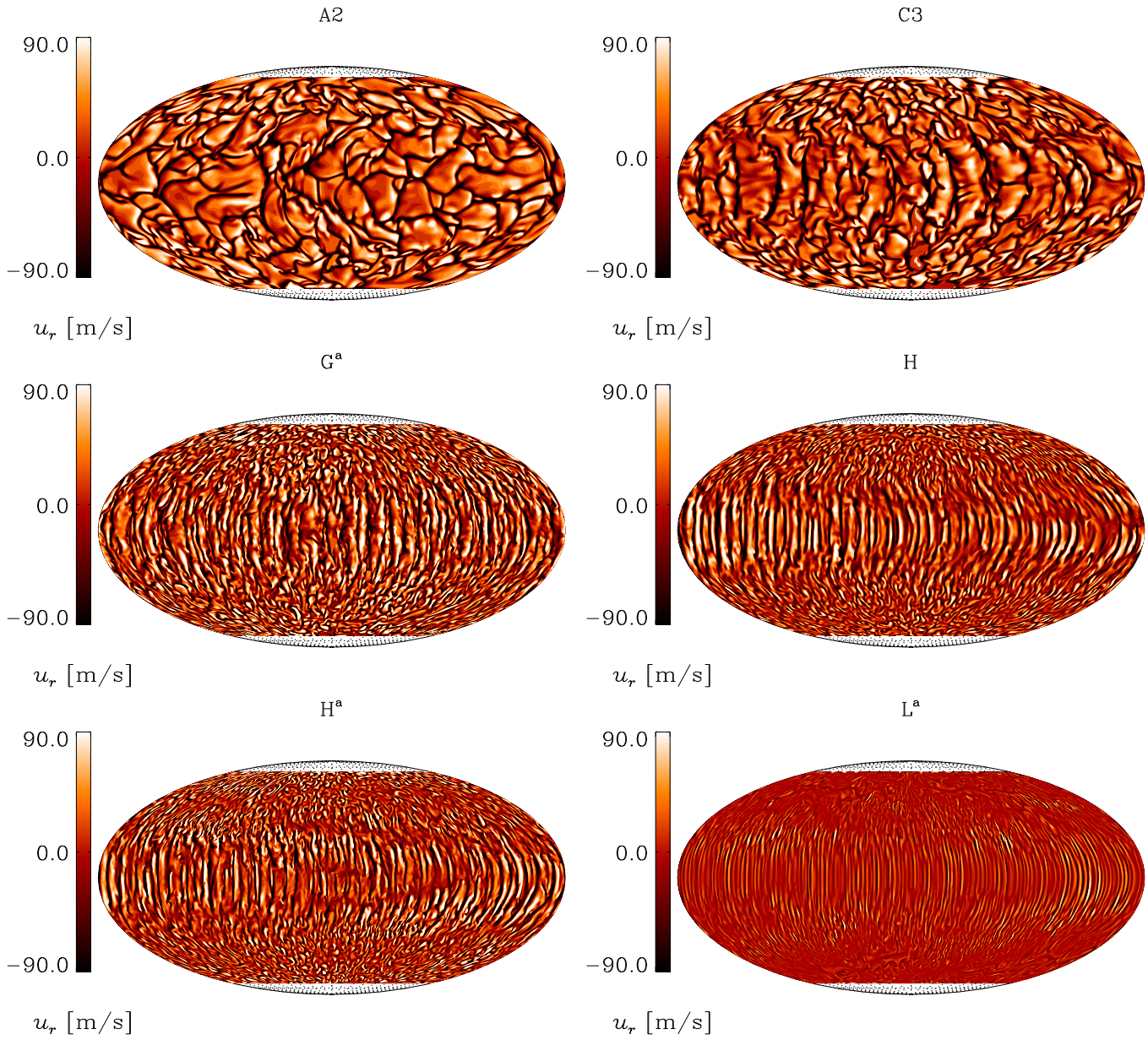

Fig. 1. Mollweide projection of radial velocity u_r at $r = 0.98\,R$ for Runs A2, C3, G^a, H, H^a, and L^a.

to $\ell = 100$ for Run L^a) and the kinetic energy at large scales (lower ℓ) becomes smaller; see Fig. 2a. The increasing rotational influence is clearly seen in Fig. 2b, where we plot the value of ℓ at the maximum of the radial velocity spectra as a function of the Coriolis number for all runs. The dependence is consistent with a power law with $\mathrm{Co}^{0.26}$, which is relatively close to the theoretically expected 1/3 scaling for rotating hydrodynamic convection near onset (Chandrasekhar 1961). This is shallower than the slope of about 1/2 found for the horizontal velocity spectra in the simulations of Featherstone & Hindman (2016a). When we only consider the high-resolution runs (blue line in Fig. 2b), we observe a steeper trend ($\mathrm{Co}^{0.46}$). Especially at rapid rotation, the high-resolution runs start deviating significantly from their low-resolution counterparts, and the scale of convection is reduced much more strongly in the former class of runs.

To look at the energy of the radial velocity field at different values of m, we decompose it at the surface, as described in Appendix A. In Fig. 3 we plot the kinetic energy for $0 \leq \ell \leq 10$. The total kinetic energy at the surface is decreasing with rotation (panel a), and most of the kinetic energy is contained in the small scales (panel b, orange line). While the fifth nonaxisymmetric mode is mostly constant with increasing rotation (red line), the axisymmetric mode ($m = 0$) varies strongly and sometimes has comparable or even higher energy than $m = 5$.

Nonaxisymmetric structures in the velocity field are also visible in Fig. 1 around the equator, in particular for Run L^a. This is in agreement with previous studies (e.g., Brown et al. 2008), which reported the presence of clear nonaxisymmetric large-scale flows for hydrodynamic simulations in parameter regimes near the onset of convection. These localized nonaxisymmetric structures are similar to the relaxation oscillations, first seen in planetary simulations. Those are explained by realizing that, at intermediate Rayleigh numbers, differential rotation tends to suppress the convective cells and, as a result, they localize in groups across longitude, leaving the rest of the azimuthal domain dominated by the axisymmetric differential rotation.

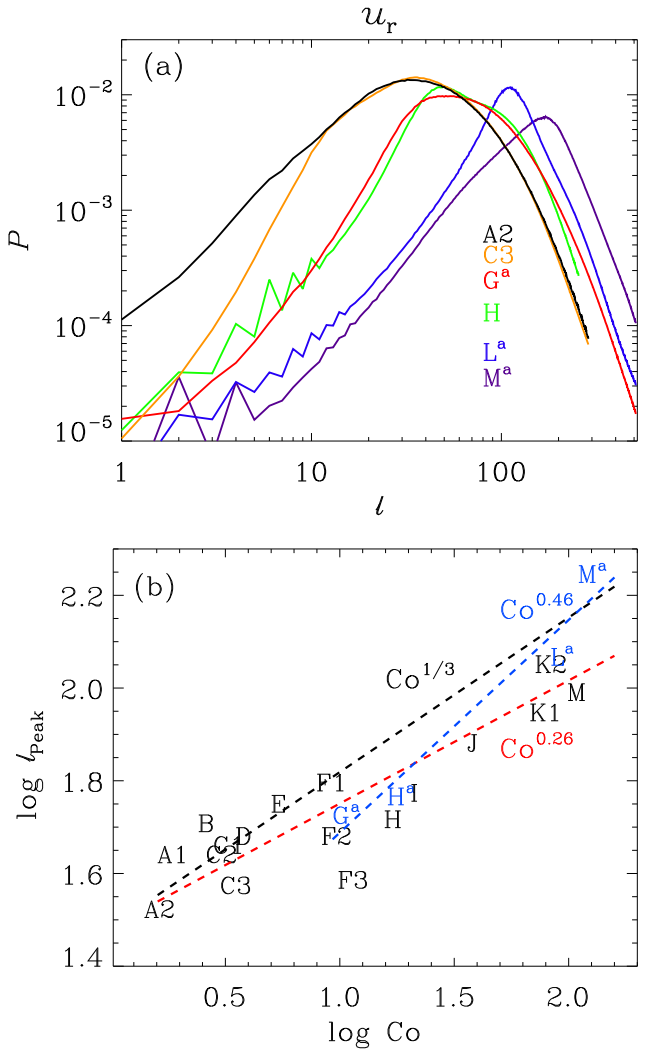

Fig. 2. *Panel a*: normalized power spectra P of the radial velocity as function of degree ℓ for Runs A2, C3, G^a, H, L^a, and M^a with increasing rotational influence. *Panel b*: degree of peak power $\ell_{\rm peak}$ estimated from the power spectra plotted over Coriolis number Co. The runs are indicated with their run names. The red dashed line represents a power law fit including all the runs; the blue dashed line represents the fit for the high-resolution runs, while the black dashed line indicates the expected slope from theoretical estimates (Chandrasekhar 1961).

3.2. Mean flows

To estimate the rotational influence on the convection we also calculated the volume averaged total kinetic energy density and its contributions; see Table 2. The total kinetic energy density is given by

$$E_{\rm kin} = \left\langle \tfrac{1}{2}\rho \boldsymbol{u}^2 \right\rangle_V , \tag{13}$$

and the contributions contained in differential rotation and meridional circulation are, respectively,

$$E_{\rm kin}^{\rm DR} = \left\langle \tfrac{1}{2}\rho \overline{u}_\phi^2 \right\rangle_V , \quad E_{\rm kin}^{\rm MC} = \left\langle \tfrac{1}{2}\rho \left(\overline{u}_r^2 + \overline{u}_\theta^2\right) \right\rangle_V . \tag{14}$$

The contribution from the nonaxisymmetric flows is

$$E_{\rm kin}^{\rm fluc} = E_{\rm kin} - \left(E_{\rm kin}^{\rm DR} + E_{\rm kin}^{\rm MC}\right). \tag{15}$$

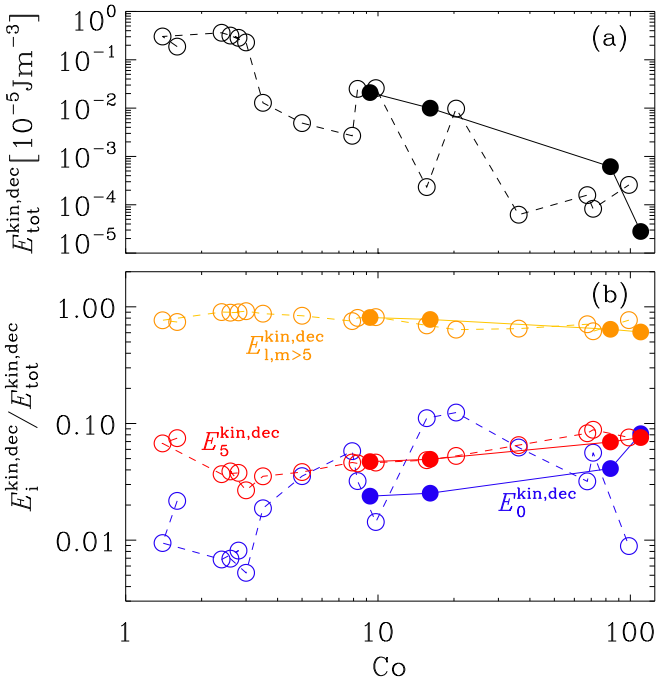

Fig. 3. Kinetic energy of the decomposition as a function of Coriolis number Co for all 2π runs showing the total energy (*panel a*), axisymmetric ($m = 0$, blue), fifth nonaxisymmetric mode ($m = 5$, red), and small-scale ($l, m > 5$, orange) contribution (*panel b*). All the energies in *panel b* are normalized to the total energy (*panel a*). Filled circles connected by a continuous line indicate high-resolution runs.

The total kinetic energy decreases nearly monotonically as a function of rotation. This clearly shows the rotational quenching of convection, which is related to an increasing critical Rayleigh number in rapidly rotating systems. As a result, the system becomes less supercritical for convection the higher the rotation rate, which is also reflected in the monotonous decrease of the nonaxisymmetric energy that also contains the fluctuations due to convective turbulence. The energy contained in differential rotation and meridional circulation shows a decreasing overall trend as a function of rotation. In general, the capability of the flow to extract energy from thermal energy is decreased by rotation. Comparison to $\pi/2$ wedge simulations indicates some differences in the dynamics of the flow, but it is hard to discern any systematic behavior. For a moderate rotation Run G, the $\pi/2$ wedge (Run G$^{\rm W}$) has an excess of every type of kinetic energy, while in the rapid rotation regime (Runs I, J, L, M) the flow energies have a tendency to be lower than in the corresponding runs with full azimuthal extent.

3.3. Differential rotation

The rotation also influences the generation of mean flows as for example the differential rotation. To illustrate this, we plot the profiles of angular velocity, $\Omega(r,\theta) = \overline{u}_\phi(r,\theta)/r\sin\theta + \Omega_0$, for six representative runs (Runs A2, C3, G^a, H, H^a, and L^a) in Fig. 4. We find antisolar differential rotation for the solar rotation rate (Runs A1 and A2), which is consistent with previous numerical studies (e.g., Gastine et al. 2014; Käpylä et al. 2014). This might be due to the overall convective velocities that are too high or the concentration of power that is too high at large spatial scales (Featherstone & Hindman 2016b) in the simulations in comparison to the Sun. The antisolar rotation switches to solar-like at slightly more rapid rotation corresponding to

Table 2. Volume averaged kinetic and magnetic energy densities in units of 10^5J m^{-3}.

Run	$E_{\rm kin}$	$E_{\rm kin}^{\rm DR}$	$E_{\rm kin}^{\rm MC}$	$E_{\rm kin}^{\rm fluc}$	$E_{\rm mag}$	$E_{\rm mag}^{\rm tor}$	$E_{\rm mag}^{\rm pol}$	$E_{\rm mag}^{\rm fluc}$
A1	4.428	1.152	0.015	3.261	0.876	0.050	0.055	0.771
A2	5.055	0.858	0.015	4.182	0.995	0.047	0.055	0.893
B	3.263	0.358	0.005	2.901	0.715	0.055	0.037	0.623
C1	3.153	0.164	0.003	2.986	0.504	0.035	0.026	0.442
C2	3.631	0.128	0.003	3.500	0.488	0.028	0.023	0.438
C3	6.572	3.941	0.003	2.628	0.891	0.177	0.023	0.692
D	3.181	0.873	0.003	2.305	0.671	0.042	0.012	0.617
E	4.189	2.317	0.001	1.871	0.579	0.073	0.023	0.483
F1	2.485	0.842	0.002	1.642	1.363	0.166	0.017	1.181
F2	2.898	1.101	0.002	1.794	1.082	0.088	0.023	0.971
F3	2.700	1.263	0.001	1.437	0.767	0.208	0.018	0.541
G^a	2.748	0.820	0.001	1.926	0.754	0.076	0.014	0.664
G^W	3.506	1.653	0.003	1.851	0.986	0.193	0.132	0.661
H	2.153	0.845	0.001	1.306	1.049	0.058	0.028	0.963
H^a	1.704	0.354	0.001	1.349	1.449	0.111	0.029	1.309
I	1.706	0.570	0.001	1.135	1.361	0.065	0.036	1.260
I^W	1.625	0.483	0.001	1.141	1.197	0.247	0.230	0.720
J	0.580	0.346	0.000	0.234	0.113	0.024	0.006	0.083
J^W	0.786	0.101	0.000	0.685	0.900	0.102	0.230	0.568
K1	2.325	1.624	0.000	0.701	0.426	0.216	0.025	0.185
K2	1.549	0.934	0.000	0.615	1.029	0.358	0.153	0.518
L^a	0.708	0.155	0.000	0.552	1.928	0.031	0.018	1.878
L^W	0.415	0.023	0.000	0.391	1.102	0.129	0.393	0.580
M	2.053	1.433	0.000	0.620	0.967	0.337	0.152	0.477
M^a	0.393	0.008	0.000	0.385	2.793	0.057	0.062	2.674
M^W	0.328	0.025	0.000	0.303	1.024	0.138	0.407	0.479

Co = 3.0. For higher rotation rates the differential rotation develops a minimum at mid-latitudes. Such a configuration has been shown to be important in producing equatorward migrating magnetic activity (Warnecke et al. 2014). We also find such minima at moderate rotation, up to roughly seven times solar rotation rate (Run H). At higher rotation rates very little differential rotation is generated overall and the mid-latitude minimum becomes progressively weaker.

We quantify the relative radial and latitudinal differential rotation using

$$\Delta_\Omega^{(r)} = \frac{\Omega_{\rm eq} - \Omega_{\rm bot}}{\Omega_{\rm eq}} \text{ and } \Delta_\Omega^{(\theta)} = \frac{\Omega_{\rm eq} - \Omega_{\rm pole}}{\Omega_{\rm eq}}, \tag{16}$$

where $\Omega_{\rm eq} = \Omega(R, \pi/2)$ and $\Omega_{\rm bot} = \Omega(0.7R, \pi/2)$ are the angular velocities at the top and bottom of the convection zone at the equator, respectively, and $\Omega_{\rm pole} = [\Omega(R, \theta_0) + \Omega(R, \pi - \theta_0)]/2$ is the time averaged angular velocity at the latitudinal boundaries. Negative or positive values of $\Delta_\Omega^{(\theta)}$ indicate antisolar (fast poles, slow equator) or solar-like (fast equator, slow poles) differential rotation, respectively. In Table 1 we list these numbers from our simulations and notice that a transition from strong antisolar to significantly weaker solar-like differential rotation occurs at about $\tilde{\Omega} \approx 1.8$ (Co $\approx$ 3; Run C3). We also plot $\Delta_\Omega^{(r)}$ and $\Delta_\Omega^{(\theta)}$ as functions of Co for all the 2π runs in Fig. 5. There, we indicate the transition point with a vertical dashed line. As we later discuss in detail, this point also marks the change of the dynamo modes from axisymmetric to nonaxisymmetric. From this plot it is evident that, as the rotation increases, both relative differential rotation measures approach zero. From Tables 1 and 2 we also see that near the transition, the rotation profile is sensitive to changes in the convective efficiency, as indicated by the Rayleigh number. In Run C3 with a low $\mathrm{Pr_{SGS}}$ and lower Rayleigh and Reynolds numbers than in the more turbulent Runs C1 and C2, the rotation profile is solar-like, while in the others it is antisolar. This transition and its sensitivity to the efficiency of convection has been studied in detail by, for example, Gastine et al. (2014) and Käpylä et al. (2014).

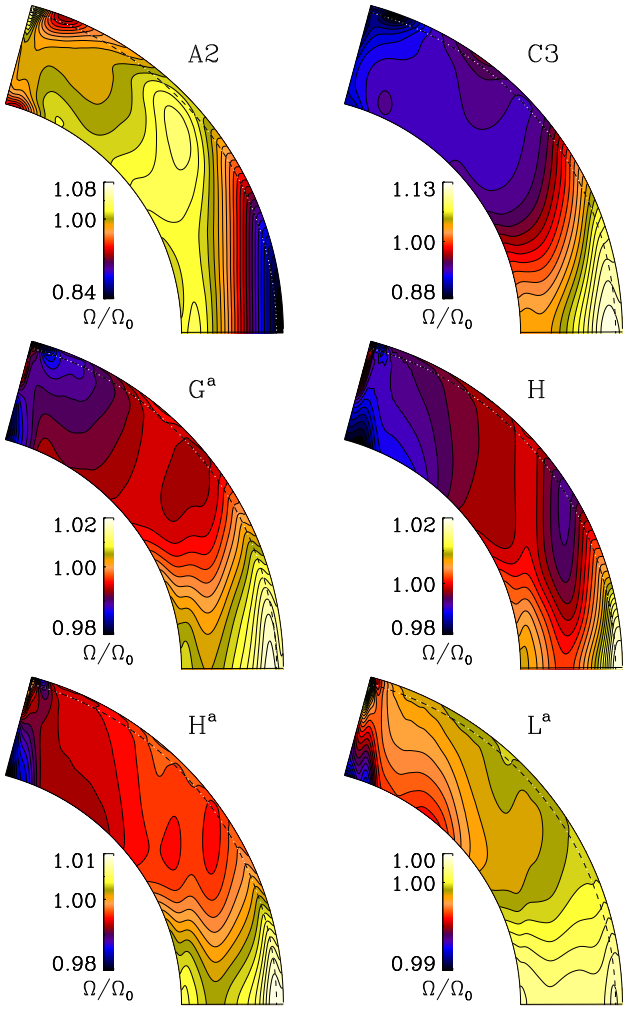

Fig. 4. Normalized angular velocity $\Omega(r, \theta)$ of Runs A2, C3, G^a, H, H^a, and L^a. The dashed lines denote the radius $r = 0.98\,R$, which is used for the further analysis.

We note that $\Delta_\Omega^{(r)}$ and $\Delta_\Omega^{(\theta)}$ measure only the difference between certain points and neglect the actual latitudinal variation, which can be more complicated. In the case of wedge geometry the flows near the latitudinal boundaries may not be representative of what takes place at high latitudes in real stars. This can lead to unrepresentative results, in particular for the latitudinal differential rotation in cases where the latitudinal profile is non-monotonic (cf. Karak et al. 2015).

The antisolar regime typically shows strong negative radial and latitudinal shear (Gastine et al. 2014), whereas magnetic fields tend to quench the differential rotation (e.g., Fan & Fang 2014; Karak et al. 2015). Our results are in agreement with those aforementioned studies. Another important aspect is the dependence of absolute differential rotation, defined as

$$\Delta\Omega_r = \Delta_\Omega^{(r)}\tilde{\Omega}, \quad \Delta\Omega_\theta = \Delta_\Omega^{(\theta)}\tilde{\Omega}, \tag{17}$$

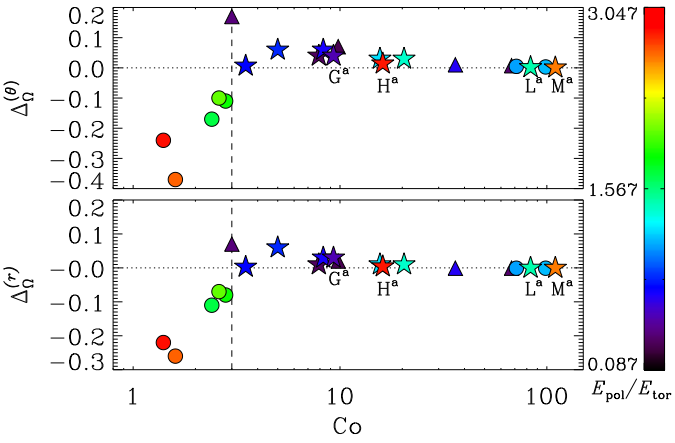

Fig. 5. Relative latitudinal differential rotation $\Delta_\Omega^{(\theta)}$ (*upper panel*) and relative radial differential rotation $\Delta_\Omega^{(r)}$ (*lower panel*) for all 2π runs. The shape of the plotted symbols indicates the degree of nonaxisymmetry of the magnetic field (sphere – axisymmetric; triangle – mixed; star – nonaxisymmetric), while the color indicates the ratio of poloidal energy $E_{\rm mag}^{\rm pol}$ to toroidal energy $E_{\rm mag}^{\rm tor}$; see Table 2. The dashed line (Co = 3) indicates the transition from antisolar to solar-like latitudinal differential rotation and the dotted lines indicate the zero. The high-resolution runs G^a, H^a, L^a, and M^a are indicated for better visibility.

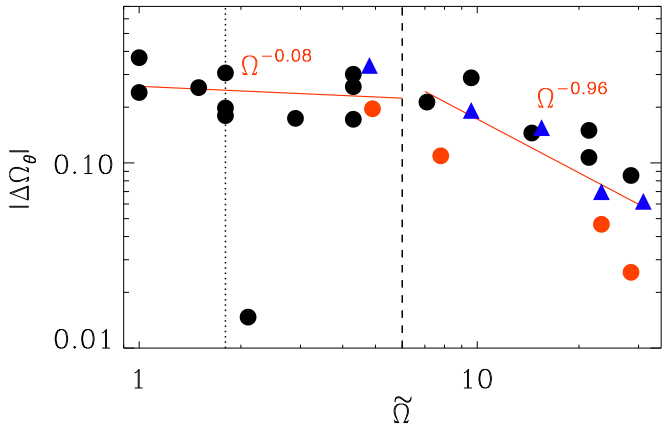

Fig. 6. Modulus of the absolute latitudinal differential rotation, $\Delta\Omega_\theta = \Delta_\Omega^{(\theta)}\Omega_0$, normalized by the solar rotation rate, as a function of rotation rate. The red lines result from fitting. The black dashed line indicates the break in the slope. Red and black circles stand for high- and low-resolution 2π runs, respectively, while blue triangles show the $\pi/2$ wedges. We note that for the fit for moderate rotation, we do not take into account Run D with very low values. The dotted line indicates the transition from antisolar to solar-like latitudinal differential rotation.

on the rotation rate itself. The broad range of probed rotation rates allows us to search for a power-law behavior of the form

$$|\Delta\Omega_\theta| \propto \Omega^q. \tag{18}$$

In Fig. 6, we do not find, however, a single power law that would describe the behavior at all rotation rates. For slow and moderate rotation, up to $\tilde{\Omega} \approx 5$, we fit a slope of $q \approx -0.08$, while for the highest rotation rates investigated, $\tilde{\Omega} \approx 5$–31, we find a steeper power law with $q \approx -0.96$.

In Table 3, we compare our results with those of some observational studies (Reinhold & Gizon 2015; Lehtinen et al. 2016) and a mean-field model (Kitchatinov & Rüdiger 1999). Our results for the low to intermediate rotation rates agree with these studies, but the power law we find for the rapid rotation regime

Table 3. Scaling of absolute differential rotation with rotation of some recent observational studies, models, and our work using the exponent q; see Eq. (18).

q	Reference
−0.08	This work (slow rotation)
−0.96	This work (rapid rotation)
−0.36	Lehtinen et al. (2016)
+0.29	Reinhold & Gizon (2015)
−0.15 (G2, mean)	Kitchatinov & Rüdiger (1999)
−0.04 (K5, mean)	Kitchatinov & Rüdiger (1999)

is much steeper and therefore in disagreement with them. This disagreement cannot be explained by the lack of supercriticality as the high-resolution runs show even weaker latitudinal differential rotation than their low-resolution counterparts. However, the magnetic fields in the rapidly rotating high-resolution runs (H^a, L^a, and especially in M^a) are generally stronger than in the lower resolution runs, possibly also contributing to the reduced differential rotation (cf. Käpylä et al. 2017).

3.4. Overview of magnetic states

All the runs discussed in this work produce large-scale magnetic fields. Similar runs were recently analyzed by Warnecke et al. (2018) using the test-field method, which measured significant turbulent effects contributing to the magnetic field generation. Therefore, we attribute the magnetic fields seen in the current runs to the turbulent dynamo mechanism. To describe the magnetic solutions, we first look at the volume-averaged magnetic energy densities. We define these densities analogously to their kinetic counterparts. We use

$$E_{\rm mag} = \left\langle \boldsymbol{B}^2 \right\rangle_V / 2\mu_0, \tag{19}$$

for the total magnetic energy density,

$$E_{\rm mag}^{\rm tor} = \left\langle \overline{B}_\phi^2 \right\rangle_V / 2\mu_0, \quad E_{\rm mag}^{\rm pol} = \left\langle \overline{B}_r^2 + \overline{B}_\theta^2 \right\rangle_V / 2\mu_0, \tag{20}$$

for the contribution of mean toroidal and mean poloidal fields, and

$$E_{\rm mag}^{\rm fluc} = E_{\rm mag} - (E_{\rm mag}^{\rm tor} + E_{\rm mag}^{\rm pol}), \tag{21}$$

for the contribution of fluctuating magnetic fields. These quantities are listed in Table 2. We find that for all the runs, the contributions from fluctuating magnetic fields dominate the magnetic energy. The axisymmetric contributions contain on the order of 5% to 10% of the total magnetic energy in the majority of the runs, and exceeds 15% only in Runs C3, F3, K1, and K2. These runs are characterized either by a low $\mathrm{Pr}_{\rm SGS}$ (C3 and F3) or rapid rotation (K1 and K2), both leading to reduced supercriticality of convection.

In contrast to the kinetic energy, we do not find a clear trend for magnetic energies as a function of rotation rate. In the rapid rotation regime, the high-resolution runs L^a and M^a exhibit magnetic fields with an energy that significantly exceeds the kinetic energy by factors of roughly 3 and 8, respectively. If we look at the radial profile of the magnetic energy density for a selection of runs (Fig. 7), we find that the magnetic field in the upper half of the convection zone increases with rotation. As discussed earlier, we observe a simultaneous, nearly monotonic, decrease

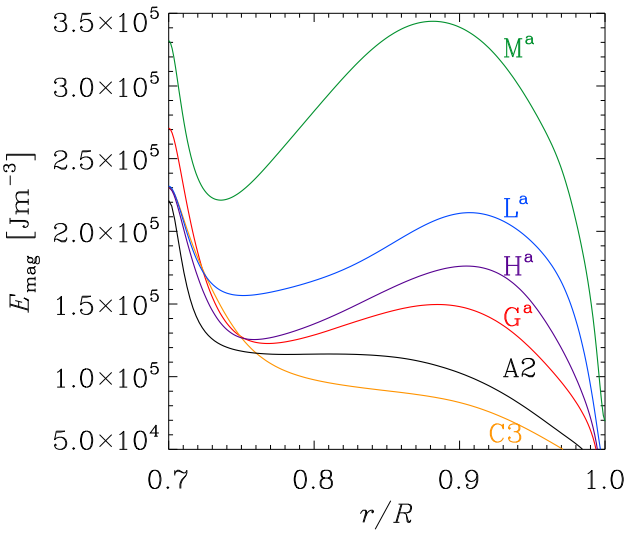

Fig. 7. Radial profiles of the total magnetic energy density $E_{\rm mag}$ averaged over time, latitude, and azimuth for Runs A2, C3, G^a, H^a, L^a, and M^a.

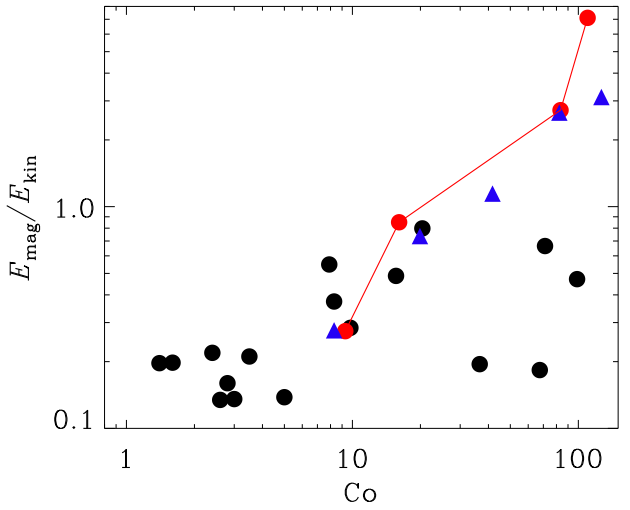

Fig. 8. Ratio of total magnetic to kinetic energies $E_{\rm mag}/E_{\rm kin}$ as a function of Coriolis number Co. The red filled symbols (connected by a line) denote high-resolution runs. Blue triangles refer to $\pi/2$ wedge runs.

of the kinetic energy as a function of rotation rate. Therefore, the ratio of the magnetic to kinetic energies, which is a measure of the dynamo efficiency, is actually steeply increasing as a function of rotation, as can be seen from Fig. 8. We find that in the low-resolution cases the dynamo is clearly less efficient in the rapid rotation regime in comparison to the high-resolution cases. We also observe that the $\pi/2$ wedge runs produce a far more efficient dynamo in the rapid rotation regime than the corresponding low-resolution runs with full azimuthal extent. This is possibly explained by the somewhat higher stratification and Rayleigh numbers in the $\pi/2$ wedge runs in comparison to those in the low-resolution full 2π models. We can conclude that the convective efficiency directly influences the dynamo efficiency and therefore, the magnetic energy production.

In Fig. 5 we studied the dependence of the overall magnetic topology on the amount of differential rotation generated in the system. The ratio of poloidal to toroidal magnetic energies, shown with the color of the symbols, changes systematically from mostly poloidal field configurations at very low rotation rates to toroidal field configurations at moderate and rapid rotation. The energy ratio gradually decreases, and with rotation rates exceeding the antisolar to solar transition point, dominantly toroidal fields are seen. The strongest toroidal fields are generated for moderate rotation. At the highest rotation rates, the ratio of toroidal and poloidal becomes again lower in the high-resolution runs, while the low-resolution counterparts fail to show systematic behavior. In the run with the highest rotation rate, M^a, the poloidal component again dominates. By inspecting Table 2, we notice that the models with reduced ϕ extent tend to produce a larger poloidal to toroidal energy ratio than the corresponding runs covering the full azimuthal extent.

To investigate the spatial structure of the magnetic field, we show in Fig. 9 snapshots of B_r for six representative runs. At low rotation rates, most of the magnetic field is concentrated in the downflows between the convective cells, while at high rotation rates, the scale of convection, still clearly affecting the magnetic field, thereby leaving a small-scale imprint on it, is significantly reduced. Nevertheless, global-scale magnetic field configurations clearly emerge in the high-latitude regions. It is immediately apparent that a nonaxisymmetric large-scale pattern is visible in all cases. In the slowly rotating cases, the nonaxisymmetric component is subdominant and the equatorial symmetry of the field is clearly dipolar (antisymmetric with respect to the equator). In all the runs with solar-like differential rotation, however, the field configuration is observed to be symmetric (or quadrupolar) with respect to the equator, even though a more detailed analysis revealed that the parity of the solutions is not pure. A weaker antisymmetric (dipolar) component is present at all times and the global parity undergoes some fluctuations. The quadrupolar component remains most significant at all times, however. This result is in agreement with some ZDI measurements of solar-like stars (e.g., Hackman et al. 2016; Rosén et al. 2016). However, we should point out that our results can be influenced by the wedge assumption in latitude and need to be verified in full spherical geometry.

We also depict the overall nonaxisymmetry of the large-scale magnetic field solutions with the shape of the symbol in Fig. 5. Again, on the lower rotation side of the break point identified, the magnetic fields are mostly axisymmetric (circular symbol). On the rapid rotation side, the fields exhibit a significant nonaxisymmetric component (triangles) and finally turn into completely nonaxisymmetric components (stars). The resolution also plays a significant role in the nonaxisymmetry measure. The higher resolution runs show preferentially nonaxisymmetric configurations, while the lower resolution runs turn back to axisymmetry at the highest rotation rates investigated.

3.5. Degree of nonaxisymmetry

Large-scale nonaxisymmetric magnetic fields, as seen in Fig. 9, are included in the definition of $E_{\rm mag}^{\rm fluc}$ in Table 2, as this quantity is the difference between total and azimuthally averaged (mean) magnetic energies. This term, therefore, contains both small-scale fluctuations and large-scale nonaxisymmetric contributions. Thus, the diagnostics introduced so far only roughly describe the large-scale fields in the system.

To obtain a more complete picture, we perform a spherical harmonics decomposition of the radial components of the vector fields at $r = 0.98\,R$ with the method described in Appendix A. The $m = 0$ mode contains the axisymmetric (mean) part of the radial magnetic field, the $m = 1$ is the first nonaxisymmetric mode, $m = 2$ is the second mode, and so on. For the $\pi/2$ wedges, the first nonaxisymmetric mode is $m = 4$. The energies

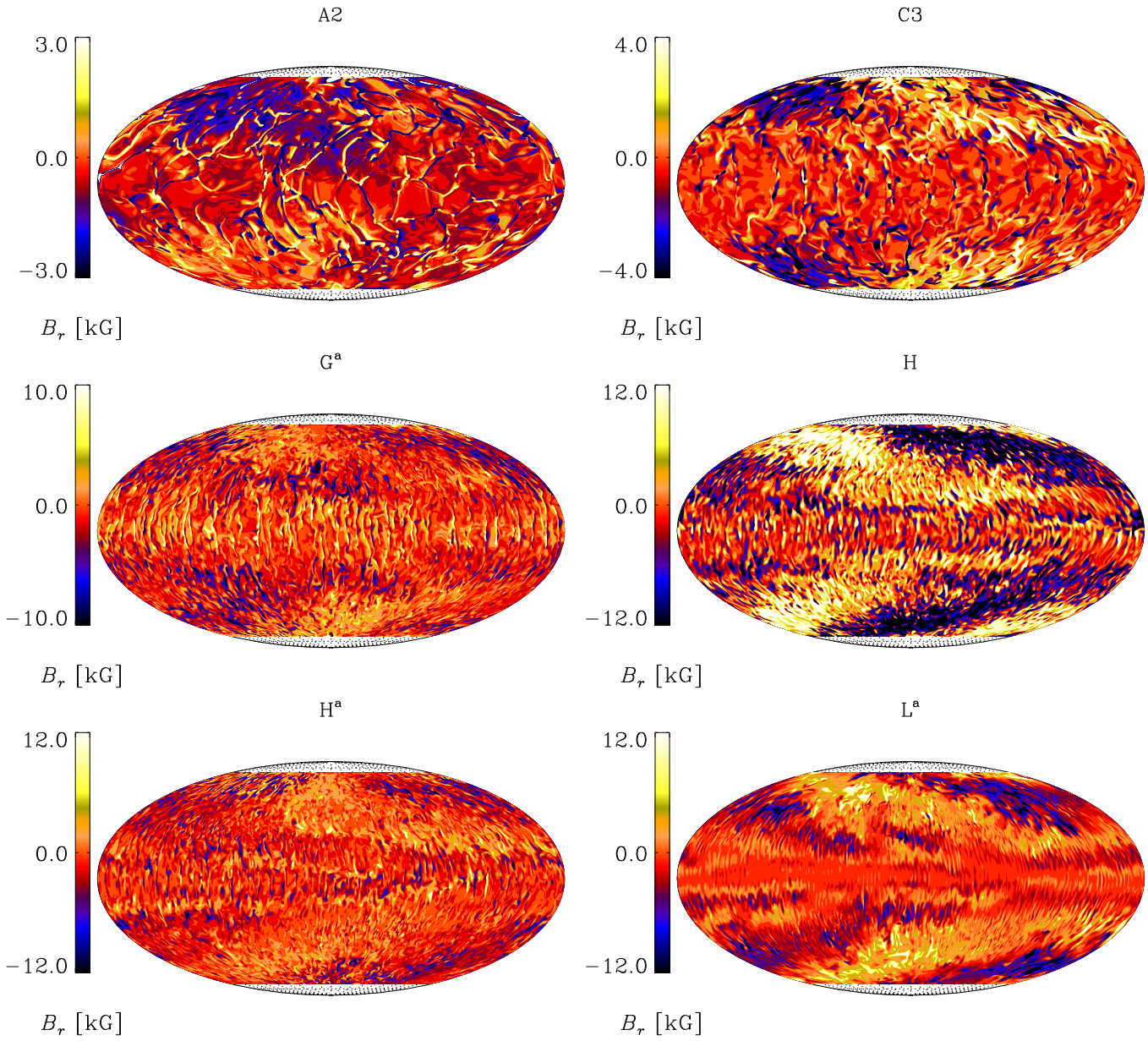

Fig. 9. Radial magnetic field B_r at $r = 0.98\,R$ from the same runs as in Fig. 1.

of the modes resulting from the decomposition are listed in Table 4. Depending on the dominant large-scale component, we call the magnetic fields nonaxisymmetric or axisymmetric even though their small-scale contributions, which are always nonaxisymmetric, might be more energetic.

The distribution of the radial magnetic energy density near the surface of the star is presented in Fig. 10a as a function of Co. We show the axisymmetric and magnetic energy in the large-scale nonaxisymmetric field ($1 \le \ell \le 5$) normalized by the total magnetic energy. We find an inversion between the energies in the axisymmetric and nonaxisymmetric components, which also coincides with the transition from antisolar- to solar-like differential rotation at Co $\approx$ 3. The runs show a nonaxisymmetric magnetic field until Co $\approx$ 70, but at higher Co the high-resolution runs remain nonaxisymmetric, while the low-resolution runs return to an axisymmetric configuration, indicating that high resolution is needed at such high rotation rates to capture the small scales. This could explain the lack of nonaxisymmetric solutions in the study of Brown et al. (2010). This conjecture is supported by the fact that in the higher resolution simulations of Nelson et al. (2013) significantly clearer nonaxisymmetric features are seen (their Figs. 4–6), although they are confined to low latitudes. Those simulations were made with $\tilde{\Omega} = 3$, albeit with a lower thermal Prandtl number and different viscosity and diffusivity profiles than in the current simulations (cf. Appendix A of Käpylä et al. 2017, for a comparison of different setups). Our Runs C3 and F3 also produce strong nonaxisymmetric large-scale fields at high latitudes despite their lower values of $\mathrm{Pr}_{\mathrm{SGS}}$. This could be an indication of the influence of the latitudinal boundaries in the current simulations.

The simulations of Fan & Fang (2014) and Hotta et al. (2016), on the other hand, used the solar rotation rate and a further decreased thermal Prandtl number resulting in a laminar heat transport to force a solar-like rotation profile. The large-scale magnetic fields in those simulations are characterized by

Table 4. Energy densities of the radial magnetic field and dynamo cycle properties.

Run	$E_{\rm mag}^{\rm surf}$	$E_{\rm mag,tot}^{\rm dec}$	$E_0^{\rm dec}$	$E_1^{\rm dec}$	$E_2^{\rm dec}$	$E_3^{\rm dec}$	$E_4^{\rm dec}$	$E_5^{\rm dec}$	$E_{l,m>5}^{\rm dec}$	$P_{\rm ADW}$ [yr]	$P_{\rm ADW}$ [P_0]	$P_{\rm ADW}$ [$P_{\rm DR}$]	D	$\tau_{\rm cyc}$ [yr]
A1	0.211	2.1(–2)	5.8(–3)	2.1(–3)	1.9(–3)	1.7(–3)	1.7(–3)	1.5(–3)	6.1(–3)					$3.72_{(m0)}$
A2	0.188	2.4(–2)	4.3(–3)	3.0(–3)	2.5(–3)	2.4(–3)	2.2(–3)	2.0(–3)	7.9(–3)					$4.13_{(m0)}$
B	0.183	2.3(–2)	7.3(–3)	3.0(–3)	1.6(–3)	1.6(–3)	1.5(–3)	1.3(–3)	6.8(–3)					$2.45_{(m0)}$
C1	0.137	1.7(–2)	5.7(–3)	3.9(–3)	1.3(–3)	1.2(–3)	1.1(–3)	9.2(–4)	3.5(–3)					$3.53_{(m0)}$
C2	0.128	1.6(–2)	4.7(–3)	3.2(–3)	1.5(–3)	1.2(–3)	1.0(–3)	8.4(–4)	3.2(–3)					$4.37_{(m0)}$
C3	0.142	2.4(–2)	3.5(–3)	1.2(–2)	2.3(–3)	1.7(–3)	1.3(–3)	1.0(–3)	2.8(–3)	19.53	474	44.83	R	$3.13_{(m0)}$
D	0.180	5.1(–2)	3.1(–3)	3.9(–2)	3.4(–3)	1.9(–3)	1.2(–3)	8.3(–4)	1.7(–3)	14.14	410	24.67	R	$18.25_{(m0)}$
E	0.147	3.1(–2)	2.9(–3)	2.1(–2)	2.4(–3)	1.4(–3)	9.4(–4)	6.0(–4)	9.9(–4)	39.87	1542	82.53	R	$10.31_{(m1)}$
F1	0.290	0.111	1.5(–3)	9.7(–2)	4.8(–3)	2.4(–3)	1.5(–3)	1.1(–3)	3.1(–3)	4.22	245	5.92	R	$6.68_{(m0)}$
F2	0.220	4.9(–2)	3.3(–3)	3.1(–2)	4.3(–3)	2.5(–3)	1.7(–3)	1.4(–3)	4.2(–3)	5.94	346	6.55	R	$8.05_{(m1)}$
F3	0.086	1.6(–2)	2.9(–3)	5.2(–3)	1.5(–3)	1.1(–3)	8.3(–4)	6.6(–4)	3.6(–3)	10.49	611	8.20	R	$5.74_{(m0)}$
G^a	0.254	5.5(–2)	4.0(–3)	3.4(–2)	5.4(–3)	2.9(–3)	2.0(–3)	1.4(–3)	5.0(–3)	8.93	583	8.60	R	$7.43_{(m1)}$
G^W	0.286	3.9(–2)	2.9(–2)	0.0	0.0	0.0	6.9(–3)	0.0	2.7(–3)					$2.37_{(m0)}$
H	0.053	2.2(–2)	1.1(–3)	1.8(–2)	1.1(–3)	5.5(–4)	3.9(–4)	2.9(–4)	7.2(–4)	42.69	1.9(+3)	12.15	R	$27.34_{(m1)}$
H^a	0.274	7.7(–2)	4.0(–3)	5.3(–2)	6.6(–3)	3.4(–3)	2.4(–3)	1.7(–3)	6.5(–3)	24.36	2.6(+3)	15.84	R	$7.17_{(m1)}$
I	0.274	0.107	8.9(–3)	8.2(–2)	6.0(–3)	3.2(–3)	2.1(–3)	1.5(–3)	3.7(–3)	11.66	1.5(+3)	7.07	R	$7.75_{(m1)}$
I^W	0.220	4.0(–2)	3.0(–2)	0.0	0.0	0.0	7.6(–3)	0.0	2.6(–3)					$4.44_{(m0)}$
J	0.014	2.0(–3)	2.0(–4)	4.9(–4)	4.3(–4)	2.7(–4)	1.6(–4)	1.1(–4)	3.8(–4)	6.0(+3)	5.4(+5)	382.59	SW, P	$8.25_{(m0)}$
J^W	0.421	0.129	7.2(–2)	0.0	0.0	0.0	4.6(–2)	0.0	1.1(–2)					$4.05_{(m0)}$
K1	0.025	3.7(–3)	5.7(–4)	6.8(–4)	1 .0(–3)	6.2(–4)	2.2(–4)	1.3(–4)	4.3(–4)	4.89	1.4(+3)	0.01	P	$1.24_{(m0)}$
K2	0.193	5.9(–2)	3.7(–2)	9.8(–3)	3.7(–3)	2.(–3)	1.7(–3)	1.5(–3)	3.3(–3)					$5.10_{(m0)}$
L^a	0.475	0.292	2.4(–3)	0.246	1.3(–2)	1.2(–2)	5.7(–3)	4.5(–3)	8.3(–3)	56.53	1.78(+4)	14.66	SW, R	$3.13_{(m1)}$
L^W	0.509	0.218	0.123	0.0	0.0	0.0	8.1(–2)	0.0	1.3(–2)					$5.68_{(m0)}$
M	0.133	4.9(–2)	3.0(–2)	9.3(–3)	3.5(–3)	1.9(–3)	1.1(–3)	8.0(–4)	1.3(–3)					$6.64_{(m0)}$
M^a	0.907	0.514	1.3(–2)	0.297	4.5(–2)	4.0(–2)	2.9(–2)	2.1(–2)	6.8(–2)	151.41	2.9(+4)	12.3	SW, P	$16.45_{(m1)}$
M^W	0.462	0.197	0.135	0.0	0.0	0.0	5.1(–2)	0.0	1.1(–2)					$4.10_{(m0)}$

Notes. The data for the energy densities is quoted near the surface ($r = 0.98\ R$) in units of 10^5 J m^{-3}. Here $E_{\rm mag}^{\rm surf}$ is the total energy density, $E_{\rm mag,tot}^{\rm dec} = \langle (\boldsymbol{B}_{\rm tot}^{\rm dec})^2 \rangle_{\theta\phi t}/2\mu_0$ is the magnetic energy density obtained from the decomposition over the first 10 harmonics, while $E_{\rm m}^{\rm dec}$ denote the magnetic energy densities for the corresponding azimuthal wavenumbers with $m = 0, ..., 5$, and $E_{\rm l,m>5}^{\rm dec}$ the magnetic energy density in scales that are considered to be small scale ($m > 5$). The rotation period $P_{\rm ADW}$ of the ADW is computed as the latitudinal and temporal average of the derivative of the maximum phase of the dynamo mode ($P_{\rm ADW} = 2\pi / < {\rm d}x_{\rm max,m1}/{\rm d}t >_{t,\theta}$). The column $P_{\rm ADW}[P_0]$ indicates the average period of the ADW compared to the bulk rotation ($P_0 = 2\pi/\Omega_0$). The column $P_{\rm ADW}[P_{\rm DR}]$ indicates the average period of the ADW compared to the period of the differential rotation. The value D indicates if the ADW is moving in the retrograde (R) or prograde (P) direction. SW indicates a standing wave. Furthermore, $\tau_{\rm cyc}$ is the characteristic timescale of the change of the dynamo solution. That coincides with the time evolution of the dominating dynamo mode, indicated in the parenthesis. If the solution exhibits oscillatory behavior, the run label is underlined. The numbers in parentheses indicate the exponent of 10.

dominant low-latitude axisymmetric fields, which show apparently random polarity reversals. The results of these studies are most closely related to our slowly rotating Runs A1, A2, and B, which also produce predominantly axisymmetric large-scale fields, although with antisolar differential rotation. This seems to suggest that axisymmetric fields are preferred at slow rotation irrespective of the differential rotation profile.

From Table 4 we notice that $m = 1$ is the first large-scale nonaxisymmetric mode excited as the rotation increases. Some higher m modes get excited, too, but they remain, on average, subdominant compared to the $m = 1$ mode. Therefore, the runs are well described by the $m = 0$ and $m = 1$ modes, shown in Fig. 10b. The axisymmetric energy is dominant at slow rotation, Co ≤ 3, while in the range $3 \leq$ Co ≤ 72 the first nonaxisymmetric mode is dominant, but its strength decreases for the low-resolution runs for Co > 20, and eventually there is a return to an axisymmetric configuration at the highest values of Co. For the high-resolution runs, however, the $m = 1$ mode energy keeps increasing until the highest rotation rates investigated.

3.6. Magnetic cycles

The time evolution of the magnetic field is not cyclic in the sense that there are not necessarily polarity reversals in all the runs. Yet, we see cyclic variations around the mean magnetic energy level, albeit with a poorly defined cycle length. This would match with an observer's viewpoint, as most often only light curve variability is observable while the surface magnetic evolution is hidden. Therefore, it makes sense to try to determine the timescale of this variability for all the runs – not only those for which we can identify cyclic polarity reversals from the butterfly diagram (the runs underlined in Table 4). By counting how many times the mean magnetic energy level is crossed, sometimes referred to as the syntactic method (Chen 1988, Chap. 9.4), we can assign a characteristic time scale of change, $\tau_{\rm cyc}$. For some of the runs, the time-latitude variability would provide another, more straightforward, way to determine the cycle length. For consistency, this approach is used to determine the cycle periods for all the runs. A comparison with cycle determination using all magnetic field components at all latitudes shows good agreement between these two methods for these kinds of simulations (Warnecke 2018). The last column in Table 4 shows $\tau_{\rm cyc}$. We use the syntactic method on the dominant modes ($m = 0$ and $m = 1$) and indicate those by a subscript. The syntactic method, however, has a limitation in that counting the fluctuations around a mean value means that we always count at least one oscillation. This makes the $\tau_{\rm cyc}$ values for Runs D, K2, and M^a questionable, as they are roughly half of the run time of the simulations. This

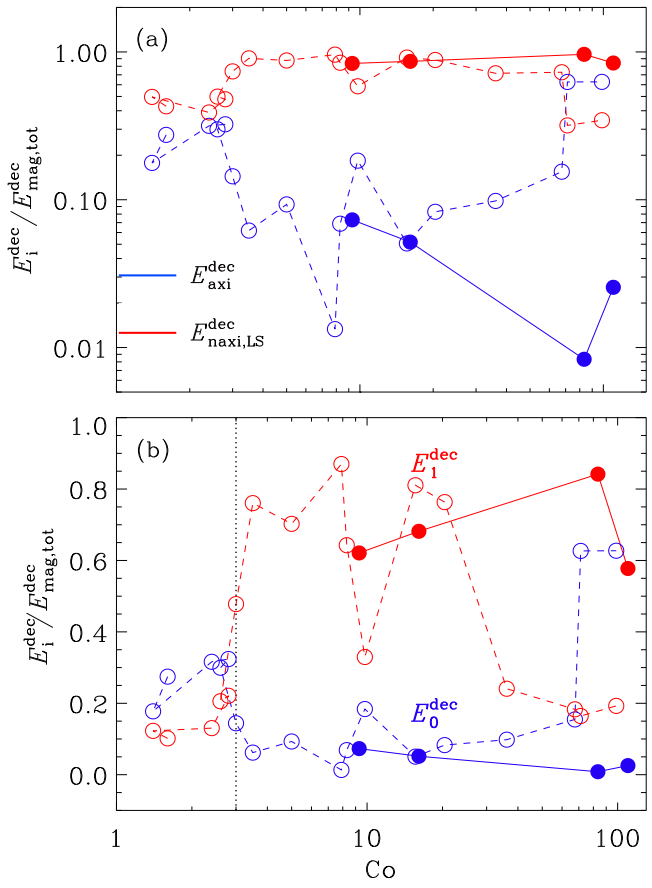

Fig. 10. Axisymmetric mean (m = 0, blue) energy vs. nonaxisymmetric large-scale (m = 1, 5; red) energy fraction at the surface (*panel a*). Axisymmetric mean (m = 0; blue) energy fraction vs. the first nonaxisymmetric mode (m = 1; red) energy fraction (*panel b*). The dotted black line denotes the axisymmetric to nonaxisymmetric transition at region Co ≈ 3. In both plots, the dashed red and blue lines connect 2π runs; filled symbols, connected with solid lines, denote the high-resolution runs.

time is denoted by Δt and is listed in Table 1. One could instead determine the characteristic time by running the aforementioned runs for a longer time. Retrieving cycle periods of the same order as the data set lengths, however, is not uncommon in observational studies (see e.g., Baliunas et al. 1995), so we have decided to retain these values with the other, more trustworthy values, in our analysis.

In the Runs A1, A2, and B, all with antisolar differential rotation profiles, we do not see much time dependence in the time–latitude (butterfly) diagrams of the mean toroidal magnetic fields; see the upper left panel of Fig. 11 for an example from Run A2. Starting from Runs C1, C2, and C3 onward to higher rotation rates (other panels of Fig. 11), however, more systematic patterns are discerned in the time series and butterfly diagrams. Runs C1 and C2 present two interesting cases, as it is very rare to obtain cyclic dynamo solutions in the regime of antisolar rotation profiles (e.g., Karak et al. 2015; Warnecke 2018), which these runs clearly possess. Furthermore, it is clear that simulations with a 2π azimuthal extent are capable of producing oscillating dynamo solutions at lower rotation rates than the corresponding $\pi/2$ wedges (see comparison in Warnecke 2018). In the rapid rotation regime, the time variability is always linked to the nonaxisymmetric component, especially in the high-resolution runs.

After estimating the characteristic time, we can determine the activity cycle period as $P_{cyc} = \tau_{cyc}$, see how it varies with rotation, and compare these values with observational results (Saar & Brandenburg 1999; Lehtinen et al. 2016). We show the results in Fig. 12a, in which we plot the ratio of rotation to activity period against the Coriolis number. We see that the transition line Co = 3 divides the runs into two populations: one in which the antisolar axisymmetric runs cluster and another in which the solar-like nonaxisymmetric runs cluster. The former population is located in the upper left corner of the plot showing a negative slope. At this location, Noyes et al. (1984) found, however, a population of stars with a positive slope. Brandenburg et al. (1998) denoted this the inactive (I) branch – to distinguish it from another active (A) one. At even higher rotation rate, Saar & Brandenburg (1999) found yet another superactive (S) branch. This branch has a negative slope, which coincides with our solar-like nonaxisymmetric population (shown in red in Fig. 12a). The rapidly rotating runs yield $\mathrm{Co}^{-0.50}$, which agrees with the slope $\mathrm{Co}^{-0.43}$ determined by Saar & Brandenburg (1999) for the S branch. However, we cannot clearly identify an A branch nor a transition between the A and S branches, which are clearly present in Saar & Brandenburg (1999). The dashed vertical line denotes the observational transition of stars without active longitudes to those with active longitudes in a sample of solar-like rapid rotators (Lehtinen et al. 2016). We note that in our simulations, active longitudes occur for considerably lower Coriolis numbers (Co > 3, corresponding to the leftmost dotted line).

The best available measure of the magnetic activity from our simulations is the ratio of magnetic to kinetic energy, which can be directly thought of as a measure of the efficiency of the dynamo; see Fig. 8. Figure 12b shows the rotation–activity period ratio as a function of this quantity. In this plot, our runs again cluster near the I branch and a well separated A–S branch. In contrast to Fig. 12a, the correlation on the I branch now appears positive, but there are not enough points to reliably conclude whether either of the correlations seen on this branch are significant. The S branch still remains inseparable, but the population of runs falling onto this branch shows a distinct negative slope.

In Fig. 12c we show a comparison between observational results and the models of Strugarek et al. (2017) using again the Coriolis number on the x axis. In this representation, although the I branch still clearly exists, none of the modeled points coincide with the observed I branch. Instead, the slowly rotating models cluster at lower Coriolis numbers than the observed stars on the inactive branch, although their cycle ratios would rather well match with those of the observed population. The Sun is not reproduced in any of those runs.

The moderate and rapid rotation runs are consistent with the S branch behavior. Strugarek et al. (2017) and the $\pi/2$ wedges of this study have a slope most closely matching the observed points of Lehtinen et al. (2016). The runs covering the full longitudinal extent have significantly shallower slope than the data points for the observed stars. The fact that the Strugarek et al. (2017) results coincide so well with those from our $\pi/2$ wedges, where the large-scale nonaxisymmetric modes are absent, suggests that also the former models tend to become axisymmetric. It needs to be seen to what extent this can be explained by those runs not being sufficiently supercritical; see again Appendix A of Käpylä et al. (2017) for a comparison of different setups. This is clearly seen in our low-resolution models, in which the magnetic field becomes axisymmetric at rapid rotation, while in their high-resolution counterparts the magnetic field remains nonaxisymmetric. We note that our first run with solar-like differential

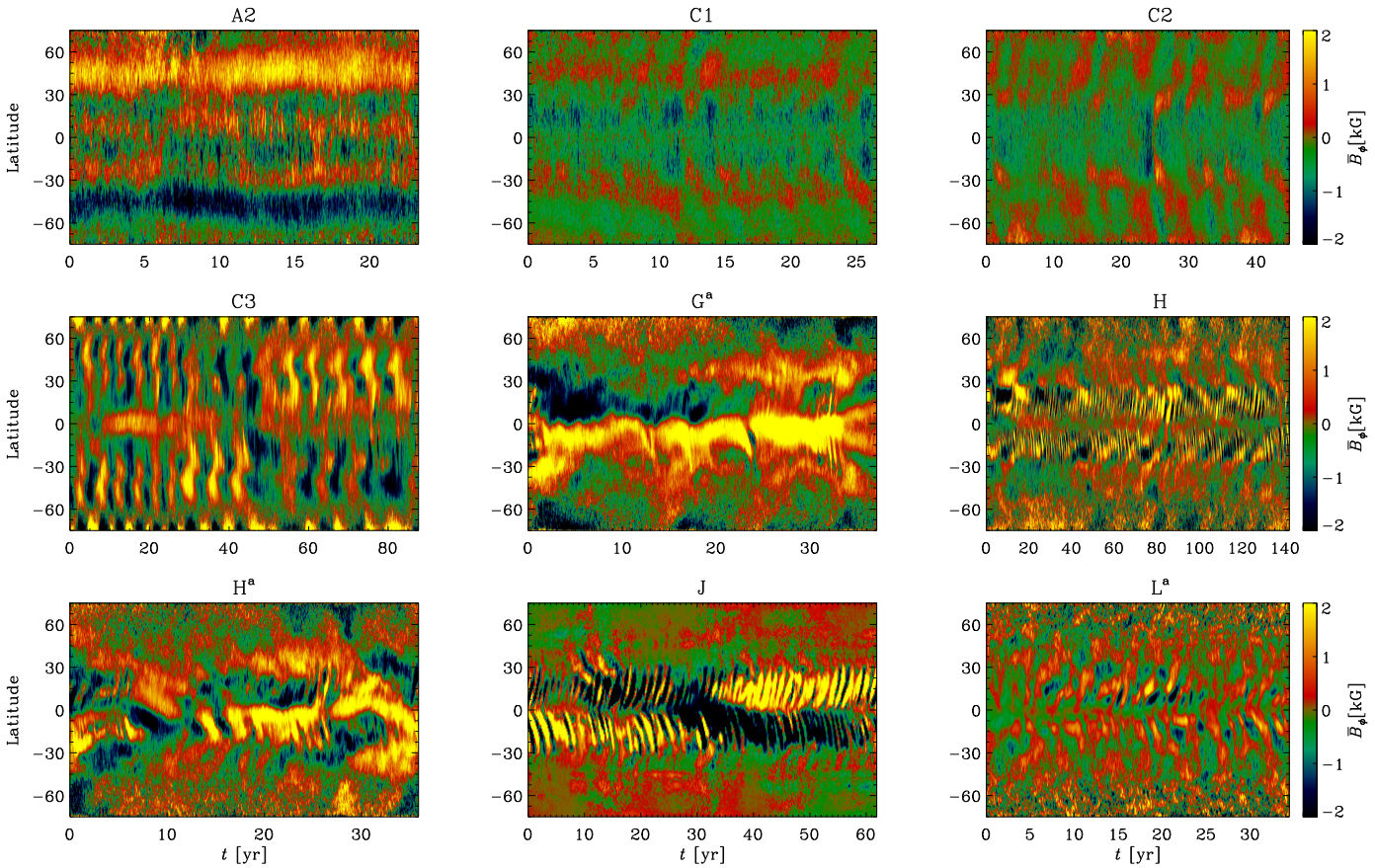

Fig. 11. Mean toroidal magnetic field $\overline{B}_\phi$ for nine representative runs near the surface $r = 0.98\,R$.

rotation, C3, is also the first showing nonaxisymmetric magnetic field. This is in disagreement with observations, as the Sun has a mostly axisymmetric field. Therefore, we conclude that the model of Strugarek et al. (2017) with lower convective velocities, and thereby less supercritical convection, can better reproduce the behavior in the proximity of the solar rotation rate. At rapid rotation regime, however, their convective velocities are too low for the models to capture the transition at all, while ours are too large and push it to Coriolis numbers that are too low.

3.7. Azimuthal dynamo waves

In stars that rotate more rapidly than the Sun, spots tend to emerge at high latitudes and are unevenly distributed in longitude. These preferred locations for starspot appearance are called active longitudes (Jetsu 1996; Berdyugina & Tuominen 1998). A phenomenon that has recently been related to active longitudes from models (Cole et al. 2014) and also observations (see e.g., Lindborg et al. 2013) is what is now called azimuthal dynamo wave (ADW). This term refers to active longitude systems that migrate in the orbital reference frame of the star. A useful comparison is the latitudinal dynamo wave visible in the Sun. This dynamo wave shows a dependence in latitude, which is visible as the appearance of sunspots at lower latitudes as the solar cycle progresses, but the spots do not appear with a preferential location in longitude. Instead of its latitude depending on time, in the ADW the longitude of the nonaxisymmetric spot-generating mechanism changes periodically in time, thereby migrating in the rotational frame of reference. Such migration was already predicted from early linear dynamo models (e.g., Krause & Rädler 1980) and the special case of nonmigratory nonaxisymmetric structure could also be interpreted as a standing ADW. The crucial difference between latitudinal and ADWs is that the polarity reversal is always associated with the former, while not necessarily with the latter. The migration direction has been observed to be preferentially prograde (see e.g., Berdyugina & Tuominen 1998; Lindborg et al. 2013; Lehtinen et al. 2016), but also a standing wave for σ Gem and a retrograde wave for EI Eri have been reported (Berdyugina & Tuominen 1998).

We inspect all our runs with a significant $m = 1$ mode for the existence of ADW. The results for the reconstruction of the first nonaxisymmetric mode of the radial magnetic field as functions of time and longitude for Runs C3, G^a, H^a, and L^a are shown in Fig. 13 for 60° northern latitude. In all the runs presented here, the $m = 1$ mode is rigidly rotating and has a different pattern speed than the gas. To verify that the magnetic field is detached from the flow, we overplot the expected advection due to differential rotation with black–white lines at the same latitude. If the magnetic field was advected by the mean flow, its maxima and minima would fall on this line. In the range $3 \le \mathrm{Co} \le 68$, the magnetic field follows a pattern that is different from the differential rotation at the surface of the star at all latitudes.

The parameters related to the ADW are listed in columns 11–14 of Table 4. The period of the ADW, $P_{\rm ADW}$, is calculated using the first derivative with respect to time of the maximum of the phase of the $m = 1$ mode, averaged over time and latitude. We compare it with the bulk rotation, $P_{\rm ADW}/P_0$, and the differential rotation, $P_{\rm ADW}/P_{\rm DR}$, where $P_0 = 2\pi/\Omega_0$ and $P_{\rm DR} = 2\pi/\langle[\Omega - \Omega_0](r = 0.98\,R)\rangle_\theta$, respectively, and indicate

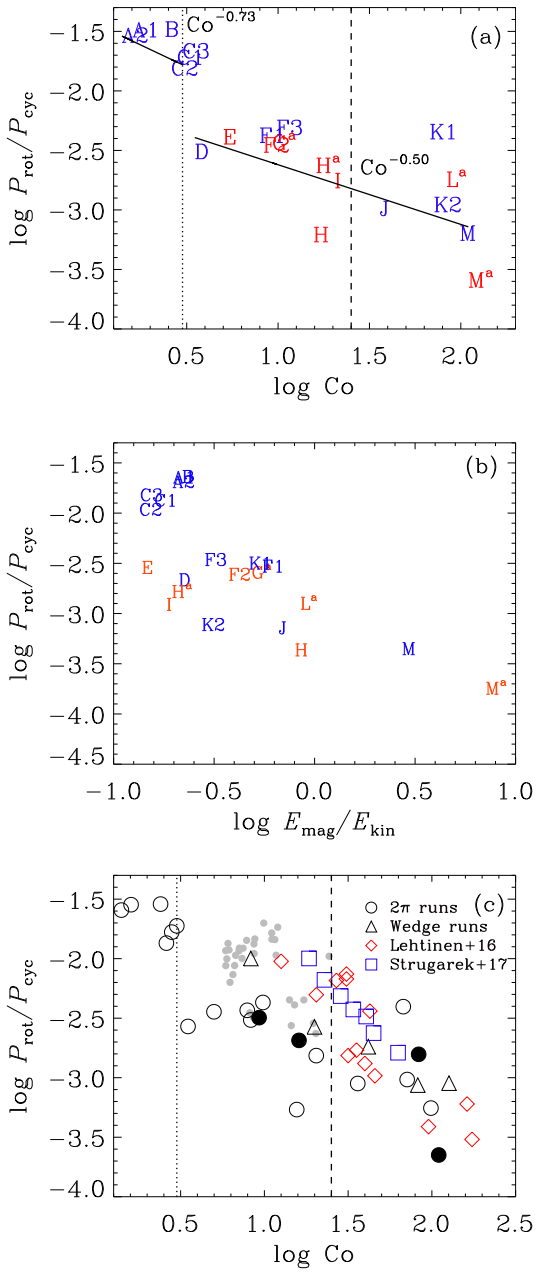

Fig. 12. Ratio of the rotation period to the cycle period as a function of Coriolis number (*panel a*). The two black lines indicate the fit to the axisymmetric and rapid rotation runs, respectively. The vertical lines denote the nonaxisymmetric transition found in our simulations (dotted; Co ≥ 3) and from the observational study of Lehtinen et al. (2016) (dashed), respectively. Runs are plotted after their labels. The color indicates the mode chosen for calculating τ_{cyc}: blue for $m = 0$, red for $m = 1$. P_{rot}/P_{cyc} as function of activity, represented by E_{mag}/E_{kin} is shown in *panel b*. *Panel c*: comparison between the results presented in this paper, Lehtinen et al. (2016), and Strugarek et al. (2017). Black circles and triangles denote high resolution and $\pi/2$ wedges in our set, respectively. The gray dots indicate M dwarfs and F and G stars from Brandenburg et al. (2017).

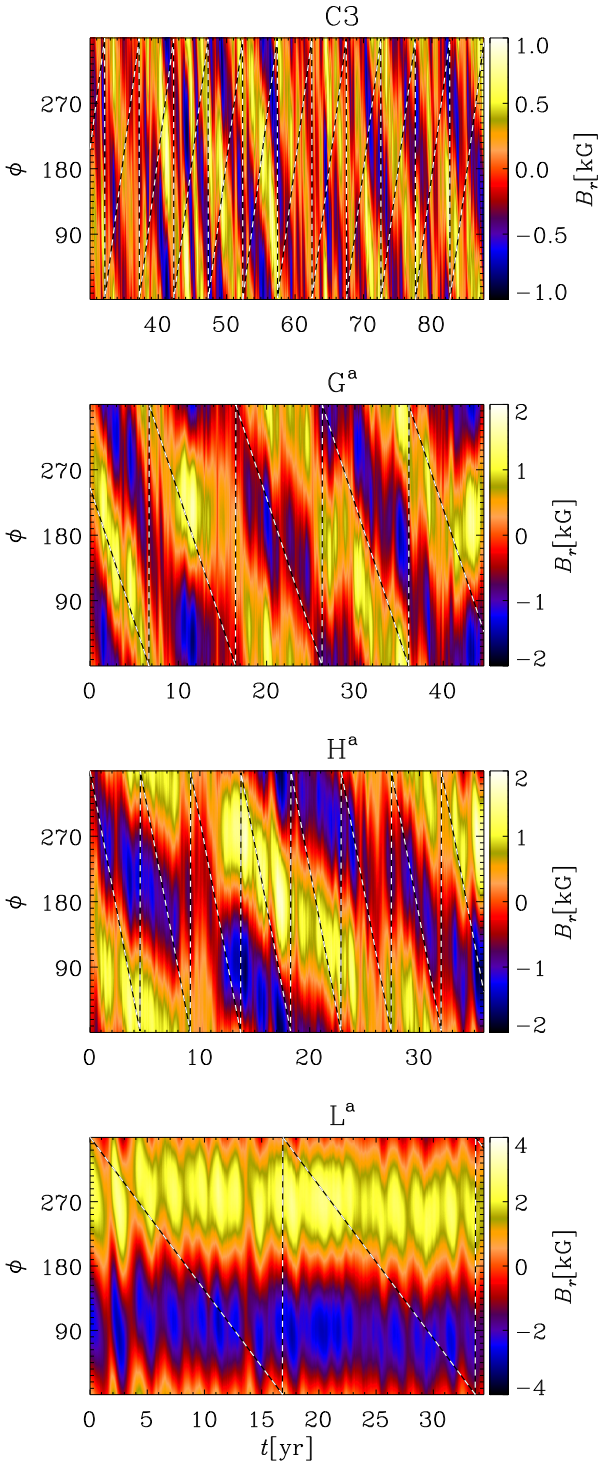

Fig. 13. Reconstruction of the $m = 1$ mode of the magnetic field at the surface of the star for Runs C3, G^a, H^a, and L^a at $\theta = +60°$. The black and white line indicates the path due to differential rotation alone.

the direction of the wave, retrograde (R, westward) or prograde (P, eastward), in the column marked *D*. A retrograde wave is moving in the opposite direction with respect to the bulk rotation. Therefore, its period is longer than the rotation period. On the other hand, a wave moving in the prograde direction has a shorter period. In most of our cases, we find retrograde ADWs, but there are some cases (Runs J, K1, L^a, M^a) in which the behavior is different. Runs J and K1 are characterized by rapid rotation and a low value of magnetic energy and the ADW has a smaller amplitude than in the other cases. In Runs M^a, L^a, and J the dynamo wave is drifting very slowly[2]. During the saturated

[2] A video of the surface radial magnetic field evolution of Run L^a can be found from https://www.youtube.com/watch?v=2g4r1uanrj4.

stage, these represent standing waves rather than migratory phenomena (therefore the identifier SW in Table 4). Their almost insignificant migrations occur in opposite directions with Runs J and M^a showing prograde migration and Run L^a exhibiting retrograde migration. In the parameter range included in this study, the retrograde migration is clearly the dominant regime. The magnetic cycle does not seem to be related in any way to the migration period of the ADW.

3.8. Time variation and flip-flop phenomenon

In some cases we find an equatorward migrating oscillatory magnetic field in the initial stages of the simulation (e.g., Runs G and H), see Fig. 11. Later, however, the dominant dynamo mode changes to a nonaxisymmetric mode soon after the large-scale field reaches dynamically significant strengths. This behavior has been found in Käpylä et al. (2013), where the $\pi/2$ and 2π versions of Run F1 have been compared. Thus, we conclude that a reduced ϕ extent significantly changes the behavior of the dynamo by suppressing the large-scale nonaxisymmetric modes ($m = 1, 2, 3$). Also, we observe that for cyclic solutions to emerge in $\pi/2$ wedges, we require a generally higher Coriolis number than in runs with full azimuthal extents.

Time variations are also seen in the cases of nearly purely nonaxisymmetric solutions; one such example is the high-resolution Run L^a. The magnetic field in this run forms two active longitudes that remain fixed on the stellar surface, having opposite polarities in each hemisphere, but exhibiting a quadrupolar symmetry with respect to the equator. The weak axisymmetric component also exhibits time variability, as can be seen from the butterfly diagram plotted in Fig. 11. Both the axi- and nonaxisymmetric components develop time variability over a similar timescale of roughly three years. The strength of the active longitudes is modulated on this timescale in such a way that those in the same hemisphere grow simultaneously (see Figs. 13 and 14) while those on the opposite hemisphere decay, followed by a reversed behavior (see Fig. 14). However, there are no clear polarity reversals that could be related to this time variation. In other words, we observe that maximum and minimum on the same hemisphere never switch in intensity, as happens in the flip-flop phenomenon (Berdyugina & Tuominen 1998; Hackman et al. 2013). It has been postulated that a polarity reversal of the active longitudes would happen during a flip-flop event and would be observable through ZDI (e.g., Carroll et al. 2009; Kochukhov et al. 2013), but the effect of ADWs has never been considered, making these conclusions uncertain.

To see whether flip-flops can occur in systems in which there is a competition between the $m = 0$ and $m = 1$ modes, we now analyze Run G^a in detail. As discussed in Sect. 3.7, this run exhibits an ADW that is migrating in the retrograde direction. To better see the time evolution of the active longitudes, this migration has to be removed, as carried out in Fig. 15, lower panel. After this systematic motion is removed, however, as in the case of L^a, the active longitudes are not switching in intensity between maxima and minima, but grow and decay together on the same hemisphere, while out of phase in the opposite hemisphere. In Run J, producing only a very weak dynamo solution with almost a standing ADW, a polarity change can, however, be detected, as is depicted in Fig. 15, upper panel. The active longitudes are seen to stay nearly fixed in the orbital frame of reference, and after quasi-regular time points, the polarity of both reverses quite abruptly. In this case the magnetic field is clearly subdominant with respect to the velocity field, but nevertheless the advection by the differential rotation explains the time

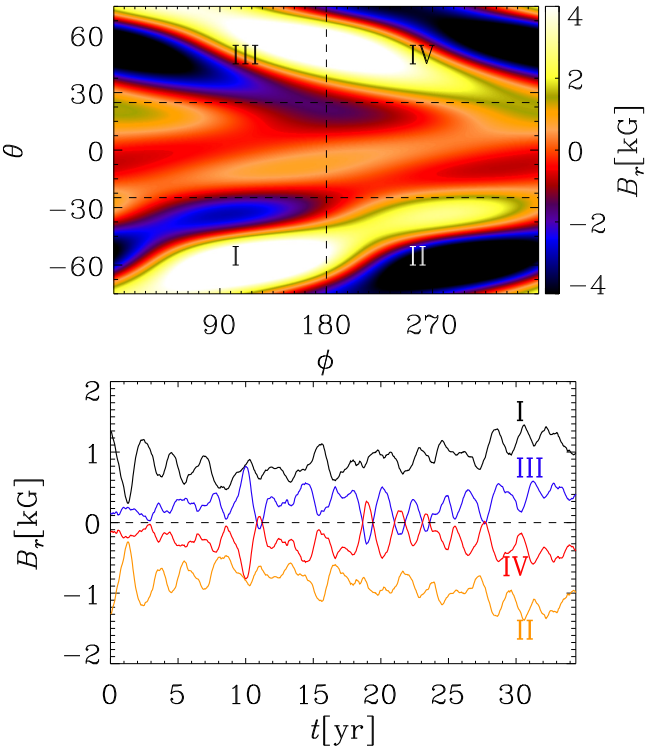

Fig. 14. Standing dynamo wave of Run L^a. *Lower panel*: time variation of the four regions indicated in the *upper panel*.

evolution of the active longitudes very poorly. Distinguishing between such a polarity reversal and the mere migration of the active longitude poses a challenge to the observations. According to our models, the migration speeds are always very distinct from the rotation periods, so any behavior caused by such systematic movement would appear smooth to a real flip-flop.

4. Conclusions

In this paper, we have performed an extensive study of the effect of rotation rate on convection-driven spherical dynamos, covering a range from 1 to 31 times the solar value, $\Omega_\odot$, corresponding to Co = 1.6 to 127. The dependence of stellar dynamos on rotation speed has been assessed over a range that is much wider than what has been studied previously. For example, Strugarek et al. (2017) studied the change of cycle frequency while changing the rotation rate by a factor of two, resulting in a change in Co of about a factor of three. We found that, for $\Omega \gtrsim 1.8\Omega_\odot$ (Co $\gtrsim$ 3), nonaxisymmetric modes are excited and ADWs are present; see Table 5. The most commonly excited configuration in our models is the $m = 1$ mode accompanied with an $m = 0$ mode comparable (for moderate rotation) or subdominant (for rapid rotation) in strength. The magnetic field near the surface is symmetric (quadrupolar) with respect to the equator in all cases with an antisolar differential rotation profile. The axisymmetric part of the magnetic field is more toroidal at moderate rotation, while preferentially more poloidal configurations are indicated from the highest rotation rates studied. In the slow rotation regime with antisolar differential rotation, the solutions are preferentially axisymmetric and poloidal.

The same pattern over the azimuthal direction can be seen observationally in the distribution of active longitudes or the magnetic field geometries of stars with different rotation rates. Lehtinen et al. (2016) found from time series photometry of

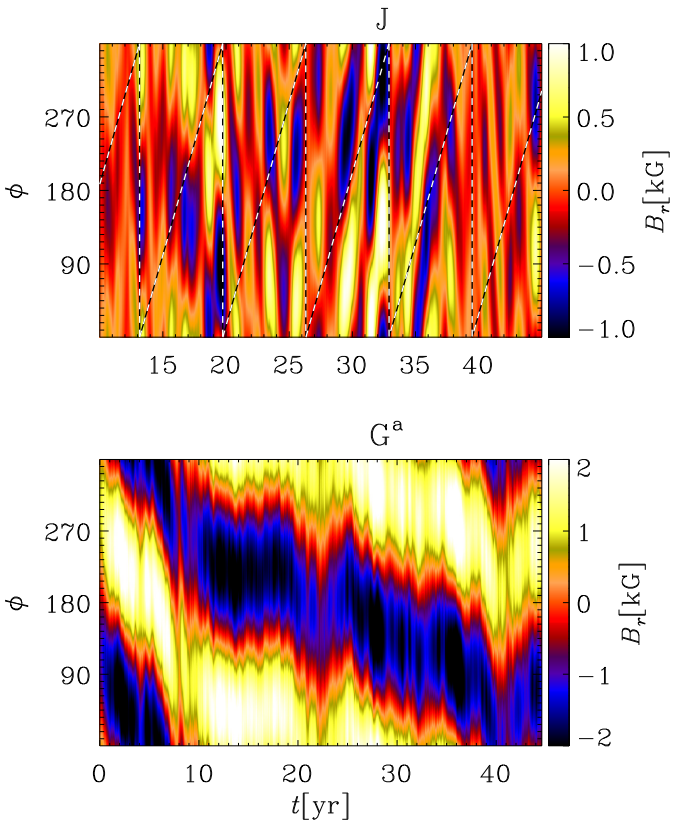

Fig. 15. *Upper panel*: flip-flop for Run J. The dashed line is the differential rotation at $\theta = +45°$. *Lower panel*: same as Fig. 13, but at $\theta = +45°$, for Run G^a. The ADW has been de-migrated to better show the active longitudes.

Table 5. Summary of the transitions from antisolar-like to solar-like differential rotation and between predominantly axisymmetric and non-axisymmetric large-scale fields from observations and our simulations as a function of increasing Coriolis number.

Transition	Observations		Simulations	
	$\tilde{\Omega}$	Co	$\tilde{\Omega}$	Co
Antisolar/solar-like DR	≈1	≈6	1.8	3
Axi/nonaxisymmetric	3–5	13–25	1.8	3
Return to axisymmetry (low-res, high Co)			15–22	37–83

Notes. Observations refer to Lehtinen et al. (2016) for the nonaxisymmetric to axisymmetric transition and to Brandenburg & Giampapa (2018) for the antisolar-like to solar-like transition using the semi-empirical τ_c values from Noyes et al. (1984).

active solar-type stars that there is an onset of active longitudes at around Co ≈ 25, corresponding to $\tilde{\Omega} \approx 4-5$. Similarly, surface magnetic field mapping using ZDI has shown that solar-type stars have a transition between axisymmetric poloidal and nonaxisymmetric toroidal field geometries at around Co ≈ 13 (or Ro = $P_{\rm rot}/\tau_c \approx 1$; Donati & Landstreet 2009; See et al. 2016), where τ_c is the convective turnover time. This split is not absolute and the rapidly rotating stars can still alternate between toroidal and poloidal fields (Kochukhov et al. 2013). Moreover, Rosén et al. (2016) observed that for rapid rotators the degree of nonaxisymmetry tends to increase toward more poloidal field geometries. This may indicate a similar behavior as in the high-resolution models, which develop nonaxisymmetric poloidal fields at the highest rotation rates. We note here that we calculate the toroidal and poloidal fields from the axisymmetric mean field in the whole convection zone, while in observations the total surface field is used.

The differences in the rotation rates and Coriolis numbers of the axisymmetric to nonaxisymmetric transition between observations and simulations may be due to several factors. First, the criteria for detecting nonaxisymmetric structures may not be fully comparable between the various studies. Second, the observational studies use semiempirical values of the convective turnover time τ_c while in this study we used the definition $\tau_c = 2\pi u_{\rm rms}/0.3\ R$. Lastly, it is worth noting that the simulations do not occupy the same parameter space as real stars. Furthermore, a different value of Co could just be explained by a different depth in the star where the dynamo is mainly driven, as $u_{\rm rms}$ has a strong radial dependency. The observations do not show any indication that the most rapidly rotating stars would again have axisymmetric fields, as is the case with the low-resolution runs in this study. The difference in behavior between high- and low-resolution runs, for which low-resolution runs turn back to axisymmetric fields and high-resolution runs remain nonaxisymmetric may simply be a symptom of the inability of the low-resolution runs to capture sufficiently small scales.

In our set of runs, we found mostly retrograde ADWs in contrast with observations of solar-like stars that show a preference for prograde direction (Lehtinen et al. 2016). The prograde pattern speeds may be analogous to those seen in the Sun. Its supergranulation pattern is found to rotate a few percent faster than the gas at the surface (Gizon et al. 2003). Similarly, magnetic tracers including sunspots are seen to rotate faster than the gas (Pulkkinen & Tuominen 1998). The occurrence of prograde pattern speeds is theoretically associated with the near-surface shear layer of the Sun (Green & Kosovichev 2006; Busse 2007; Brandenburg 2007). Thus, a reason for this discrepancy could be the fact that we simulate only the stellar convection zone and do not include the near-surface shear layer, which should lead to a prograde directed wave.

In the interval 1–1.8 $\Omega_\odot$, corresponding to Co = 1.6–2.8, we find antisolar differential rotation, which is in agreement with previous studies such as Käpylä et al. (2014) and Gastine et al. (2014). We do not see any oscillatory behavior of the magnetic field in the interval Co = 1.6–2.4, whereas close to the transition from antisolar to solar rotation profiles, at Co = 2.6–2.8, even systems with antisolar rotation profiles produce clear cycles in their axisymmetric fields. This seems to be quite a robust finding, as this behavior persists even when the efficiency of convection is varied. Cyclic magnetic activity has been seen in giants and subgiants that are believed to have antisolar differential rotation profiles (Weber et al. 2005; Kővári et al. 2007; Harutyunyan et al. 2016), which, according to our results, would be possible in a narrow region near the break point from antisolar (and axisymmetric) to solar (and nonaxisymmetric) behavior (see Table 5). In dwarfs, antisolar differential rotation is indicated only indirectly through the occurrence of enhanced activity at slow rotation for $\tilde{\Omega} \lesssim 1$ (Brandenburg & Giampapa 2018).

In the rapid rotation regime, both dominantly axisymmetric and nonaxisymmetric solutions produce time variability of very different nature, which, however, occurs over similar timescales and produces similar magnitudes of variations, at least in terms of the surface magnetic field strength. In the axisymmetric case, these relate to the latitudinal dynamo wave and are accompanied by a polarity change. In the majority of the nonaxisymmetric cases, the time variability relates to the changing activity levels

of active longitudes on different hemispheres with no associated polarity change. In one low-resolution case that produces only a very weak dynamo, we found a solution that also shows flip-flop type polarity reversals, but this particular parameter regime needs to be studied with high-resolution runs. The drift period of the active longitude system in the orbital frame of reference identified in almost every simulation seem to be decoupled from the magnetic activity cycle, but together with the variations in the active longitude strengths can be thought to give rise to an ADW. Also observationally the occurrence of cycles is not related to the axisymmetry of the stellar magnetic fields. Activity cycles are observed on slow and fast rotating stars alike, regardless of whether they have active longitudes or not (Lehtinen et al. 2016).

Our extensive study of the dependence on rotation rates allowed us to investigate the existence of activity branches (see e.g., Saar & Brandenburg 1999; Distefano et al. 2017; Reinhold et al. 2017). In our $P_{\rm rot}/P_{\rm cyc}$ versus Co plot, the runs are separated into two populations: one for the axisymmetric runs at low Coriolis numbers, whose slope of $\mathrm{Co}^{-0.73}$ seems to be similar to that found in the $\pi/2$ wedges of Warnecke (2018), the other at higher Co representing the nonaxisymmetric population, whose slope of $\mathrm{Co}^{-0.50}$ is close to the superactive branch reported in Saar & Brandenburg (1999) and whose behavior resembles that of the transitional branch of Distefano et al. (2017). However, when comparing to observations, our inactive population does not match the inactive branch seen in observational studies (e.g., Noyes et al. 1984; Brandenburg et al. 1998, 2017). A possible explanation for this discrepancy could reside in the different ways of calculating $\tau_{\rm c}$ in observations and simulations. Also, we do not find any clear separation between active and superactive branches. Moreover, we studied the behavior of $P_{\rm rot}/P_{\rm cyc}$ as a function of magnetic activity (represented, in our case, by the ratio $E_{\rm mag}/E_{\rm kin}$). In this case, the axisymmetric population seems to have a positive slope, as seen in observations. Anyway, our sparse sample at low rotation and the inability to reliably compute the chromospheric activity index $R'_{\rm HK}$ from the models do not allow us to draw any significant conclusion. We also compare our results with the numerical study of Strugarek et al. (2017). In contrast with our simulations, their solutions show only axisymmetric behavior. This, and the fact that in the rotation-activity plot their results lay close to our models with reduced ϕ extent, make us believe that the resolution used in this study was not enough to allow for nonaxisymmetric solutions. We consider this as a further proof of the importance of using high resolution when investigating high rotation regimes.

Our results confirm that the scale at which the power spectrum of the velocity field peaks shifts to higher values of ℓ with increasing rotation speed, indicating the presence of smaller convective cells at rapid rotation (Chandrasekhar 1961). Our results have also demonstrated that sufficiently high numerical resolution is important for allowing the $m = 1$ nonaxisymmetric structure to develop. The wedge assumption in the azimuthal direction was not found to be a a good assumption for rapidly rotating stars. First, this assumption suppresses the nonaxisymmetric modes that emerge close to the solar rotation rate. Second, there were only indications of oscillatory solutions in earlier $\pi/2$ wedges with antisolar rotation profiles (Karak et al. 2015; Warnecke 2018), while in this study we find clear oscillatory solutions with many polarity reversals in the runs with full azimuthal extents. The magnetic structures appearing preferentially at high-latitude regions with more rapid rotation also put the latitudinal wedge assumption into a question. A better modeling strategy for the future are full spherical grids in which the parameters are chosen so that the models are equally supercritical in terms of the Rayleigh number.

Acknowledgements. We thank the referee for constructive criticism. M.V. acknowledges a postgraduate fellowship from the SOLSTAR Max Planck Research Group and having been enrolled in the International Max Planck Research School for Solar System Science at the University of Göttingen (IMPRS) framework. The simulations were performed using the supercomputers hosted by GWDG, the Max Planck supercomputer at RZG in Garching, and CSC – IT Center for Science Ltd. in Espoo, Finland, who are administered by the Finnish Ministry of Education. The Special Grand Challenge allocation DYNAMO13 is acknowledged. J.W. acknowledges funding by the Max-Planck/Princeton Center for Plasma Physics and from the People Programme (Marie Curie Actions) of the European Union's Seventh Framework Programme (FP7/2007-2013) under REA grant agreement No. 623609. Financial support from the Academy of Finland grant No. 272157 to the ReSoLVE Centre of Excellence (J.W., M.J.K., P.J.K.), Finnish Cultural Foundation grant No. 00170789 (N.O.), as well as the NSF Astronomy and Astrophysics Grants Program (grant 1615100), the Research Council of Norway under the FRINATEK grant 231444, and the University of Colorado through its support of the George Ellery Hale visiting faculty appointment are acknowledged (A.B.).

References

Augustson, K., Brun, A. S., Miesch, M., & Toomre, J. 2015, ApJ, 809, 149
Baliunas, S. L., Donahue, R. A., Soon, W. H., et al. 1995, ApJ, 438, 269
Beaudoin, P., Simard, C., Cossette, J.-F., & Charbonneau, P. 2016, ApJ, 826, 138
Berdyugina, S. V., & Tuominen, I. 1998, A&A, 336, L25
Berdyugina, S. V., Pelt, J., & Tuominen, I. 2002, A&A, 394, 505
Boro Saikia, S., Marvin, C. J., Jeffers, S. V., et al. 2018, A&A, 616, A108
Brandenburg, A. 2007, IAU Symp., 239, 457
Brandenburg, A., & Giampapa, M. S. 2018, ApJ, 855, L22
Brandenburg, A., Saar, S. H., & Turpin, C. R. 1998, ApJ, 498, L51
Brandenburg, A., Mathur, S., & Metcalfe, T. S. 2017, ApJ, 845, 79
Brown, B. P., Browning, M. K., Brun, A. S., Miesch, M. S., & Toomre, J. 2008, ApJ, 689, 1354
Brown, B. P., Browning, M. K., Brun, A. S., Miesch, M. S., & Toomre, J. 2010, ApJ, 711, 424
Browning, M. K. 2008, ApJ, 676, 1262
Busse, F. H. 1970, ApJ, 159, 629
Busse, F. H. 2007, Sol. Phys., 245, 27
Carroll, T. A., Kopf, M., Strassmeier, K. G., Ilyin, I., & Tuominen, I. 2009, in Cosmic Magnetic Fields: From Planets, to Stars and Galaxies, eds. K. G. Strassmeier, A. G. Kosovichev, & J. E. Beckman, IAU Symp., 259, 437
Chandrasekhar, S. 1961, in Hydrodynamic and hydromagnetic stability (Oxford: Oxford University Press)
Charbonneau, P. 2013, in Solar and Stellar Dynamos, Saas-Fee Advanced Courses (Berlin, Heidelberg: Springer-Verlag), 39, 187
Chen, C. 1988, in Signal Processing Handbook, Electrical and Computer Engineering (Taylor & Francis)
Cole, E., Käpylä, P. J., Mantere, M. J., & Brandenburg, A. 2014, ApJ, 780, L22
Distefano, E., Lanzafame, A. C., Lanza, A. F., Messina, S., & Spada, F. 2017, A&A, 606, A58
Dobler, W., Stix, M., & Brandenburg, A. 2006, ApJ, 638, 336
Donati, J.-F., & Landstreet, J. D. 2009, ARA&A, 47, 333
Duarte, L. D. V., Wicht, J., & Gastine, T. 2018, Icarus, 299, 206
Fan, Y., & Fang, F. 2014, ApJ, 789, 35
Featherstone, N. A., & Hindman, B. W. 2016a, ApJ, 830, L15
Featherstone, N. A., & Hindman, B. W. 2016b, ApJ, 818, 32
Gastine, T., Duarte, L., & Wicht, J. 2012, A&A, 546, A19
Gastine, T., Yadav, R. K., Morin, J., Reiners, A., & Wicht, J. 2014, MNRAS, 438, L76
Ghizaru, M., Charbonneau, P., & Smolarkiewicz, P. K. 2010, ApJ, 715, L133
Gizon, L., Duvall, T. L., & Schou, J. 2003, Nature, 421, 43
Green, C. A., & Kosovichev, A. G. 2006, ApJ, 641, L77
Hackman, T., Pelt, J., Mantere, M. J., et al. 2013, A&A, 553, A40
Hackman, T., Lehtinen, J., Rosén, L., Kochukhov, O., & Käpylä, M. J. 2016, A&A, 587, A28
Hanasoge, S. M., Duvall, T. L., & Sreenivasan, K. R. 2012, Proc. Natl. Acad. Sci., 109, 11928
Harutyunyan, G., Strassmeier, K. G., Künstler, A., Carroll, T. A., & Weber, M. 2016, A&A, 592, A117

Hotta, H., Rempel, M., & Yokoyama, T. 2014, ApJ, 786, 24
Hotta, H., Rempel, M., & Yokoyama, T. 2016, Science, 351, 1427
Ishihara, N., & Kida, S. 2000, J Phys. Soc. Japan, 69, 1582
Järvinen, S. P., Korhonen, H., Berdyugina, S. V., et al. 2008, A&A, 488, 1047
Jetsu, L. 1996, A&A, 314, 153
Jetsu, L., Pelt, J., & Tuominen, I. 1993, A&A, 278, 449
Jones, C. A. 2014, Icarus, 241, 148
Käpylä, P. J., Mantere, M. J., & Brandenburg, A. 2012, ApJ, 755, L22
Käpylä, P. J., Mantere, M. J., Cole, E., Warnecke, J., & Brandenburg, A. 2013, ApJ, 778, 41
Käpylä, P. J., Käpylä, M. J., & Brandenburg, A. 2014, A&A, 570, A43
Käpylä, M. J., Käpylä, P. J., Olspert, N., et al. 2016, A&A, 589, A56
Käpylä, P. J., Käpylä, M. J., Olspert, N., Warnecke, J., & Brandenburg, A. 2017, A&A, 599, A5
Karak, B. B., Käpylä, P. J., Käpylä, M. J., et al. 2015, A&A, 576, A26
Kitchatinov, L. L., & Rüdiger, G. 1999, A&A, 344, 911
Kővári, Z., Bartus, J., Strassmeier, K. G., et al. 2007, A&A, 474, 165
Kochukhov, O., Mantere, M. J., Hackman, T., & Ilyin, I. 2013, A&A, 550, A84
Krause, F., & Rädler, K.-H. 1980, in Mean-field Magnetohydrodynamics and Dynamo Theory (Oxford: Pergamon Press)
Lehtinen, J., Jetsu, L., Hackman, T., Kajatkari, P., & Henry, G. W. 2016, A&A, 588, A38
Lindborg, M., Mantere, M. J., Olspert, N., et al. 2013, A&A, 559, A97
Morin, J., Donati, J.-F., Petit, P., et al. 2010, MNRAS, 407, 2269
Moss, D., & Brandenburg, A. 1995, Geophys. Astrophys. Fluid Dyn., 80, 229
Moss, D., Barker, D. M., Brandenburg, A., & Tuominen, I. 1995, A&A, 294, 155
Nelson, N. J., Brown, B. P., Brun, A. S., Miesch, M. S., & Toomre, J. 2013, ApJ, 762, 73
Noyes, R. W., Weiss, N. O., & Vaughan, A. H. 1984, ApJ, 287, 769
Oláh, K., Kolláth, Z., Granzer, T., et al. 2009, A&A, 501, 703
Oláh, K., Kővári, Z., Petrovay, K., et al. 2016, A&A, 590, A133
Olspert, N., Käpylä, M. J., Pelt, J., et al. 2015, A&A, 577, A120
Olspert, N., Lehtinen, J. J., Käpylä, M. J., Pelt, J., & Grigorievskiy, A. 2018, A&A, in press, DOI: 10.1051/0004-6361/201732525
Ossendrijver, M. 2003, A&A Rev., 11, 287
Parker, E. N. 1955, ApJ, 121, 491
Pelt, J., Brooke, J. M., Korpi, M. J., & Tuominen, I. 2006, A&A, 460, 875
Pipin, V. V. 2017, MNRAS, 466, 3007
Pulkkinen, P., & Tuominen, I. 1998, A&A, 332, 748
Rädler, K.-H., Wiedemann, E., Brandenburg, A., Meinel, R., & Tuominen, I. 1990, A&A, 239, 413
Reinhold, T., & Gizon, L. 2015, A&A, 583, A65
Reinhold, T., Reiners, A., & Basri, G. 2013, A&A, 560, A4
Reinhold, T., Cameron, R. H., & Gizon, L. 2017, A&A, 603, A52
Roettenbacher, R. M., Monnier, J. D., Korhonen, H., et al. 2016, Nature, 533, 217
Rosén, L., Kochukhov, O., Hackman, T., & Lehtinen, J. 2016, A&A, 593, A35
Rüdiger, G. 1978, Astron. Nachr., 299, 217
Saar, S. H., & Brandenburg, A. 1999, ApJ, 524, 295
Schrinner, M., Petitdemange, L., & Dormy, E. 2012, ApJ, 752, 121
See, V., Jardine, M., Vidotto, A. A., et al. 2016, MNRAS, 462, 4442
Stassun, K. G., Hebb, L., Covey, K., et al. 2011, in 16th Cambridge Workshop on Cool Stars, Stellar Systems, and the Sun, eds. C. Johns-Krull, M. K. Browning, & A. A. West, ASP Conf. Ser., 448, 505
Strugarek, A., Beaudoin, P., Charbonneau, P., Brun, A. S., & do Nascimento J.-D. 2017, Science, 357, 185
Warnecke, J. 2018, A&A, 616, A72
Warnecke, J., Käpylä, P. J., Käpylä, M. J., & Brandenburg, A. 2014, ApJ, 796, L12
Warnecke, J., Käpylä, P. J., Käpylä, M. J., & Brandenburg, A. 2016, A&A, 596, A115
Warnecke, J., Rheinhardt, M., Tuomisto, S., et al. 2018, A&A, 609, A51
Weber, M., Strassmeier, K. G., & Washuettl, A. 2005, Astron. Nachr., 326, 287
Yadav, R. K., Christensen, U. R., Morin, J., et al. 2015a, ApJ, 813, L31
Yadav, R. K., Gastine, T., Christensen, U. R., & Reiners, A. 2015b, A&A, 573, A68

Appendix A: Decomposition of the magnetic and velocity field in spherical harmonics

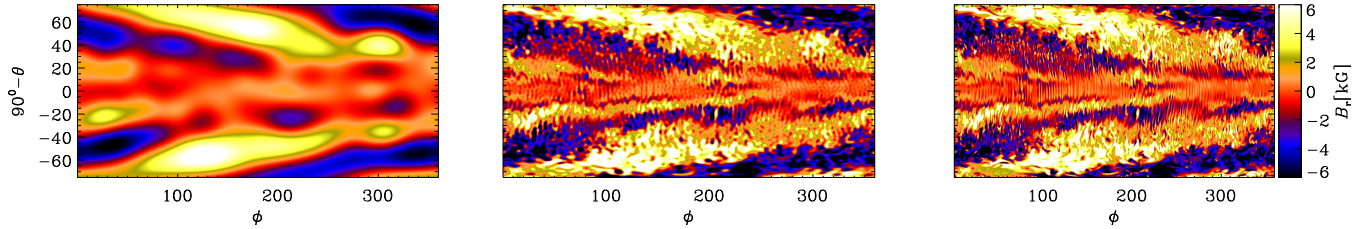

Fig. A.1. Spherical harmonic reconstruction, using $1 \le \ell \le 10$ harmonics (*left panel*) and $1 \le \ell \le 100$ harmonics (*middle panel*), and original data of the radial magnetic field (*right panel*) near the surface ($r = 0.98\ R$) of Run L^a.

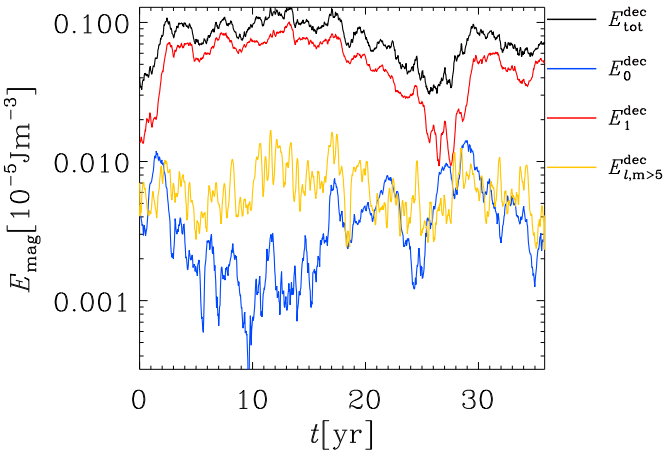

Fig. A.2. Time series of the total radial magnetic energy from decomposition (in black) and three of the m modes for Run H^a. Blue: $m = 0$; red: $m = 1$; and yellow: small-scale magnetic field.

To investigate the scale dependence of the velocity and magnetic fields, it is instructive to decompose the solutions into spherical harmonics. For this purpose, we only use the radial components of the magnetic and velocity fields, B_r and u_r, respectively. Those are related to the respective superpotentials via

$$B_r = L^2\mathcal{B}, \quad u_r = L^2\mathcal{U}, \tag{A.1}$$

where $L^2(\cdot) = -\sin^{-1}\partial_\theta(\sin\theta\partial_\theta\,\cdot) - \sin^{-2}\partial_\phi^2$ is the angular momentum operator and $\mathcal{B}$ and $\mathcal{U}$ are the poloidal superpotentials that can be expanded in terms of spherical harmonics $Y_\ell^m(\theta,\phi)$ as (Krause & Rädler 1980)

$$\mathcal{U}(\theta,\phi) = \sum_{\ell=0}^{\ell_{\max}} \sum_{m=-\ell}^{\ell} \tilde{\mathcal{U}}_\ell^m Y_\ell^m(\theta,\phi), \tag{A.2}$$

where $\tilde{\mathcal{U}}_\ell^m$ are computed as

$$\tilde{\mathcal{U}}_\ell^m = \int_0^{2\pi}\int_{\theta_0}^{\pi-\theta_0} \mathcal{U}(\theta,\phi)\, Y_\ell^{m\,*}(\theta,\phi)\, \sin\theta\, \mathrm{d}\theta\, \mathrm{d}\phi, \tag{A.3}$$

and likewise for $\tilde{\mathcal{B}}_\ell^m$. Owing to the absence of magnetic monopoles, however, there is no contribution to the magnetic field for $\ell = 0$. In practice, we work directly with the radial components of velocity and magnetic field, whose transforms are related to $\mathcal{B}$ and $\mathcal{U}$ via $\hat{B}_{\ell,r}^m = \ell(\ell+1)\hat{\mathcal{B}}_\ell^m$ and $\hat{u}_{\ell,r}^m = \ell(\ell+1)\hat{\mathcal{U}}_\ell^m$, respectively.

While testing the decomposition, we noticed that the large-scale field features were fairly well described by the first few modes ($0 \le \ell \le 5$). Therefore, in order to obtain a complete picture, we decompose the magnetic and velocity field in the first eleven spherical harmonics ($0 \le \ell \le 10$) and consider $0 \le \ell \le 5$ and $0 \le m \le 5$ as the large-scale fields and the rest as small-scale fields. Throughout this work we use the decomposition for the radial velocity and magnetic field on a slice at a fixed radial position of $r = 0.98\ R$.

We illustrate the quality of the reconstruction in Fig. A.1 showing the radial magnetic field from Run L^a using different numbers of spherical harmonics. In the left panel, the reconstruction was obtained using $1 \le \ell \le 10$, while in the central panel, the reconstruction is obtained summing over the first 100 spherical harmonics. The right panel shows the original data slice. It is clear from Fig. A.1 that $l_{\max} = 10$ allows us to capture the main features of the magnetic field and a reasonable amount of the surface total energy (see, Table 4). We show a typical time series of various m-mode energies from the surface radial magnetic field reconstruction of Run H^a in Fig. A.2. This run is dominated by the $m = 1$ mode, which shows cyclic variations over time, and also long-term changes, during which the axisymmetric modes become comparable to the dominant mode for a short period of time.

5.2 Stellar dynamos in the transition regime: multiple dynamo modes and anti-solar differential rotation

Contribution to the paper: I run the simulation, performed the data analysis and wrote the first draft of the manuscript.

The Astrophysical Journal, 886:21 (10pp), 2019 November 20 https://doi.org/10.3847/1538-4357/ab3e07

Stellar Dynamos in the Transition Regime: Multiple Dynamo Modes and Antisolar Differential Rotation

M. Viviani[1], M. J. Käpylä[1,2], J. Warnecke[1], P. J. Käpylä[2,3], and M. Rheinhardt[2]
[1] Max-Planck-Institut für Sonnensystemforschung, Justus-von-Liebig-Weg 3, D-37077 Göttingen, Germany; viviani@mps.mpg.de
[2] ReSoLVE Centre of Excellence, Department of Computer Science, Aalto University, P.O. Box 15400, FI-00076 Aalto, Finland
[3] Institut für Astrophysik, Georg-August-Universität Göttingen, Friedrich-Hund-Platz 1, D-37077 Göttingen, Germany
Received 2019 February 11; revised 2019 August 9; accepted 2019 August 17; published 2019 November 14

Abstract

Global and semi-global convective dynamo simulations of solar-like stars are known to show a transition from an antisolar (fast poles, slow equator) to solar-like (fast equator, slow poles) differential rotation (DR) for increasing rotation rate. The dynamo solutions in the latter regime can exhibit regular cyclic modes, whereas in the former one, only stationary or temporally irregular solutions have been obtained so far. In this paper we present a semi-global dynamo simulation in the transition region, exhibiting two coexisting dynamo modes, a cyclic and a stationary one, both being dynamically significant. We seek to understand how such a dynamo is driven by analyzing the large-scale flow properties (DR and meridional circulation) together with the turbulent transport coefficients obtained with the test-field method. Neither an $\alpha\Omega$ dynamo wave nor an advection-dominated dynamo are able to explain the cycle period and the propagation direction of the mean magnetic field. Furthermore, we find that the α effect is comparable or even larger than the Ω effect in generating the toroidal magnetic field, and therefore, the dynamo seems to be of $\alpha^2\Omega$ or α^2 type. We further find that the effective large-scale flows are significantly altered by turbulent pumping.

Key words: dynamo – magnetohydrodynamics (MHD)

1. Introduction

Recently, Brandenburg & Giampapa (2018) reported on an abrupt increase of the magnetic activity level of solar-like stars with decreasing values of the Coriolis number in the vicinity of its solar value, with the Coriolis number quantifying the rotational influence on convection. Another observational study (Olspert et al. 2018) found that the degree of magnetic variability abruptly decreases, indicative of the disappearance of magnetic cycles, at slightly lower than solar chromospheric activity index values. Moreover, Metcalfe et al. (2016) interpreted *Kepler* data to indicate that the Sun is rotationally and magnetically in a transitional state, where the global magnetic dynamo is shutting down. Brandenburg & Giampapa (2018) proposed a transition in the differential rotation (DR) from solar-like (for younger stars) to antisolar (at a later age) to be responsible for some of these phenomena.

This transition (henceforth AS–S transition) has already been the subject of many numerical studies (see, e.g., Gastine et al. 2014; Käpylä et al. 2014; Featherstone & Miesch 2015; Mabuchi et al. 2015; Viviani et al. 2018), and they all pinpoint it in a narrow Coriolis number interval around its solar value. The latter can be estimated, for example, from mixing-length models to be around two (e.g., Käpylä et al. 2014). However, none of these works considered dynamo solutions near the transition point. They either studied the cyclic modes in the solar-like rotation regime, or the stationary and temporally irregular ones (Karak et al. 2015; Warnecke 2018) obtained in the antisolar regime.

In a previous paper (Viviani et al. 2018), we reported on dynamo simulations of solar-like stars with varying rotation rate, two of which showed oscillatory behavior in the AS-S transition. In these simulations, the poleward migration of the magnetic field is accompanied by a rotation profile exhibiting a decelerated equator and faster polar regions (antisolar DR). The aim of the present paper is to study how such transitional–regime dynamos operate.

In the regime of solar-like DR, cyclic dynamo solutions with equatorward dynamo waves are often obtained from global magneto-convection models (e.g., Käpylä et al. 2012; Augustson et al. 2015; Strugarek et al. 2017). Most of them can be explained in terms of Parker waves (see, e.g., Warnecke et al. 2014, 2016, 2018; Käpylä et al. 2016, 2017; Warnecke 2018). The migration direction and cycle period of such waves is determined by the product of the α effect and the radial gradient of the local rotation rate Ω (Parker 1955; Yoshimura 1975). For an equatorward-migrating field in the northern hemisphere (as observed on the Sun), one needs, for example, a negative radial gradient of Ω and a positive α effect. However, simplified dynamo models often invoke an advection-dominated concept (e.g., Choudhuri et al. 1995; Dikpati & Charbonneau 1999; Küker et al. 2001) to explain the migration and cyclic behavior of large-scale stellar magnetic fields. In this case, the meridional flow speed and direction at the location of the toroidal field generation determine the cycle period and latitudinal dynamo wave direction.

Another possible mechanism generating cyclic dynamo solutions is an α^2 dynamo (Baryshnikova & Shukurov 1987; Rädler & Bräuer 1987; Brandenburg 2017). In this case, magnetic field generation is due to the α effect alone, and DR is not needed. Such a dynamo was reproduced in forced turbulence in a spherical shell (Mitra et al. 2010) and convection simulations in a box (Masada & Sano 2014), but global convective dynamo models have not yet yielded a similar solution.

In this work, we will investigate the properties of one particular transitional–regime dynamo solution, and test which mechanisms can explain the seen cyclic behavior. To achieve this goal we will use the test-field method (Schrinner et al. 2005, 2007) for extracting the turbulent transport coefficients.

This is possible due to the dominance of the axisymmetric magnetic field allowing us to try a description in terms of mean-field theory. The test-field method has been successfully used in previous studies to explain planetary dynamos (e.g., Schrinner 2011; Schrinner et al. 2011, 2012), cyclic dynamo solutions of solar-type stars (Warnecke et al. 2018; Warnecke 2018), and the long-term variations of these solutions (Gent et al. 2017).

2. Setup and Methods

We use the Pencil Code[4] to solve the fully compressible magnetohydrodynamic equations for the velocity $\boldsymbol{U}$, the density ρ, the specific entropy s, and the magnetic vector potential $\boldsymbol{A}$ with the magnetic field $\boldsymbol{B} = \boldsymbol{\nabla} \times \boldsymbol{A}$ in a spherical shell without polar cap, defined in spherical coordinates (r, θ, ϕ) by $0.7R \leqslant r \leqslant R$ for the radial extent, with $\theta_0 \leqslant \theta \leqslant \pi - \theta_0$ and $0 \leqslant \phi \leqslant 2\pi$ for the extents in colatitude and longitude, respectively, where $\theta_0 = 15°$. The setup is the same as the one used in Käpylä et al. (2013) and Viviani et al. (2018). We impose impenetrable and stress-free boundary conditions at all radial and latitudinal boundaries for the velocity field $\boldsymbol{U}$, and a perfect-conductor boundary condition at the bottom and the latitudinal boundaries for $\boldsymbol{B}$, while at the top, the field is forced to be radial. The temperature follows a blackbody condition at the top, whereas a constant heat flux is prescribed at the bottom. At the latitudinal boundaries, zero heat flux is enforced. We start with an isentropic atmosphere for density and entropy, see Käpylä et al. (2013) for details. The initial conditions for the magnetic field and the velocity are weak Gaussian seeds.

Nondimensional input parameters for the examined run are the Taylor number, or correspondingly the Ekman number, defined as

$$\mathrm{Ta} = (2\Omega_0(\Delta r)^2/\nu)^2 = \mathrm{Ek}^{-2} = 2.03 \cdot 10^7, \quad (1)$$

where Ω_0 is the overall rotation rate with $\Omega_0/\Omega_\odot = 1.8$ for the considered run, $\Delta r = 0.3R$ is the thickness of the shell, and ν is the constant viscosity. Further, we have the thermal, sub-grid scale (SGS) thermal and magnetic Prandtl numbers, the latter two describing the unresolved turbulent effects:

$$\mathrm{Pr} = \frac{\nu}{\chi^{\mathrm{m}}} = 58, \quad \mathrm{Pr_{SGS}} = \frac{\nu}{\chi^{\mathrm{m}}_{\mathrm{SGS}}} = 2.5, \quad \mathrm{Pr_M} = \frac{\nu}{\eta} = 1. \quad (2)$$

Here, χ^{m} is the heat diffusivity calculated in the middle of the convective zone at $r^{\mathrm{m}} = 0.85R$ as $\chi^{\mathrm{m}} = K(r^{\mathrm{m}})/c_P\rho(r^{\mathrm{m}})$, c_P being the specific heat at constant pressure. The radiative heat conductivity K follows an r^{-15} dependency to mimic the actual heat flux profile in the Sun. $\chi^{\mathrm{m}}_{\mathrm{SGS}}$ is the turbulent heat diffusivity at $r = r^{\mathrm{m}}$ (see Käpylä et al. 2013, for details) and η is the constant magnetic diffusivity.

The nondimensional quantities are scaled to physical units using the solar radius $R = 7 \cdot 10^8$ m, solar rotation rate $\Omega_\odot = 2.7 \cdot 10^{-6}$ s^{-1}, the density at the bottom of the solar convection zone $\rho(0.7R) = \rho_0 = 200$ kg m^{-3}, and $\mu_0 = 4\pi \cdot 10^{-7}$ Hm^{-1}. The initial density contrast in the simulation is roughly 30, and the dimensionless luminosity $\mathcal{L} = L_0/[\rho_0(GM)^{3/2}R^{1/2}] \approx 3.8 \cdot 10^{-5}$, where L_0 is the luminosity in the simulation, G is the gravitational constant, and M the mass of the star. This corresponds to an approximately 10^6 times higher luminosity than the solar one, $L_\odot$, to avoid the acoustic timestep constraint. The rotation rate is increased correspondingly in proportion to $(L_0/L_\odot)^{1/3}$, to obtain a realistic rotational influence on the flow (for further details see Appendix A of Käpylä et al. 2019).

We indicate by $\overline{\boldsymbol{B}}$ and $\overline{\boldsymbol{U}}$ the mean (longitudinally averaged) fields, and by $\boldsymbol{b}'$, $\boldsymbol{u}'$ the corresponding fluctuating fields, so that, for example, $\boldsymbol{B} = \overline{\boldsymbol{B}} + \boldsymbol{b}'$.

The need to compute turbulent transport coefficients can be seen from the induction equation for the mean magnetic field, $\overline{\boldsymbol{B}}$:

$$\frac{\partial \overline{\boldsymbol{B}}}{\partial t} = \boldsymbol{\nabla} \times (\overline{\boldsymbol{U}} \times \overline{\boldsymbol{B}} + \overline{\boldsymbol{u}' \times \boldsymbol{b}'}) - \boldsymbol{\nabla} \times \eta \boldsymbol{\nabla} \times \overline{\boldsymbol{B}}. \quad (3)$$

The term $\overline{\boldsymbol{\mathcal{E}}} = \overline{\boldsymbol{u}' \times \boldsymbol{b}'}$ is the turbulent electromotive force (EMF); it can be expanded in terms of $\overline{\boldsymbol{B}}$ and its derivatives. Further, the tensorial coefficients of the individual contributions can be divided into symmetric and antisymmetric parts (see, e.g., Krause & Rädler 1980) such that

$$\overline{\boldsymbol{\mathcal{E}}} = \boldsymbol{\alpha} \cdot \overline{\boldsymbol{B}} + \boldsymbol{\gamma} \times \overline{\boldsymbol{B}} - \boldsymbol{\beta} \cdot \boldsymbol{\nabla} \times \overline{\boldsymbol{B}} - \boldsymbol{\delta} \times \boldsymbol{\nabla} \times \overline{\boldsymbol{B}} - \boldsymbol{\kappa} \cdot (\boldsymbol{\nabla}\overline{\boldsymbol{B}})^{(s)}, \quad (4)$$

where $\boldsymbol{\alpha}$ and $\boldsymbol{\beta}$ are symmetric tensors of rank two, $\boldsymbol{\gamma}$ and $\boldsymbol{\delta}$ are vectors, while $\boldsymbol{\kappa}$ is a tensor of rank three with $(\boldsymbol{\nabla}\overline{\boldsymbol{B}})^{(s)}$ being the symmetric part of the derivative tensor of $\overline{\boldsymbol{B}}$. Each of these coefficients can be related to a physical effect, e.g., $\boldsymbol{\alpha}$ covers cyclonic generation (α effect), $\boldsymbol{\beta}$ describes turbulent diffusion, $\boldsymbol{\gamma}$ represents turbulent pumping. The pumping enters the *effective mean flow*, $\overline{\boldsymbol{U}}^{\mathrm{eff}} = \overline{\boldsymbol{U}} + \boldsymbol{\gamma}$, (e.g., Kichatinov 1991; Ossendrijver et al. 2002; Käpylä et al. 2006; Warnecke et al. 2018) and may thus be crucial in determining the nature of the dynamo.

To determine the turbulent transport coefficients, we continued one of the transitional–regime dynamo runs from Viviani et al. (2018), showing a cyclic dynamo solution (Run C1), with the test-field module of the Pencil Code activated (for its theory, see Schrinner et al. 2005, 2007).

3. Results

The run considered is characterized by the following nondimensional output parameters: the fluid and magnetic Reynolds numbers

$$\mathrm{Re} = \frac{u_{\mathrm{rms}}}{\nu k_u} = 41, \quad \mathrm{Re_M} = \frac{u_{\mathrm{rms}}}{\eta k_u} = 41, \quad (5)$$

and the Coriolis number

$$\mathrm{Co} = \frac{2\Omega_0}{u_{\mathrm{rms}} k_u} = 2.8. \quad (6)$$

Here, $k_u = 2\pi/\Delta r \approx 21/R$ is an estimate of the wavenumber of the largest eddies, and the averaged rms velocity is defined as $u_{\mathrm{rms}} = \sqrt{(3/2)\langle U_r^2 + U_\theta^2 \rangle_{r\theta\phi t}}$ (see Käpylä et al. 2013). Angle brackets indicate averaging over the coordinate(s) in the subscript.

3.1. Mean Magnetic Field

The mean magnetic field is prevailingly symmetric about the equator (quadrupolar) and shows cyclic behavior with poleward-migrating $\overline{B}_\phi$, and polarity reversals at mid to high latitudes (Figure 1(a)). Detailed inspection of the solution reveals the presence of a cyclic and a stationary constituent, the

[4] https://github.com/pencil-code/

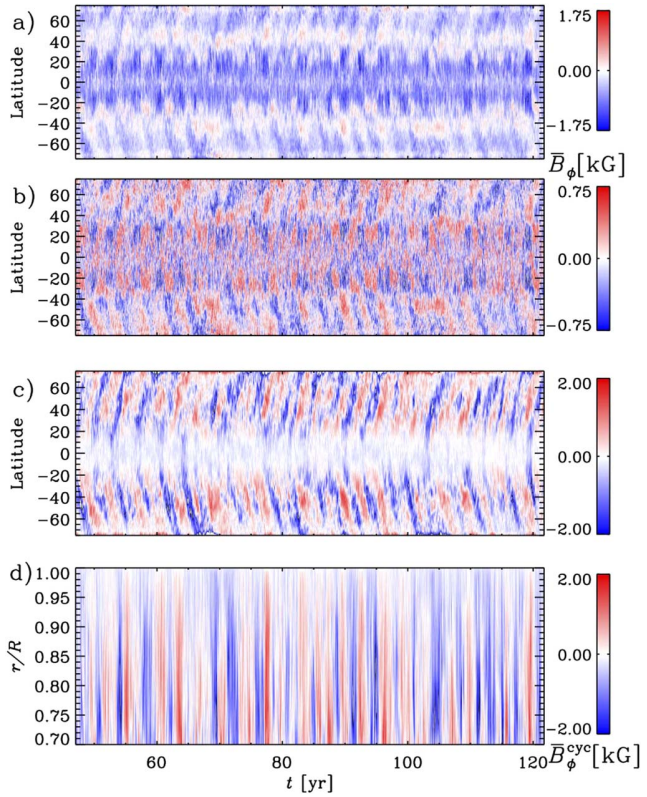

Figure 1. (a): time–latitude diagram for $\overline{B}_\phi$ near the surface ($r = 0.98\,R$). (b): analogously for $\overline{B}_\phi^{\rm cyc} = \overline{B}_\phi - \langle \overline{B}_\phi \rangle_t$. (c): same as in (b), but at $r = 0.8\,R$. (d): time–radius diagram for $\overline{B}_\phi^{\rm cyc}$ at latitude 50°.

latter being 2–2.5 times stronger (in rms values) than the former. We interpret these as two different, coexisting dynamo modes, $\langle \overline{\boldsymbol{B}} \rangle_t$ and $\overline{\boldsymbol{B}}^{\rm cyc} = \overline{\boldsymbol{B}} - \langle \overline{\boldsymbol{B}} \rangle_t$, respectively; see Figures 1(b)–(d) for the toroidal component of $\overline{\boldsymbol{B}}^{\rm cyc}$ at two depths, along with its dependence on radius and time at latitude +50° where it is strongest in rms value. Its topology is similar throughout the convection zone, and the poleward migration is present at all depths.

3.2. Mean Flows

We start our analysis by investigating meridional circulation and DR as shown in Figures 2(a)–(c). The former has a dominant, large, counterclockwise cell, producing a relatively strong (20 m s^{-1}) poleward flow near the surface at almost all latitudes. There is a slow equatorward return flow widely distributed in the bulk of the convection zone at mid to high latitudes. In the slow rotation regime, antisolar DR is often accompanied by a single cell counterclockwise meridional circulation. In contrast, in the regime of fast rotation, solar-like DR drives multicellular meridional circulation aligned with the rotation axis. The cell pattern in this run represents a transitional state between these two regimes (e.g., Käpylä et al. 2014; Featherstone & Miesch 2015; Karak et al. 2015).

The DR profile shows a decelerated equator and accelerated polar regions at the surface; hence, it is broadly speaking antisolar, despite some regions of weakly solar-like DR at the bottom of the CZ. The pole-equator difference at the surface is comparable to runs with similar rotational influence (e.g., Karak et al. 2015; Warnecke 2018). However, the energy in the DR compared to the total kinetic energy, neglecting the rigid rotation, is smaller than in runs with slightly slower and faster rotation (Viviani et al. 2018). This is most likely because our run is very close to the actual AS–S transition. In the DR profile, we find two distinct features: at midlatitudes, there is a local minimum of Ω, which has also been found in simulations with about three times faster rotation. In these, the resulting shear drives a dynamo wave obeying the Parker–Yoshimura rule (e.g., Warnecke et al. 2014). Furthermore, we find strong negative shear in a layer near the surface at low latitudes.

3.3. Turbulent Transport Coefficients

Next, we look at the turbulent transport coefficients, for which we have used a slightly different definition than in previous work (Schrinner et al. 2007; Warnecke et al. 2018), see Appendix A for motivation and details. We begin by discussing $\boldsymbol{\alpha}$ and $\boldsymbol{\gamma}$, and compare them with their counterparts from a more rapidly rotating dynamo run with solar-like DR of Warnecke et al. (2018) in terms of the ratio of their extremal values. Regarding $\boldsymbol{\alpha}$ (see Figure 3), both α_{rr} and $\alpha_{\phi\phi}$ are 20% smaller than in Warnecke et al. (2018), while the meridional profiles are similar. Furthermore, $\alpha_{\theta\theta}$ is nearly 30% larger and shows an opposite sign near the surface close to the equator. The corresponding ratios for the off-diagonal components $\alpha_{r\theta}$, $\alpha_{\theta\phi}$, and $\alpha_{r\phi}$ are 1.9, 1.1, and 0.7, respectively. Moreover, $\alpha_{r\theta}$ and $\alpha_{r\phi}$ show opposite signs at the equator near the surface. We associate these differences from Warnecke et al. (2018) with the milder rotational influence on convection, characterized by the Coriolis number, being roughly three times smaller in our run. The usage of the new definition of the turbulent transport coefficients could also have caused some of these differences, but this influence was checked to be very small by recomputing the coefficients for Warnecke et al. (2018) using the new convention. A detailed comparison is shown in Table 1 of Appendix A.

Concerning the turbulent pumping (see Figure 3), γ_r has a similar magnitude, γ_θ is 40% weaker and γ_ϕ is 40% stronger than in Warnecke et al. (2018). Here, too, the new definition has no significant effect. Note also the different normalization we used for $\boldsymbol{\gamma}$. γ_r is upward everywhere except in the bulk of the convection zone at mid and high latitudes. γ_θ is equatorward (poleward) in the upper (lower) half of the convection zone. γ_ϕ is prograde near the surface and at midlatitudes near the bottom, and negative everywhere else. The magnitudes of all three components are around 0.3 $u'_{\rm rms}$, where $u'_{\rm rms}(r, \theta) = \langle \boldsymbol{u}'^2 \rangle_{\phi t}^{1/2}$ is the local turbulent rms velocity in the meridional plane. The effective mean velocity resulting from $\boldsymbol{\gamma}$ is shown by its time average in Figures 2(e)–(g). The radial component, $\overline{U}_r^{\rm eff}$, is completely dominated by γ_r, leaving nearly no trace of the actual flow. γ_θ changes the sign of $\overline{U}_\theta$ only slightly below the surface and reduces its magnitude by around 30%. However, the meridional flow cells are completely destroyed, as shown by the flow lines in Figure 2(f). γ_ϕ is accelerating the equator and decelerating the polar region. The larger change in $\Omega^{\rm eff}$ compared to Warnecke et al. (2018) is because γ_ϕ increases with decreasing Ω_0.

The reconstruction of the turbulent EMF $\overline{\boldsymbol{\mathcal{E}}}$ based on Equation (4) shows reasonable agreement with $\overline{\boldsymbol{u}' \times \boldsymbol{b}'}$, see Appendix C. Therefore, we can confidently use the set of

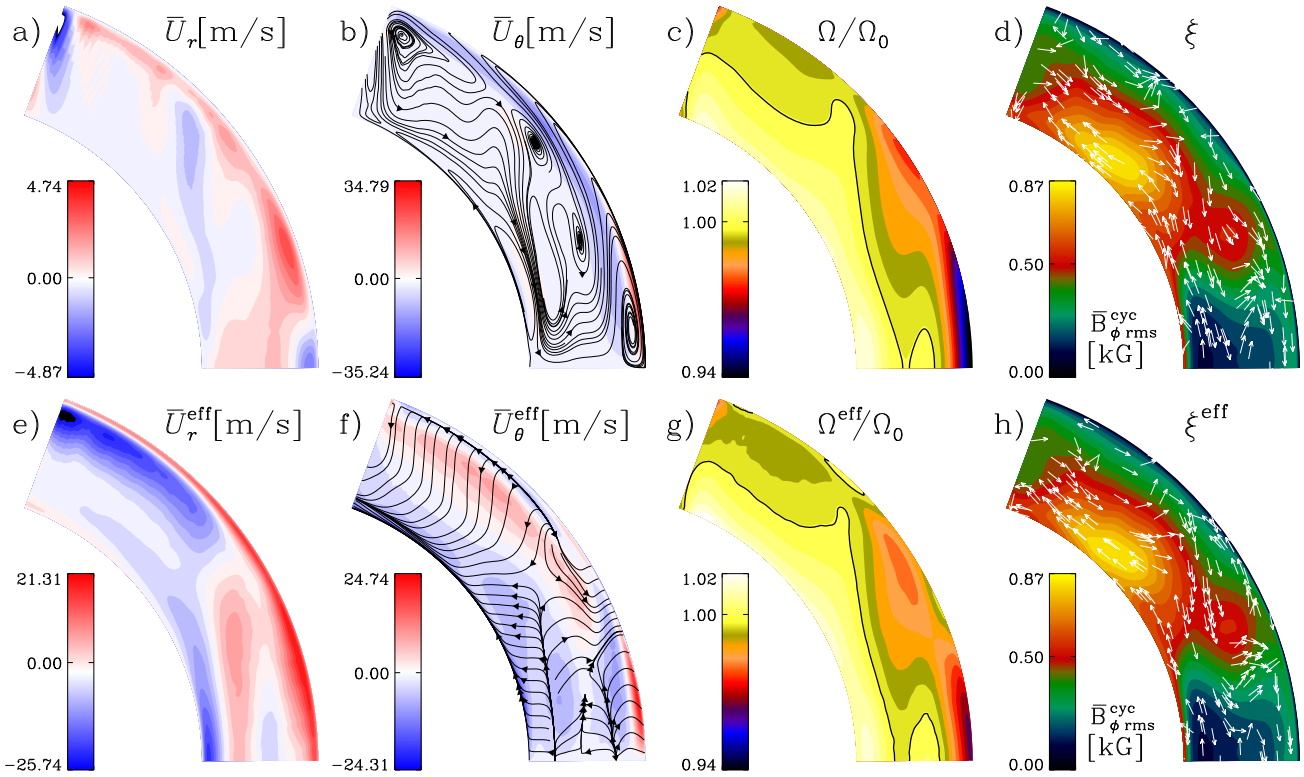

Figure 2. Time-averaged radial (a) and latitudinal (b) components of the meridional circulation ($\overline{U}_r$, $\overline{U}_\theta$, 0), (c) mean angular velocity $\Omega = \overline{U}_\phi/r \sin\theta + \Omega_0$ and (d) temporal rms value of the azimuthal component of the cyclic magnetic field $\overline{B}_\phi^{\mathrm{cyc}}$. (e)–(h): same as (a)–(d), but using the effective mean velocity. Flow lines in (b), (f): meridional and effective meridional circulation, respectively. Black lines in (c) and (g): $\Omega/\Omega_0 = 1$ and $\Omega^{\mathrm{eff}}/\Omega_0 = 1$, respectively. Arrows in (d), (h): direction of the Parker–Yoshimura dynamo wave propagation, see Equation (10).

turbulent transport coefficients to describe the dynamo processes in this run.

3.4. Dynamo Cycles and Migration

As a first step in determining the possible dynamo mechanism, we compare the period of the magnetic field cycle with theoretical expectations. We compute the magnetic cycle period by Fourier transforming $\overline{B}_\phi$ at $r = 0.98R$ and then averaging the spectra over latitude. As a result, we get $P_{\mathrm{cyc}} = (3.2 \pm 0.3)$ yr, where the error is obtained from the width at half maximum.

The two main dynamo scenarios both make predictions for the dynamo cycle length P_{cyc}. The Parker–Yoshimura dynamo period is locally defined as (Parker 1955; Yoshimura 1975)

$$P_{\mathrm{PY}} = 2\pi \left| \frac{\alpha_{\phi\phi} k_\theta}{2} r \cos\theta \, \partial_r \Omega \right|^{-1/2}, \qquad (7)$$

where $k_\theta = 2\pi/(r\Delta\theta)$ is the latitudinal wavenumber of the dynamo wave with $\Delta\theta = \pi/2 - \theta_0$. The justification of using only $\alpha_{\phi\phi}$ in Equation (7) is that the other contributions to the poloidal field generation are smaller.

The cycle period of an advection-dominated dynamo is related to the travel time of the meridional circulation from the equator to the pole, τ_{MC}, such that $P_{\mathrm{MC}} \approx 2\,\tau_{\mathrm{MC}}$ (Küker et al. 2001, 2019). Hence, in our notations, the expected cycle period can be written as

$$P_{\mathrm{MC}} = \frac{2r\Delta\theta}{\overline{U}_{\mathrm{MC}}(r,\theta)} \qquad (8)$$

where $\overline{U}_{\mathrm{MC}}$ is the temporal rms[5] of the meridional flow at the location of the dynamo wave. Traditionally, advection-dominated dynamo models assume the meridional flow and the resulting migration to be significant near the bottom of the convection zone, which would correspond to setting $r = 0.7\,R$, but in the present case it is not so straightforward to determine the location of the dynamo wave.

We start by using the measured radial DR in Equation (7), and meridional flow in Equation (8), and obtain for the averages over the convection zone $\langle P_{\mathrm{PY}}\rangle_{r\theta} = 2.2$ yr and $\langle P_{\mathrm{MC}}\rangle_{r\theta} = 8.2$ yr. Using the meridional circulation in the lower quarter of the convection zone only, we obtain, instead, $\langle P_{\mathrm{MC}}\rangle_{\delta r\theta} = 63.8$ yr, where δr goes from $0.7R$ to $R/4$. Considering the relevant role of the turbulent pumping, especially in $\overline{U}_r$, we also calculated the periods using the effective velocity, that is adding the contributions of turbulent pumping to the measured large-scale flows, obtaining $\langle P_{\mathrm{PY}}^{\mathrm{eff}}\rangle_{r\theta} = 2.0$ yr, $\langle P_{\mathrm{MC}}^{\mathrm{eff}}\rangle_{r\theta} = 5.6$ yr, and $\langle P_{\mathrm{MC}}^{\mathrm{eff}}\rangle_{\delta r\theta} = 22.0$ yr. The Parker–Yoshimura periods are less affected than those from meridional circulation, as the γ contribution is more significant for the meridional circulation than for the DR. In conclusion, the Parker–Yoshimura periods are consistent with the measured magnetic cycle, while advection by meridional flow cannot explain it.

If the mean magnetic field was advected by the meridional flow or its effective counterpart, one would not be able to explain poleward migration virtually everywhere within the convection zone. This becomes evident from Figures 2(b) and

[5] We define the temporal rms for a quantity f as $\sqrt{\langle f^2\rangle_t}$.

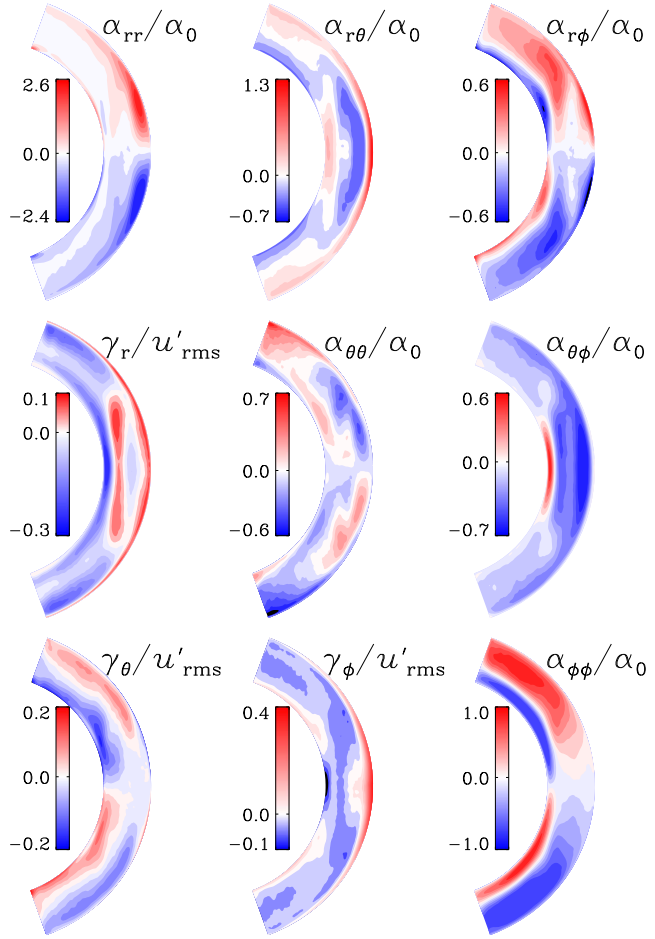

Figure 3. Independent components of time-averaged $\boldsymbol{\alpha}$, normalized by $\alpha_0 = u'_{\rm rms}/3$, and $\boldsymbol{\gamma}$, normalized by $u'_{\rm rms}$.

(f), where equatorward flows are present. Whether the meridional circulation is able to overcome diffusion, can be assessed by help of the corresponding dynamo number (or turbulent magnetic Reynolds number)

$$C_U = \Delta r \, \langle \overline{U}_{\rm MC} \rangle_{r\theta} / \langle \, {\rm Tr}\, \{\boldsymbol{\beta}\} \rangle_{r\theta}, \tag{9}$$

where Tr $\{\cdot\}$ indicates the trace. The time-averaged value for the measured mean and the effective mean flow are 0.2 and 0.6, respectively. Values below unity imply that the (effective) flow cannot overcome diffusion, not even with $\boldsymbol{\gamma}$ included; therefore, the advection-dominated dynamo scenario is not applicable here. However, the obtained values indicate that the meridional circulation may not be completely negligible in the magnetic evolution.

The prediction for the Parker–Yoshimura wave propagation direction given by (Yoshimura 1975)

$$\boldsymbol{\xi}(r, \theta) = -\alpha_{\phi\phi} \hat{\boldsymbol{e}}_\phi \times \boldsymbol{\nabla}\Omega, \tag{10}$$

is depicted in Figures 2(d) and (h) for the shear from Ω and $\Omega^{\rm eff}$, respectively. Near the bottom of the convection zone, where also the cyclic field is strongest, $\boldsymbol{\xi}$ is poleward at almost all latitudes, which would agree with the actual field propagation. In the bulk of the convection zone, however, the predicted direction is equatorward, failing to explain the actual migration. Hence, neither the Parker–Yoshimura dynamo wave nor the advection-dominated dynamo alone can be responsible for the oscillating poleward-migrating magnetic field throughout the convection zone.

3.5. Dynamo Drivers

To understand the failure of the simple dynamo scenarios in explaining cycles and migration of the field, we finally turn to computing the terms contributing to the magnetic field generation in detail. We present the contributions of the Ω and α effects, that is, of $\overline{\boldsymbol{B}} \cdot \boldsymbol{\nabla}\Omega$ and $\boldsymbol{\nabla} \times (\boldsymbol{\alpha} \cdot \overline{\boldsymbol{B}})$, in terms of their temporal rms values in Figure 4 employing the total magnetic field (upper row), and show the corresponding temporal rms magnetic fields in the lower row. The two leftmost (rightmost) columns show the generators for the poloidal (toroidal) magnetic field. From the magnitudes of the toroidal generators, it is evident that the α effect is equally important, or even dominant over the Ω effect. Hence, the generation of the toroidal field by the α effect is more efficient than by the Ω effect, suggesting an $\alpha^2\Omega$ or even an α^2 dynamo mechanism for the observed dynamo.

The Ω effect generates toroidal field efficiently at low latitudes near the surface and at midlatitudes in the bulk of the convection zone, coinciding with the surroundings of the local minimum of Ω. The α effect is strongest near the surface, but shows also toroidal field generation around the local minimum of Ω. The patches of strong rms toroidal field, however, overlap only partially with its generators, and its profile is clearly offset deeper into the convection zone. One reason might be the radial-field boundary condition, which suppresses any toroidal field near the surface. The α effect generates poloidal field mostly at high latitudes at all depths of the convection zone, although there are also regions of strong field generation close to the surface near the equator. The high-latitude field generator profiles match qualitatively better to the rms poloidal field distribution than to that of the toroidal field, but still the match is very incomplete.

The mismatch between the generators and the actual field distribution indicates that our conclusion of the generating mechanism being a simple $\alpha^2\Omega$ or α^2 dynamo is not a very solid one, and that other dynamo effects might be at play. For example, we find that the δ (Rädler) effect may also redound to the driving of the dynamo. Its contribution, shown in Figure 6 in Appendix A, is significant at midlatitudes near the surface for the poloidal field (panels a–b) and at the surface at all latitudes for the toroidal field (panel c). Particularly in the latter case, the contribution of $\boldsymbol{\delta}$ is strong in the same regions as the α and Ω effects and with roughly the same magnitude. However, this effect, in its simplest form in a shear flow, is known to lead to stationary solutions (Brandenburg & Subramanian 2005). Hence, its role for the oscillatory dynamo mode is likely to be negligible. How the δ effect contributes to the magnetic field generation needs to be analyzed in detail using mean-field simulations.

The study of Warnecke (2018) covers parameter regimes very close to the one explored here, but all of these solutions appear to exhibit only stationary or temporally irregular modes. This draws attention to the role of the wedge assumption used in that study. There, the computational domain covers only $\pi/2$ in azimuth, instead of the full 2π interval here, being virtually the only difference between these two studies. Our interpretation is that there are various dynamo modes excited with very similar critical dynamo numbers. In terms of dynamo theory,

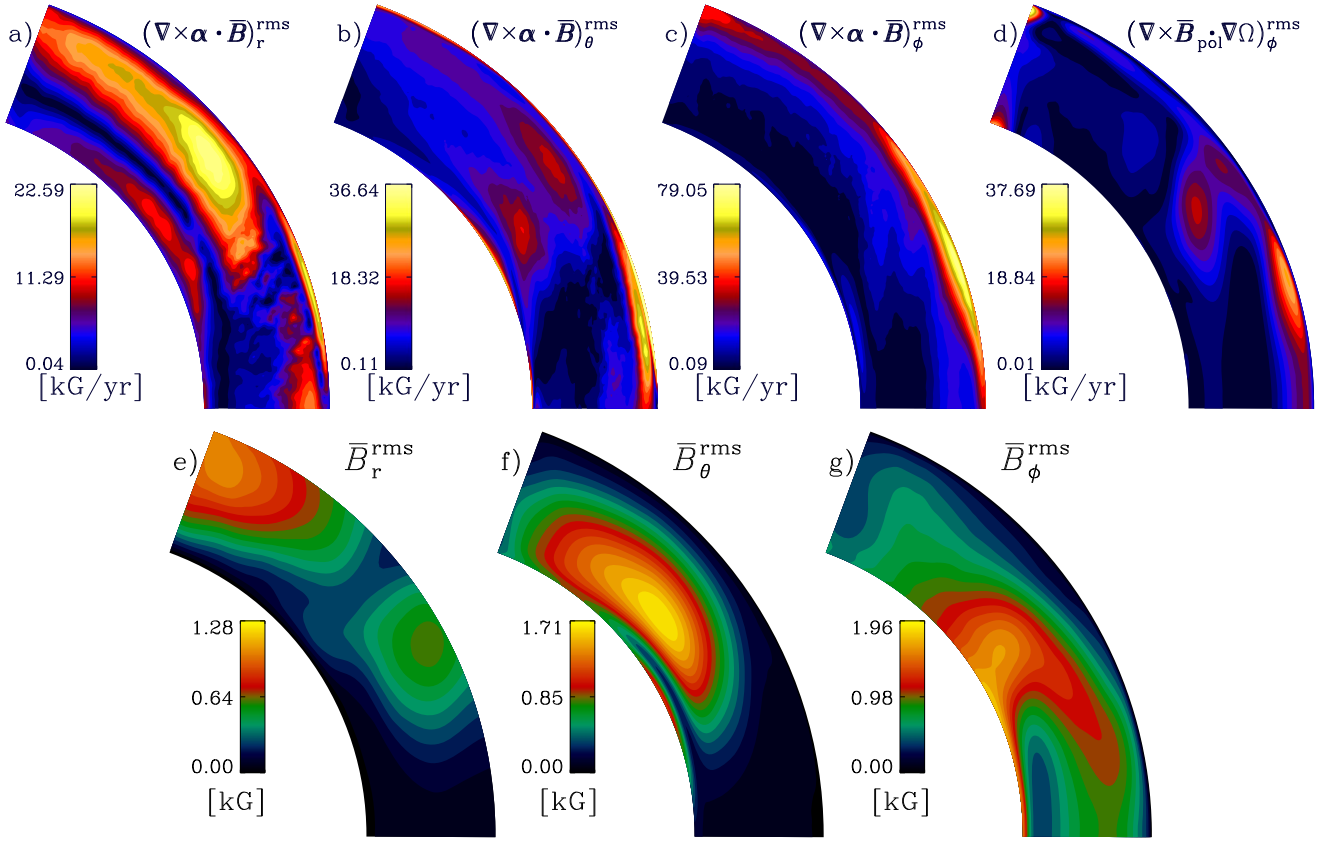

Figure 4. (a)–(d): temporal rms of the components of the α and Ω effect terms. (a), (b): poloidal field generators; (c), (d): toroidal field generators. (e)–(g): temporal rms values of the components of $\overline{\boldsymbol{B}}$.

the coexistence of a steady and an oscillating field constituent can be understood as follows: sufficiently overcritical flows enable the growth of more than one dynamo mode. Under the assumption of steady mean flows and statistically stationary turbulence, the time dependence of these eigenmodes is exponential with an, in general, complex increment. It is well conceivable that a nonoscillating and an oscillating mode are both excited and even continue to coexist in their nonlinear stage, although their kinematic growth rates were different.

4. Conclusions

We presented and analyzed a spherical convective dynamo simulation located in the transitional regime between S and AS rotation profiles. Unlike the oscillatory or stationary/irregular dynamos, of the S and AS regimes, the dynamo consists of coexisting cyclic and stationary modes. Metcalfe et al. (2016) suggested that the drop in the variability level of stars slightly less active than the Sun could be the result of a shutdown of the dynamo. Motivated by our finding of coexisting cyclic and stationary modes, we rather interpret this drop to be due to a change in the dynamo type. We tried to explain the oscillating magnetic field as a Parker–Yoshimura-rule-obeying dynamo wave or within the advection-dominated framework. Neither of the two approaches alone can explain the results in terms of cycle period and migration direction, even if we take the turbulent contributions to the effective mean flow into account. One reason might be that the α effect plays here a more dominant role than in a simple $\alpha\Omega$ dynamo. Our claim is validated by the analysis of the field generators shown in Figure 4: the mean field is generated by cyclonic convection and DR together, suggestive of an $\alpha^2\Omega$ or α^2 dynamo. However, the spatial distributions of the generators do not match very well with those of the mean fields. This likely indicates that other dynamo effects may also play important roles, and we find evidence of a significant contribution from the δ effect. However, mean-field models that take into account all turbulent effects are needed to address this issue.

We acknowledge the HPC-EUROPA3 project (INFRAIA-2016-1-730897), supported by the EC Research Innovation Action under the H2020 Programme. M.V., M.J.K., P.J.K., and M.R. acknowledge the support of the Academy of Finland ReSoLVE Centre of Excellence (grant No. 307411). M.V. acknowledges being enrolled in the International Max Planck Research School for Solar System Science at the University of Göttingen (IMPRS). J.W. acknowledges funding by the Max-Planck/Princeton Center for Plasma Physics. P.J.K. acknowledges support from DFG Heisenberg grant (No. KA 4825/1-1). This project has received funding from the European Research Council (ERC) under the European Union's Horizon 2020 research and innovation programme (project "UniSDyn", grant agreement No. 818665). We acknowledge also support from the supercomputers at GWDG, at RZG in Garching, and in the facilities hosted by the CSC—IT Center for Science in Espoo, Finland, which are financed by the Finnish ministry of education.

Appendix A
Redefinition of the Turbulent Transport Coefficients

A.1. Motivation

As mentioned in Schrinner et al. (2007) and Warnecke et al. (2018), there is some arbitrariness in deriving the transport coefficients (see Equation (4)) from the (noncovariant) tensors $\tilde{\boldsymbol{a}}$ and $\tilde{\boldsymbol{b}}$ defined by

$$\overline{\mathcal{E}}_\kappa = \tilde{a}_{\kappa\lambda}\overline{B}_\lambda + \tilde{b}_{\kappa\lambda r}\partial_r\overline{B}_\lambda + \tilde{b}_{\kappa\lambda\theta}\partial_\theta\overline{B}_\lambda,\quad \kappa,\,\lambda = r,\,\theta,\,\phi, \tag{11}$$

which form the immediate outcome of the test-field method. Here, we specify a choice, different from the one employed earlier (see Schrinner et al. 2007; Warnecke et al. 2018; Warnecke 2018), and characterized by a maximum of vanishing components in $\boldsymbol{\kappa}$. As a consequence, the role of $\boldsymbol{\kappa}$ in the turbulent EMF $\overline{\boldsymbol{\mathcal{E}}}$ is reduced, while mainly that of $\boldsymbol{\beta}$ is enhanced. This is motivated by the difficulty to interpret $\boldsymbol{\kappa}$ physically, whereas $\boldsymbol{\beta}$ clearly stands for turbulent dissipation. As a meaningful side effect, the diagonal elements of the latter become equal for isotropic turbulence. Furthermore, localized appearances of negative definite $\boldsymbol{\beta}$, which are destructive to mean-field modeling, become more visible as less of the diffusive contributions (ideally none) are "hidden" in $\boldsymbol{\kappa}$. Thus, removing the negative definiteness in the redefined $\boldsymbol{\beta}$ has better prospects to render the mean-field model feasible.

A.2. Decomposition

In Equation (11), the components $\tilde{b}_{\kappa\lambda\phi}$ do not appear as all ϕ derivatives vanish. They show up in the definitions of $\boldsymbol{\alpha}$, $\boldsymbol{\beta}$, etc. though, but setting them arbitrarily cannot change $\overline{\boldsymbol{\mathcal{E}}}$. Here, we choose $\tilde{b}_{\kappa\lambda\phi} = -\tilde{b}_{\kappa\phi\lambda}$, in contrast to Schrinner et al. (2007) who set $\tilde{b}_{\kappa\lambda\phi} = 0$. Then we arrive at the following expressions for the transport coefficients, where underlines indicate new or altered terms in comparison to Schrinner et al. (2007):

$$\alpha_{rr} = \tilde{a}_{rr} - \tilde{b}_{r\theta\theta}/r \tag{12}$$

$$\alpha_{r\theta} = \alpha_{\theta r} = \frac{1}{2}(\tilde{a}_{r\theta} + \tilde{a}_{\theta r} + (\tilde{b}_{rr\theta} - \tilde{b}_{\theta\theta\theta})/r) \tag{13}$$

$$\alpha_{r\phi} = \alpha_{\phi r} = \frac{1}{2}(\tilde{a}_{r\phi} + \tilde{a}_{\phi r} - (\underline{\tilde{b}_{r\phi r} + \cot\theta\,\tilde{b}_{r\phi\theta}} + \tilde{b}_{\phi\theta\theta})/r) \tag{14}$$

$$\alpha_{\theta\theta} = \tilde{a}_{\theta\theta} + \tilde{b}_{\theta r\theta}/r \tag{15}$$

$$\alpha_{\theta\phi} = \alpha_{\phi\theta} = \frac{1}{2}(\tilde{a}_{\theta\phi} + \tilde{a}_{\phi\theta} - (\underline{\tilde{b}_{\theta\phi r} + \cot\theta\,\tilde{b}_{\theta\phi\theta}} - \tilde{b}_{\phi r\theta})/r) \tag{16}$$

$$\alpha_{\phi\phi} = \tilde{a}_{\phi\phi} - (\underline{\tilde{b}_{\phi\phi r} + \cot\theta\,\tilde{b}_{\phi\phi\theta}})/r \tag{17}$$

$$\gamma_r = \frac{1}{2}(\tilde{a}_{\phi\theta} - \tilde{a}_{\theta\phi} + (\underline{\tilde{b}_{\theta\phi r} + \cot\theta\,\tilde{b}_{\theta\phi\theta}} + \tilde{b}_{\phi r\theta})/r) \tag{18}$$

$$\gamma_\theta = \frac{1}{2}(\tilde{a}_{r\phi} - \tilde{a}_{\phi r} + (\tilde{b}_{\phi\theta\theta} - \underline{\tilde{b}_{r\phi r} - \cot\theta\,\tilde{b}_{r\phi\theta}})/r) \tag{19}$$

$$\gamma_\phi = \frac{1}{2}(\tilde{a}_{\theta r} - \tilde{a}_{r\theta} - (\tilde{b}_{rr\theta} + \tilde{b}_{\theta\theta\theta})/r) \tag{20}$$

$$\beta_{rr} = -\underline{1}\cdot\tilde{b}_{r\phi\theta} \tag{21}$$

$$\beta_{r\theta} = \beta_{\theta r} = \frac{1}{\underline{2}}(\tilde{b}_{r\phi r} - \tilde{b}_{\theta\phi\theta}) \tag{22}$$

$$\beta_{r\phi} = \beta_{\phi r} = \frac{1}{4}(-\underline{2}\tilde{b}_{\phi\phi\theta} + \tilde{b}_{rr\theta} - \tilde{b}_{r\theta r}) \tag{23}$$

$$\beta_{\theta\theta} = \underline{1}\cdot\tilde{b}_{\theta\phi r} \tag{24}$$

$$\beta_{\theta\phi} = \beta_{\phi\theta} = \frac{1}{4}(\underline{2}\tilde{b}_{\phi\phi r} + \tilde{b}_{\theta r\theta} - \tilde{b}_{\theta\theta r}) \tag{25}$$

$$\beta_{\phi\phi} = \frac{1}{2}(\tilde{b}_{\phi r\theta} - \tilde{b}_{\phi\theta r}) \tag{26}$$

$$\delta_r = \frac{1}{4}(\tilde{b}_{\theta\theta r} - \tilde{b}_{\theta r\theta} + \underline{2}\tilde{b}_{\phi\phi r}) \tag{27}$$

$$\delta_\theta = \frac{1}{4}(\tilde{b}_{rr\theta} - \tilde{b}_{r\theta r} + \underline{2}\tilde{b}_{\phi\phi\theta}) \tag{28}$$

$$\delta_\phi = -\frac{1}{\underline{2}}(\tilde{b}_{r\phi r} + \tilde{b}_{\theta\phi\theta}) \tag{29}$$

$$\kappa_{irr} = -\tilde{b}_{irr} \tag{30}$$

$$\kappa_{ir\theta} = \kappa_{i\theta r} = -\frac{1}{2}(\tilde{b}_{ir\theta} + \tilde{b}_{i\theta r}) \tag{31}$$

$$\kappa_{ir\phi} = \kappa_{i\phi r} = \underline{0} \tag{32}$$

$$\kappa_{i\theta\theta} = -\tilde{b}_{i\theta\theta} \tag{33}$$

$$\kappa_{i\theta\phi} = \kappa_{i\phi\theta} = \underline{0} \tag{34}$$

$$\kappa_{i\phi\phi} = 0. \tag{35}$$

The results from the new definition are shown in Figure 3 for $\boldsymbol{\alpha}$ and $\boldsymbol{\gamma}$ and in Figure 5 for the six independent components of $\boldsymbol{\beta}$, the vector $\boldsymbol{\delta}$ (first three columns), and for the nine independent nonzero components of $\boldsymbol{\kappa}$ (last three columns). $\boldsymbol{\beta}$, $\boldsymbol{\delta}$, and $\boldsymbol{\kappa}$ are normalized by $\eta_{t0} = u'_{\rm rms}\alpha_{\rm MLT}H_p/3$, where $\alpha_{\rm MLT} = 5/3$ is the mixing-length parameter and $H_p = -1/\partial_r \ln p$ is the pressure scale height. The terms contributing to the magnetic field evolution from the δ (Rädler) effect, using the new definition, are shown in Figure 6.

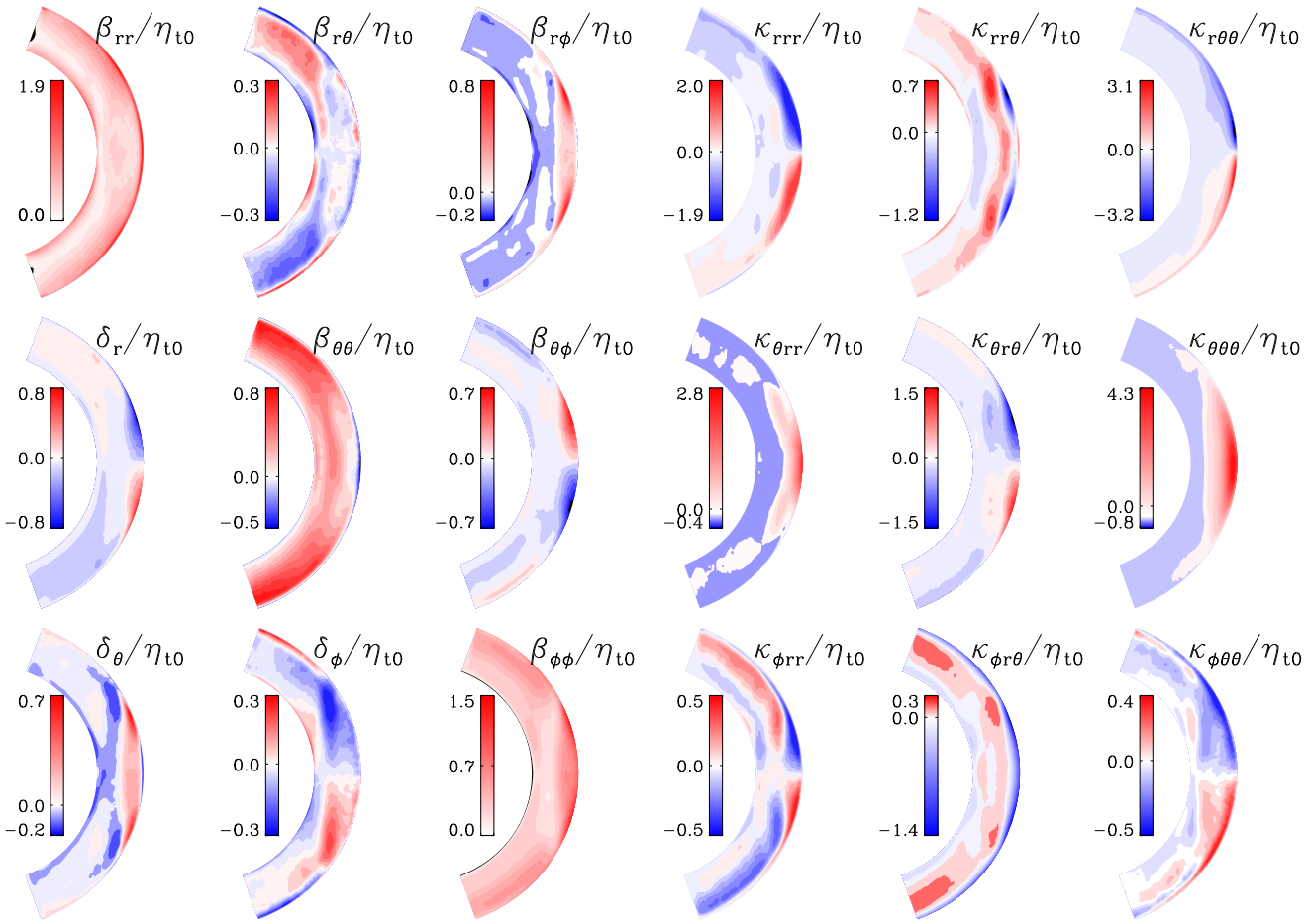

Figure 5. Independent components of time-averaged $\boldsymbol{\beta}$ and $\boldsymbol{\delta}$ (first three columns), and the nine independent nonzero components of time-averaged $\boldsymbol{\kappa}$ (last three columns), normalized by $\eta_{t0} = u'_{\rm rms}\alpha_{\rm MLT}H_p/3$.

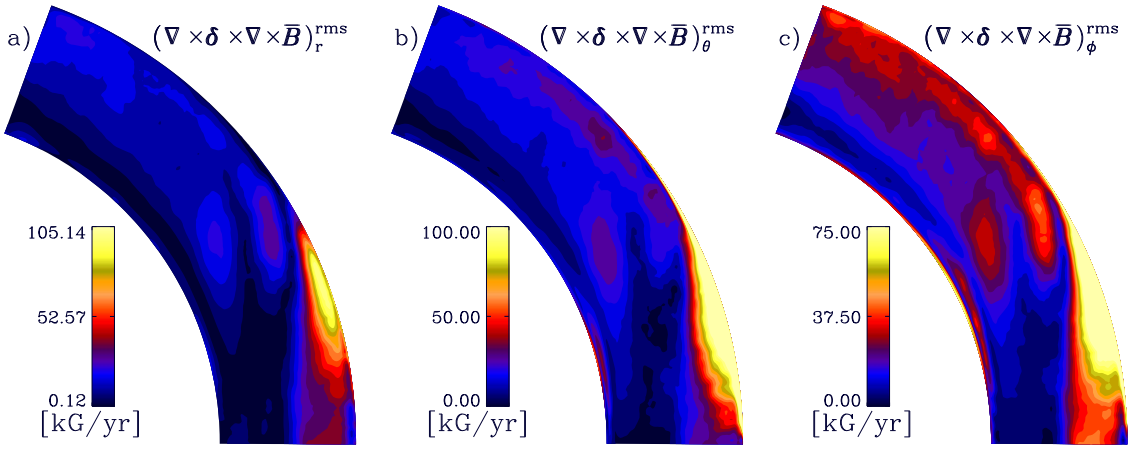

Figure 6. Temporal rms of the components of the δ (Rädler) effect, $\nabla\times\boldsymbol{\delta}\times\nabla\times\bar{\boldsymbol{B}}$, see Equation (4).

Appendix B
Comparison of the Turbulent Transport Coefficients to Warnecke et al. (2018)

We summarize the ratios of the turbulent transport coefficients from this study and their corresponding values from Warnecke et al. (2018) in Table 1. Note that all coefficients except $\beta_{\phi\phi}$ and the nonvanishing components of $\boldsymbol{\kappa}$ are affected by the redefinition explained in Appendix A, and β_{rr} and $\beta_{\theta\theta}$ are now twice as large as with the old definition. The extrema of the β_{ij} are between 2.4 and 5 times larger than the ones in Warnecke et al. (2018), with only $\beta_{\phi\phi}$ having the same order of magnitude, while all the components of $\boldsymbol{\delta}$ are

Table 1
Comparison with Warnecke et al. (2018)

Coeff	q	Comments	Coeff	q	Comments	Coeff	q	Comments
α_{rr}	0.8		β_{rr}	2.4		κ_{rrr}	2.9	
$\alpha_{r\theta}$	1.9	opposite sign below surface	$\beta_{r\theta}$	2.5	opposite sign in deep CZ	$\kappa_{rr\theta}$	2.3	
$\alpha_{r\phi}$	0.7	opposite sign near equator in upper CZ	$\beta_{r\phi}$	2.9		$\kappa_{r\theta\theta}$	3.5	negative near surface
$\alpha_{\theta\theta}$	1.2	opposite sign	$\beta_{\theta\theta}$	4.5	weakly negative layer at surface	$\kappa_{\theta rr}$	7.0	
$\alpha_{\theta\phi}$	1.1		$\beta_{\theta\phi}$	5.0	opposite sign near surface	$\kappa_{\theta r\theta}$	3.7	opposite sign near surface
$\alpha_{\phi\phi}$	0.8		$\beta_{\phi\phi}$	1.1		$\kappa_{\theta\theta\theta}$	6.5	
γ_r	1.0		δ_r	4	opposite sign at surface	$\kappa_{\phi rr}$	1.1	opposite sign
γ_θ	0.6		δ_θ	2.4		$\kappa_{\phi r\theta}$	1.0	negative layer at surface
γ_ϕ	1.4		δ_ϕ	3.3		$\kappa_{\phi\theta\theta}$	1.4	

Note. q is the ratio of the respective extremal value from the present study to that of Warnecke et al. (2018).

between 2.4 and 4 times larger. The diagonal components of $\boldsymbol{\beta}$ all show positive values throughout the domain, except for a thin layer near the surface for $\beta_{\theta\theta}$. $\beta_{r\theta}$ is positive at high latitudes and shows a sign reversal at the bottom of the convection zone at low latitudes. $\beta_{\theta\phi}$ is symmetric about the equator and changes sign in depth. $\beta_{r\phi}$ has a positive layer outside the tangent cylinder and is near zero everywhere else.

δ_r changes sign at high latitudes and, with respect to δ_r in Warnecke et al. (2018), has the opposite sign at low latitudes near the surface. Like $\beta_{r\phi}$, δ_θ has also a positive layer outside the tangent cylinder, and two negative patches are present, roughly at the same location as the minimum in Ω. δ_ϕ is 1.5 times larger than by the old definition.

The $\boldsymbol{\kappa}$ components look, in general, smoother than in Warnecke et al. (2018). Most of the κ_{ijk} are now zero, leaving just nine independent nonzero components. κ_{rrr}, $\kappa_{rr\theta}$, $\kappa_{\theta r\theta}$, and $\kappa_{r\theta\theta}$ are roughly three times larger, $\kappa_{\phi\theta\theta}$ and $\kappa_{\phi r\theta}$ have similar magnitudes, while $\kappa_{\theta rr}$ and $\kappa_{\theta\theta\theta}$ are 7 and 6.5 times larger in the current study, respectively. $\kappa_{rr\theta}$ shows sign reversal near the surface, and $\kappa_{r\theta\theta}$ does not show any particular structure in the bulk of the convection zone, as was the case in Warnecke et al. (2018), too. $\kappa_{\theta rr}$ has strong positive values near the equator in the upper part of the convection zone, extending to mid-latitudes, while $\kappa_{\theta r\theta}$ is antisymmetric with respect to the equator, and has the opposite sign near the surface with respect to Warnecke et al. (2018). Two sign reversals in depth are visible in $\kappa_{\phi rr}$, and also $\kappa_{\phi r\theta}$ shows three layers in depth: two narrow negative ones at the top and bottom of the convection zone and a weakly positive one in the bulk.

While $\boldsymbol{\alpha}$ and $\boldsymbol{\gamma}$ do not differ markedly between the compared runs, the other tensors show variations by up to a factor of seven compared to Warnecke et al. (2018). Given that the roughly three-times-higher Coriolis number of their run is virtually the only relevant difference to our present run, we have to assign these changes to the effect of rotational quenching (see, e.g., Kitchatinov et al. 1994). This is supported by the findings of Brandenburg et al. (2012) for rotating homogeneous turbulence who report on a reduction of $\boldsymbol{\beta}$ and $\boldsymbol{\delta}$ by a factor of approximately three when Co is increased from two to eight, with an even stronger reduction in $\boldsymbol{\kappa}$.

Appendix C
Reconstruction of the Turbulent Electromotive Force

We show in Figure 7 the turbulent EMF, computed directly via $\overline{\boldsymbol{u}' \times \boldsymbol{b}'}$ and its reconstruction using Equation (4) with the time-averaged transport coefficients and the full $\overline{\boldsymbol{B}}$ during roughly five typical dynamo cycles. In the reconstructed and directly computed EMFs, we have filtered out the time average and all time-scales shorter than one year to highlight the oscillating pattern. The spatial and temporal structures of all components of the reconstructed EMF match the measured ones reasonably well. In Warnecke et al. (2018), a good match was found in the mid and high latitudes, while the near-equator behavior was captured less accurately. However, the time average was not removed there. Now we find good correspondence also at the equatorial regions. As in Warnecke et al. (2018), the magnitudes of the reconstructed EMF components tend to be overestimated. Here, this effect is most pronounced for the azimuthal component of the EMF, which is by a factor of 2.5 larger than the measured one. This can be interpreted as a consequence of nonlocalities in turbulent convection, and calls for the application of scale dependent test fields to the problem.

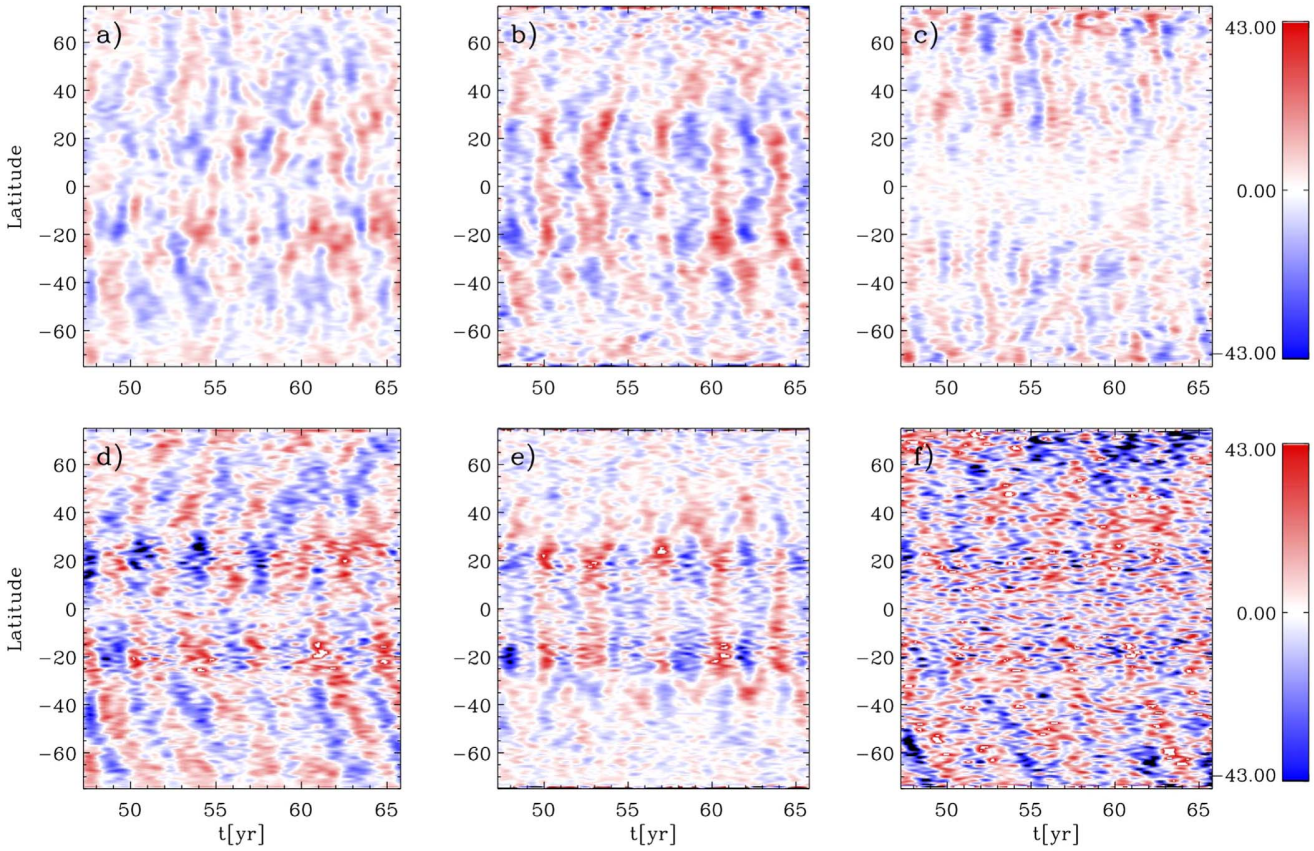

Figure 7. Radial, latitudinal, and longitudinal components of the turbulent electromotive force computed directly using $\overline{\boldsymbol{u}' \times \boldsymbol{b}'}$ (panels a–c) and of its reconstruction using Equation (4) (panels d–f) near the surface ($r = 0.98\,R$). Time averages and time-scales shorter than one year have been filtered out. The longitudinal components (panels c and f) have been multiplied by a factor 2.5.

ORCID iDs

M. Viviani https://orcid.org/0000-0003-3317-5889
M. J. Käpylä https://orcid.org/0000-0002-9614-2200
J. Warnecke https://orcid.org/0000-0002-9292-4600
P. J. Käpylä https://orcid.org/0000-0001-9619-0053
M. Rheinhardt https://orcid.org/0000-0001-9840-5986

References

Augustson, K., Brun, A. S., Miesch, M., & Toomre, J. 2015, ApJ, 809, 149
Baryshnikova, I., & Shukurov, A. 1987, AN, 308, 89
Brandenburg, A. 2017, A&A, 598, A117
Brandenburg, A., & Giampapa, M. S. 2018, ApJL, 855, L22
Brandenburg, A., Rädler, K.-H., & Kemel, K. 2012, A&A, 539, A35
Brandenburg, A., & Subramanian, K. 2005, PhR, 417, 1
Choudhuri, A. R., Schüssler, M., & Dikpati, M. 1995, A&A, 303, L29
Dikpati, M., & Charbonneau, P. 1999, ApJ, 518, 508
Featherstone, N. A., & Miesch, M. S. 2015, ApJ, 804, 67
Gastine, T., Yadav, R. K., Morin, J., Reiners, A., & Wicht, J. 2014, MNRAS, 438, L76
Gent, F. A., Käpylä, M. J., & Warnecke, J. 2017, AN, 338, 885
Käpylä, M. J., Käpylä, P. J., Olspert, N., et al. 2016, A&A, 589, A56
Käpylä, P. J., Gent, F. A., Olspert, N., Käpylä, M. J., & Brandenburg, A. 2019, GApFD, doi:10.1080/03091929.2019.1571586
Käpylä, P. J., Käpylä, M. J., & Brandenburg, A. 2014, A&A, 570, A43
Käpylä, P. J., Käpylä, M. J., Olspert, N., Warnecke, J., & Brandenburg, A. 2017, A&A, 599, A5
Käpylä, P. J., Korpi, M. J., & Tuominen, I. 2006, AN, 327, 884
Käpylä, P. J., Mantere, M. J., & Brandenburg, A. 2012, ApJL, 755, L22
Käpylä, P. J., Mantere, M. J., Cole, E., Warnecke, J., & Brandenburg, A. 2013, ApJ, 778, 41
Karak, B. B., Käpylä, P. J., Käpylä, M. J., et al. 2015, A&A, 576, A26
Kichatinov, L. L. 1991, A&A, 243, 483
Kitchatinov, L. L., Pipin, V. V., & Rüdiger, G. 1994, AN, 315, 157
Krause, F., & Rädler, K.-H. 1980, Mean-field Magnetohydrodynamics and Dynamo Theory (Oxford: Pergamon)
Küker, M., Rüdiger, G., Olah, K., & Strassmeier, K. G. 2019, A&A, 622, A40
Küker, M., Rüdiger, G., & Schultz, M. 2001, A&A, 374, 301
Mabuchi, J., Masada, Y., & Kageyama, A. 2015, ApJ, 806, 10
Masada, Y., & Sano, T. 2014, ApJL, 794, L6
Metcalfe, T. S., Egeland, R., & van Saders, J. 2016, ApJL, 826, L2
Mitra, D., Tavakol, R., Käpylä, P. J., & Brandenburg, A. 2010, ApJL, 719, L1
Olspert, N., Lehtinen, J. J., Käpylä, M. J., Pelt, J., & Grigorievskiy, A. 2018, A&A, 619, A6
Ossendrijver, M., Stix, M., Brandenburg, A., & Rüdiger, G. 2002, A&A, 394, 735
Parker, E. N. 1955, ApJ, 121, 491
Rädler, K.-H., & Bräuer, H.-J. 1987, AN, 308, 101
Schrinner, M. 2011, A&A, 533, A108
Schrinner, M., Petitdemange, L., & Dormy, E. 2011, A&A, 530, A140
Schrinner, M., Petitdemange, L., & Dormy, E. 2012, ApJ, 752, 121
Schrinner, M., Rädler, K.-H., Schmitt, D., Rheinhardt, M., & Christensen, U. 2005, AN, 326, 245
Schrinner, M., Rädler, K.-H., Schmitt, D., Rheinhardt, M., & Christensen, U. R. 2007, GApFD, 101, 81
Strugarek, A., Beaudoin, P., Charbonneau, P., Brun, A. S., & do Nascimento, J.-D. 2017, Sci, 357, 185
Viviani, M., Warnecke, J., Käpylä, M. J., et al. 2018, A&A, 616, A160
Warnecke, J. 2018, A&A, 616, A72
Warnecke, J., Käpylä, P. J., Käpylä, M. J., & Brandenburg, A. 2014, ApJL, 796, L12
Warnecke, J., Käpylä, P. J., Käpylä, M. J., & Brandenburg, A. 2016, A&A, 596, A115
Warnecke, J., Rheinhardt, M., Tuomisto, S., et al. 2018, A&A, 609, A151
Yoshimura, H. 1975, ApJ, 201, 740

5.3 Physically motivated heat conduction treatment in simulations of solar-like stars: effects on dynamo transitions

This Chapter has been used as a first draft for a paper submitted to A&A in June 2020.

Results from simulations of solar-like stars are at odds with observations in many respects: numerical models show an excess of power at large scales, anti-solar differential rotation profiles, with accelerated poles, for the solar rotation rate, and a transition to non-axisymmetric dynamos at a much lower rotation rate than the observed one. Even though the simulations reproduce the presence of active longitudes in fast rotators, the preferred migration direction for them is retrograde, instead of the mainly prograde migration direction seen in observations. The purpose of this study is to try to alleviate the discrepancies between observations and simulations. We used Kramers opacity law on a semi-global spherical setup describing convective envelopes of solar-like stars. We detected a shift of the axi- to non-axisymmetric transition at higher rotation rates and a change in the propagation direction of azimuthal dynamo waves. Also the transition to a solar-like rotational profile is shifted at higher rotation rate, in contrast to observations.

5.3.1 Introduction

The solar surface differential rotation has been known for a long time (Scheiner 1630, Carrington 1863): the equator completes a turn in around 25 days, while the poles take roughly 30 days. Helioseismology inferences have allowed also to uncover the subsurface rotation (Schou et al. 1998), and the actual radial differential rotation is weaker than expected: isorotation contours are inclined in the radial direction, showing that the Sun is able to break the Taylor-Proudman balance (Chandrasekhar 1961). Simulations of stellar convection in spherical or semi-spherical shells, though, show cylindrical isocontours for the differential rotation (e.g., Guerrero et al. 2013, Gastine et al. 2014, Käpylä et al. 2014, Augustson et al. 2015), implying a strong rotational influence. Latitudinal temperature variations can break the Taylor-Proudman balance and even a slight difference in temperature between the equator and the poles, of the order of few Kelvin, would be enough (Rüdiger 1989). This temperature difference is of the same order of magnitude as the error of current instruments, although Rast et al. (2008) reported on an enhancement of $\sim$ 2.5 K at the Sun's poles. The presence of a weakly subadiabatic layer at the base of the convection zone has been shown to generate a thermal wind and sustain the necessary temperature gradient in a mean-field hydrodynamic model (Rempel 2005). Another reason for the inclined contours could be an anisotropic convective heat transport, as investigated in Kitchatinov and Rüdiger (1995), that would lead to a temperature difference of $\sim$ 4 K. Simulations also show high power at large-scales, while time-distance helioseismology (Hanasoge et al. 2012) surprisingly revealed a lack of power at large scales, where the peak for giant cells should be located. Moreover, simulations are unable to reproduce an accelerated equator when using the solar rotation rate (Gastine et al. 2014, Käpylä et al. 2014, Karak et al. 2015). All the above mentioned discrepancies between observations and numerical models are collectively known as "convective conundrum" (see,

e.g., O'Mara et al. 2016) and solving it is one of the major challenges of contemporary solar physics.

Most of nowadays numerical setups are using fixed heat conduction profiles and convection zone (e.g., Brun et al. 2011, Käpylä et al. 2013), based on MLT, developed by Vitense (1953) and Böhm-Vitense (1958). In its original formulation, MLT predicts convection at the largest possible scale, which would correspond to cells of the diameter of the entire convective layer. Although MLT-designed setups have been successful in reproducing the pattern of granulation and supergranulation in surface convection, deeper convection simulations produce far more power at large scales than observations (Gizon and Birch 2012).

One proposed explanation is that the actual convectively unstable layer in the Sun, according to the Schwarzschild criterion (Chandrasekhar 1961), is shallower than expected. Scenarios along this line of thought have already been considered: Spruit (1997) described cool threads descending from the surface into deeper layers. Such a phenomenon is known as *entropy rain* (Brandenburg 2016) and describes surface driven convection, that would excite only small to mid-scales. By extending MLT to include entropy fluctuations, Brandenburg (2016) identified the presence of a Schwarzschild stable layer in which the convective flux is still positive. Such a layer was identified first in the Earth's atmosphere (Deardorff 1961, 1966). Models using Kramers opacity law, as an MLT independent description for heat flux, have demonstrated such non-local surface driving of convection in Cartesian (Käpylä et al. 2017, Käpylä 2018) and also spherical geometry (Käpylä et al. 2019a,b) both in hydrodynamic setups and including magnetic fields. Käpylä et al. (2017) found the numerical evidence of this sub-adiabatic, but still convective, layer (Deardorff zone) and consequently redefined the convection zone as the sum of the convection zone in the traditional sense, now called buoyancy zone, plus the Deardorff layer. The simulations in this work also included the presence of an overshoot zone and a radiative layer at the bottom. The depth of the layers is not determined a priori, but rather is an outcome of the simulation. The effect of subadiabatic layers in MHD simulations has been investigated in Käpylä et al. (2019b). The formation of a stably stratified layer at the bottom of the domain allows for the storage of magnetic field beneath it (see, also, Browning et al. 2006), but these strong fields may suppress the oscillating magnetic field at the surface. They also considered the effect of subadiabatic layers on the convective velocity spectra, but found that the decrease in power at large scales was not enough to solve the conundrum.

Another solution to the problem of higher convective velocities in simulations, proposed first in a Cartesian domain by Hotta et al. (2015a) and then in full spheres by Karak et al. (2018), is the feedback effect of the magnetic field on the velocity field through the Lorentz force. Small-scale dynamo could generate magnetic fields that would suppress the velocity field, acting, therefore, as an effective viscosity. To mimic this effect, Karak et al. (2018) increased the effective Prandtl number. Their simulations develop an overshoot zone at the base of the domain, and also show a decrease in the convective power at large scales, due to downward directed plumes. These results, although arising for a different reason, are consistent with the results of Käpylä et al. (2017) and Käpylä et al. (2019b). Another finding of Karak et al. (2018) is that the plumes, carrying their angular momentum inward, cause the rotation profile to switch to anti-solar.

Observations of fast rotating stars, younger and more active than the Sun, indicate con-

centrations of magnetic activity at high latitudes persisting for a long time (e.g., Berdyugina and Tuominen 1998). Such structures are constituted by two activity patches, one stronger than the other, and are identified as active longitudes (e.g., Jetsu 1996). Active longitudes usually migrate, forming azimuthal dynamo waves (ADW). The direction of migration of these structures can follow the plasma rotation, and in this case we will talk about prograde ADWs; they can also drift in the opposite direction (retrograde ADWs), or they can stand still with respect to the observer's point of view (standing ADW). These ADWs can persist for long periods of time (e.g., Lindborg et al. 2011), or their appearance can be more chaotic (e.g., Olspert et al. 2015), with a short-lived ADW reappearing after some time. ADW have been detected on many active stars (e.g., Berdyugina and Tuominen 1998). Lehtinen et al. (2016) and See et al. (2016) reported on a threshold in activity, above which stars show active longitudes. In the study of Lehtinen et al. (2016), the active longitudes are mostly migrating in the prograde direction. The appearance of active longitudes has been attributed to non-axisymmetric dynamo modes operating in these stars (Tuominen et al. 2002), in contrast to the axisymmetric dynamo operating in less active stars. The transition from non-axisymmetric to axisymmetric dynamos has also been studied numerically (Cole et al. 2014, Viviani et al. 2018), but these studies reported a majority of retrograde ADWs. Both studies were using prescribed and MLT-motivated profiles for heat conduction, resulting in a priori fixed depth of the convection zone.

The aim of this paper is to extend the study of Viviani et al. (2018) to include a dynamically adaptable heat conduction. In order to do this, we use a Kramers opacity law, as was done in Käpylä et al. (2019b) for semi-spherical wedge simulations. While wedge simulations exclusively allow to study axisymmetric solutions, our setup will allow us to study the effect of subadiabatic layers on non-axisymmetric dynamos.

5.3.2 Setup and Model

We apply a similar setup as in Käpylä et al. (2013) and Käpylä et al. (2019b), representing the outer envelope of solar-like stars, $0.7R \leq r \leq R$ (with R the radius of the star), in a semi-spherical domain, $0 \leq \phi \leq 2\pi$ and $\theta_0 \leq \theta \leq \pi - \theta_0$ ($\theta_0 = 15^o$). We solve numerically the system of MHD equations:

$$
\begin{aligned}
&\frac{\mathrm{D}\ln\rho}{\mathrm{D}t} + \nabla\cdot\boldsymbol{U} = 0,\\
&\frac{\mathrm{D}\boldsymbol{U}}{\mathrm{D}t} = \boldsymbol{g} - 2\boldsymbol{\Omega}_0\times\boldsymbol{U} + \frac{1}{\rho}\left(\boldsymbol{J}\times\boldsymbol{B} - \nabla p + \nabla\cdot 2\nu\rho\mathbf{S}\right),\\
&T\frac{\mathrm{D}s}{\mathrm{D}t} = \frac{1}{\rho}\left[-\nabla\cdot\left(\boldsymbol{F}^{\rm rad} + \boldsymbol{F}^{\rm SGS}\right) + \mu_0\eta\boldsymbol{J}^2 - \Gamma_{\rm cool}\right] + 2\nu\mathbf{S}^2,\\
&\frac{\partial\boldsymbol{A}}{\partial t} = \boldsymbol{U}\times\boldsymbol{B} - \mu_0\eta\boldsymbol{J},
\end{aligned}
\tag{5.1}
$$

where ρ and $\boldsymbol{U}$ are the density and the velocity field, $\boldsymbol{g} = -GM/r^3$ is the gravitational acceleration, with G the gravitational constant and M the mass of the star. $\boldsymbol{\Omega}_0 = \Omega_0\,(\cos\theta, -\sin\theta, 0)$ is the bulk rotation. $\boldsymbol{J}$, $\boldsymbol{B}$ and $\boldsymbol{A}$ are the current density, the magnetic field and the vector potential, respectively, p, ν and μ_0 are the pressure, the viscosity, and the magnetic permeability in vacuum, while $\mathbf{S}$ is the rate-of-strain tensor. $\boldsymbol{F}^{\rm rad}$ and $\boldsymbol{F}^{\rm SGS}$ are the radiative

and sub-grid scale (SGS) fluxes, expressed by:

$$\boldsymbol{F}^{\rm rad} = -K\nabla T \quad \boldsymbol{F}^{\rm SGS} = -\chi_{\rm SGS}\rho T\nabla s' \quad . \tag{5.2}$$

K is the radiative heat conductivity and $\chi_{\rm SGS}$ is the SGS heat diffusivity, assumed to be constant. s' is the fluctuating entropy, $s' = s - \langle\overline{s}\rangle_\theta$, where the overbar denotes longitudinal average and the brackets express averaging over the variable in the subscript. Finally, $\Gamma_{\rm cool}$ is a term acting near the surface and cooling to a reference temperature. Its flux is expressed as:

$$\overline{F}_{\rm cool} = \int_{0.7R}^{R} \Gamma_{\rm cool} dr. \tag{5.3}$$

The initial velocity and magnetic fields are gaussian seeds. The initial stratification is isoentropic. The radiative heat conductivity, K, follows Kramers opacity law for free-free and bound-free transitions (used, also, in Barekat and Brandenburg 2014, Käpylä et al. 2017, Käpylä 2018, Käpylä et al. 2019a,b):

$$K = K_0 \left(\frac{\rho}{\rho_0}\right)^2 \left(\frac{T}{T_0}\right)^{13/2} . \tag{5.4}$$

where ρ_0 and T_0 are reference values for density and temperature. The constant K_0 is defined via:

$$\begin{aligned} K_0 &= \frac{\mathcal{L}}{4\pi} c_v \left(\gamma - 1\right) \left(n_{\rm ad} + 1\right) \rho_0 \sqrt{GMR}, \\ \mathcal{L} &= \frac{L_0}{\rho_0 \left(GM\right)^{3/2} R^{1/2}}. \end{aligned} \tag{5.5}$$

$\mathcal{L}$ is the normalized luminosity, $c_{\rm V}$ is the specific heat at constant volume, $\gamma = c_{\rm P}/c_{\rm V}$ is the ratio between the specific heat at constant pressure and $c_{\rm V}$, and $n_{\rm ad} = 1.5$ is the adiabatic index.

The velocity field is impenetrable and stress free at all boundaries, while entropy derivatives are set to zero at $\theta = \theta_0$ and $\theta = \pi - \theta_0$. The magnetic field is radial at $r = R$ and a perfect conductor boundary condition is applied at the bottom boundary. At the latitudinal boundaries, $\boldsymbol{B}$ is tangential, which means:

$$A_r = A_\phi = \frac{\partial A_\theta}{\partial \theta} = 0 \qquad \text{at} \quad \theta = \theta_0 \quad \text{and} \quad \theta = \pi - \theta_0 \tag{5.6}$$

Käpylä et al. (2019a) showed that this latitudinal boundary condition does not generate major differences with respect to the perfect conductor boundary condition used in previous works (e.g., in Käpylä et al. 2013, Cole et al. 2014, Warnecke et al. 2014, Viviani et al. 2018).

The simulations are defined by the parameters Ω_0, ν, μ, $\chi_{\rm SGS}$, K_0, ρ_0, T_0 and the energy flux at the bottom, $F_{\rm bot} = -K\partial_r T$.

Moreover, important non-dimensional input parameters are the magnetic and SGS Prandtl numbers:

$$\mathrm{Pr_M} = \frac{\nu}{\mu}, \quad \mathrm{Pr_{SGS}} = \frac{\nu}{\chi_{\rm SGS}}, \tag{5.7}$$

with $\chi = K/c_{\rm P}\rho$. Output parameters of the simulations are the Reynolds numbers:

$$\mathrm{Re} = \frac{u_{\rm rms}}{\nu k_f}, \quad \mathrm{Rm} = \frac{u_{\rm rms}}{\eta k_f} \tag{5.8}$$

with $u_{\rm rms} = \sqrt{3/2 \left\langle U_r^2 + U_\theta^2 \right\rangle_{r\theta\phi t}}$ rms velocity and $k_f = 2\pi/0.3R$ the wavenumber of the largest eddy, corresponding to the radial extent, and the Coriolis number:

$$\mathrm{Co} = \frac{2\Omega_0}{u_{\rm rms} k_f}, \tag{5.9}$$

quantifying the relative importance of rotation and convection.

Physical units are chosen using the solar radius $R = 7 \cdot 10^8$ m, the solar angular velocity $\Omega_\odot = 2.7 \cdot 10^{-6}$ s^{-1}, the density at the bottom of the solar convection zone $\rho_{\rm bot} =$ 200 Kg m^{-3}, and the magnetic permeability $\mu_0 = 4\pi \cdot 10^{-7}$ H m^{-1}. We performed our simulations using the Pencil Code[1], a high-order, finite-difference, open source code.

5.3.3 Results

The simulations and their defining parameters are summarized in Table 5.1. Run R1 corresponds to Run C3 of Viviani et al. (2018), where we changed the heat conductivity description. We wanted to check the effect of more physical treatment for heat conduction on the anti-solar to solar-like differential rotation transition and the transition to non-axisymmetric magnetic fields. Run C3 was the slowest simulation showing both accelerated equator and non-axisymmetric magnetic field. We investigate the effect of the Kramers opacity law on this same setup in Run R1. Run R2 is the extension to 2π of Run MHD2 of Käpylä et al. (2019b). Wedge simulations covering 1/4 of the full longitude do not allow for non-axisymmetric solutions to develop, therefore, we extend the longitudinal domain of Run MHD2 and check whether the topology of the magnetic field is affected. Run R3 has the same setup as Run R2, but twice the rotation rate. Simulations in the same rotation range, but with fixed heat conduction profiles (e.g., Viviani et al. 2018), show a clear predominance of the non-axisymmetric mode over the axisymmetric one.

Run	$\Omega[\Omega_\odot]$	$\mathrm{Pr_{SGS}}$	$\mathrm{Pr_M}$	Re	Rm	Co	rBZ	rDZ	rOZ
R1	1.8	0.33	1.0	32	32	2.7(2.1)	0.769	0.767	0.710
R2	3.0	1.0	1.0	29	29	4.2(3.7)	0.773	0.738	0.706
R3	6.0	1.0	1.0	24	24	10.2(8.8)	0.778	0.740	0.710

Table 5.1: Summary of the runs. The values in parenthesis for Co indicate its value considering the wavenumber of the revised convection zone $k_{f\rm rev} = 2\pi/(R - r_{\rm DZ})$ (see, also, Käpylä et al. 2019b). Last three columns indicate the latitudinally and longitudinally averaged values for the depths of BZ, DZ and OZ.

We use the revised convection zone structure from Käpylä et al. (2019b), and indicate the bottom of the different layers in Figure 5.1 and Figure 5.2. The radial enthalpy flux is defined as $F_r^{\rm enth} = \overline{c_p (\rho \boldsymbol{u}_r)' T}$. The bottom of the buoyancy zone (BZ), in which the radial enthalpy flux is greater than zero, $F_r^{\rm enth} > 0$, and the radial entropy gradient is negative, $\partial_r s < 0$, is indicated with a continuous white line. We denote the bottom of the Deardorff layer (DZ), in which $F_r^{\rm enth} > 0$ and $\partial_r s > 0$, by a dashed line, and the

[1] https://github.com/pencil-code/

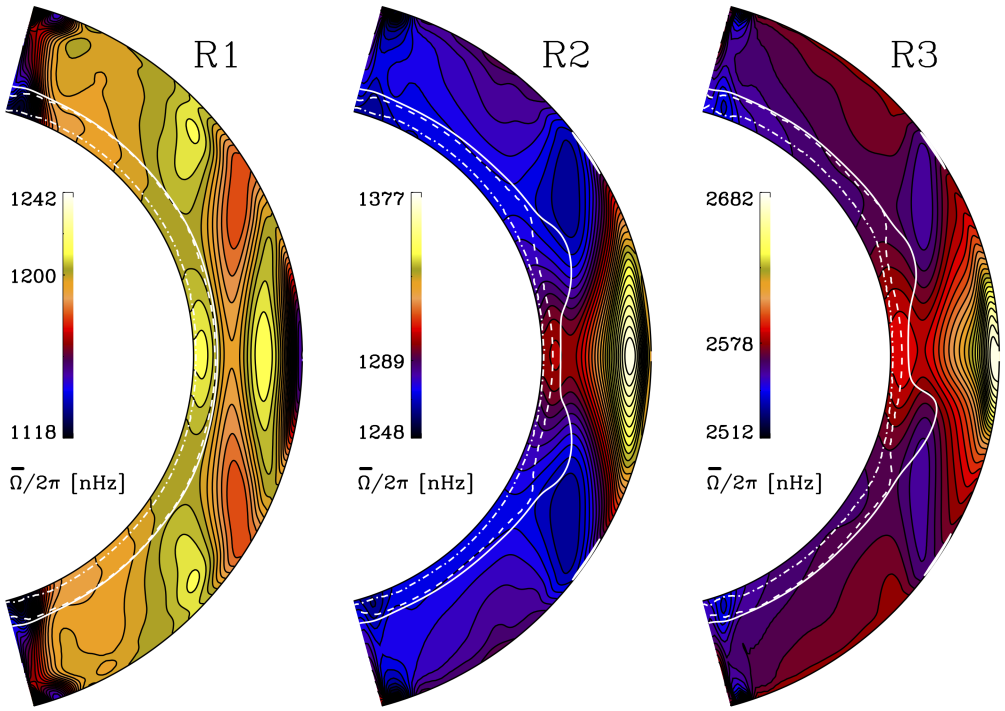

Figure 5.1: Differential rotation profiles. The continuous, dashed and dash-dotted lines represents, respectively, the bottom boundaries of BZ, DZ and OZ.

bottom of the overshoot zone (OZ), for which $F_r^{\text{enth}} < 0$ and $\partial_r s > 0$, with a dash-dotted line. In the radiative zone (RZ), $F_r^{\text{enth}} \approx 0$ and $\partial_r s > 0$. The values averaged over latitude for the depth of the layers are also shown in Table 5.1. We quote two Coriolis numbers for each simulation. The first one is obtained from Equation (5.9); the second one, listed in parenthesis in Table 5.1, takes into consideration the wavenumber of the revised convection zone (buoyancy zone and Deardorff zone), therefore we use $k_{frev} = 2\pi/(R - r_{\text{DZ}})$, where r_{DZ} is the latitudinally averaged radius of the Deardorff layer.

5.3.3.1 Convective states

We show the differential rotation profiles in Figure 5.1. Run R1 corresponds to the simulation with the lowest rotation rate showing an accelerated equator in Viviani et al. (2018), the rotation profile in that case being quite solar-like. With an adaptable heat conduction profile the rotation profile is less solar-like (see, Figure 5.1, left panel): the equatorial acceleration becomes less pronounced, the angular velocity contours are more cylindrical, and additional regions of negative shear appear at mid-latitudes and near the equatorial region close to the surface. The region of negative shear at mid-latitudes, in many simulations (e.g., Käpylä et al. 2012b, Warnecke et al. 2014), is responsible for the equatorward propagation of the magnetic field at the surface. In this case, though, the absolute differential rotation is smaller, placing this run even closer to the anti-solar to solar-like

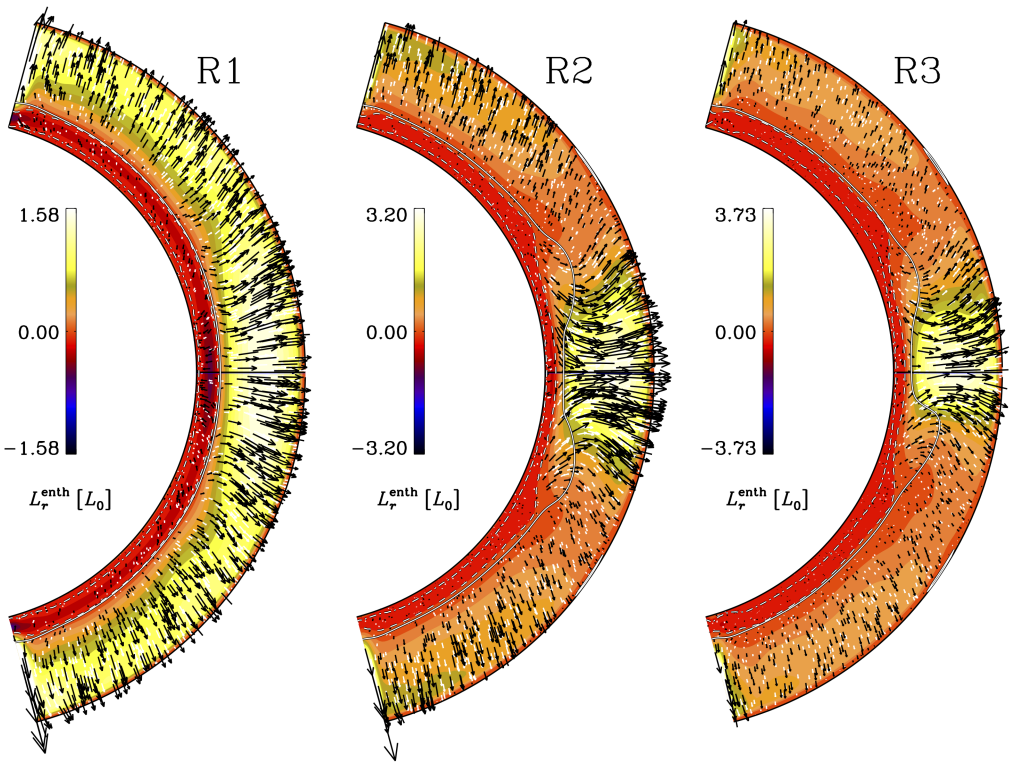

Figure 5.2: Radial $L^{\rm enth}$ normalized by L_0. The arrows show the direction of $L^{\rm enth}$. Continuous, dashed and dash-dotted lines as in Figure 5.1.

differential rotation transition. Hence, the contribution of the differential rotation to the large scale dynamo generation should be negligible. To assert this, though, a more thorough analysis needs to be performed. In this solution, the layers are rather isotropic in latitude, with a very thin DZ and a considerable OZ. A thin RZ develops at the bottom.

The rotation profile of Run R2 (Figure 5.1) is solar-like, showing an accelerated equator. The minimum at mid-latitudes is present, and its location corresponds to a subadiabatic region at the surface. A shear layer is present from mid to low latitudes at the surface. The layers vary more in latitude than in Run R1, with the BZ becoming shallower close to the tangent cylinder.

The rotation rate of Run R3 corresponds to Run H in Viviani et al. (2018), while its Coriolis number would correspond to Run G^a in the same setup. It seems to be a characteristic of the Kramers opacity law to produce higher convective velocities and, therefore, smaller Co. The rotation profile, shown in Figure 5.1, rightmost panel, closely resembles that of Run H, with a deep minimum at mid-latitudes, again, as for Run R2, corresponding to a subadiabatic surface region. A hemispheric asymmetry is present in the depth of the layers. The DZ is thicker at low latitudes and less isotropic next to the tangent cylinder.

We also inspect the radial enthalpy flux, $F_r^{\rm enth}$, by representing the enthalpy luminosity, $L^{\rm enth} = 4\pi r^2 F_r^{\rm enth}$, in Figure 5.2. The enthalpy flux in run R1 is isotropic in latitude and rather radial everywhere in the BZ, while a weak negative flux in the equatorial region

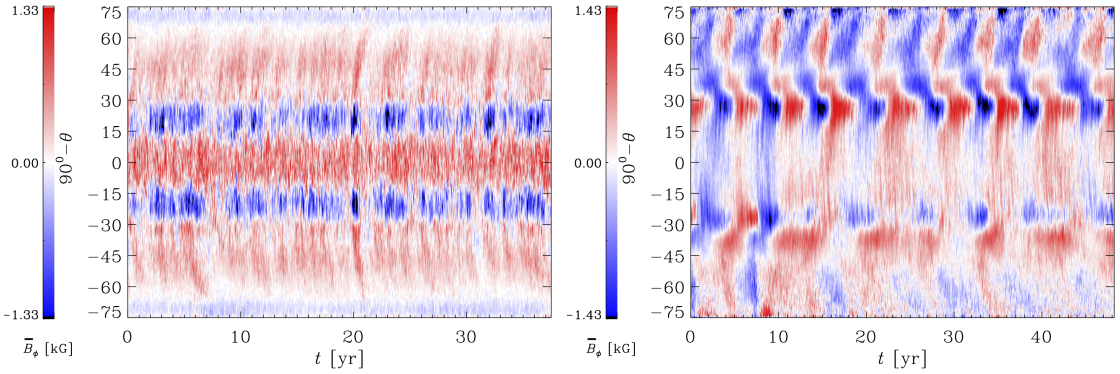

(a) R1 (b) R2

Figure 5.3: Azimuthal magnetic field at $r = 0.98R$ for Run R1 and Run R2.

is present in the OZ. A different situation arises for the two fast rotating runs, where the convective transport of energy is stronger at low latitudes. A clear equatorial asymmetry is present in L_r^{enth} for Run R3. This asymmetry is also reflected in the depth of the BZ, which becomes shallower just below the equator.

5.3.3.2 Axisymmetric magnetic field

We show the averaged longitudinal magnetic field near the surface, as a function of time, in Figure 5.3 and upper-left panel of Figure 5.4. Run R1 is characterized by equatorially symmetric magnetic field, with non-migrating negative polarities at low latitudes and slightly poleward migrating positive field at higher latitudes. A stationary negative field is present at all times close to the latitudinal boundary. This oscillating magnetic field was reported also in Viviani et al. (2019) and seems to be characteristic of models transitioning from solar-like to anti-solar differential rotation.

The equatorial propagation of the oscillating magnetic field in Run R2 is very similar to that of Run MHD2 in Käpylä et al. (2019b), also showing a similar periodicity of ~ 2 yr. In contrast to Run MHD2, the solution shows a pronounced hemispheric asymmetry, with a regular cycle in the northern hemisphere and an irregular periodicity in the southern hemisphere. The latter cycle seems to be longer than the one in the Northern hemisphere.

Run R3 presents two dynamo modes: a high frequency one in the southern hemisphere and a lower frequency one, with a periodicity similar to Run R2, in the northern hemisphere. By inspecting the magnetic field at different depths in Figure 5.4, we infer that the low frequency mode is generated in the OZ, while the high frequency one develops at a depth $0.80 \leq r \leq 0.85$, therefore at the bottom of the BZ. The existence of different dynamo modes at different depths has been reported already in other studies (such as Käpylä et al. 2016, 2019b).

5.3.3.3 Non-axisymmetric magnetic field

We present the results of the decomposition in the first 11 spherical harmonics ($0 \leq l, m \leq 10$) in Table 5.2. The decomposition was performed on the radial magnetic field near the surface of the simulation ($r = 0.98R$). Run R1 has a dominant axisymmetric large-scale

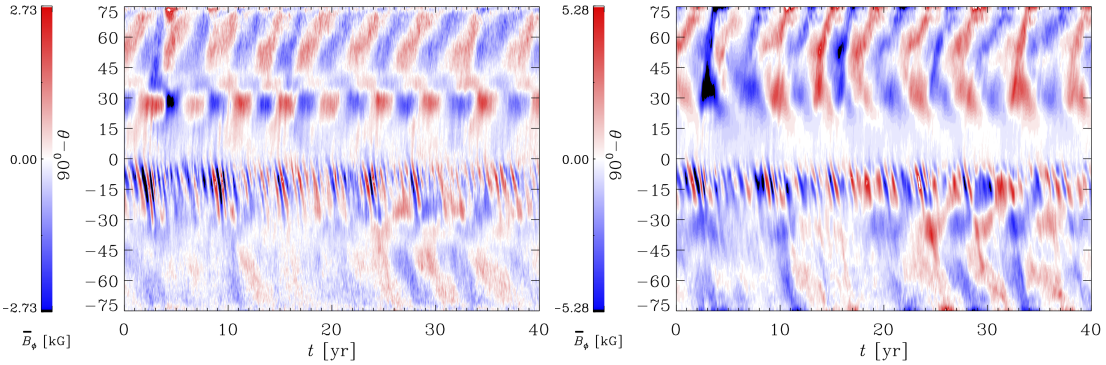

(a) R3[0.98R] (b) R3[0.86R]

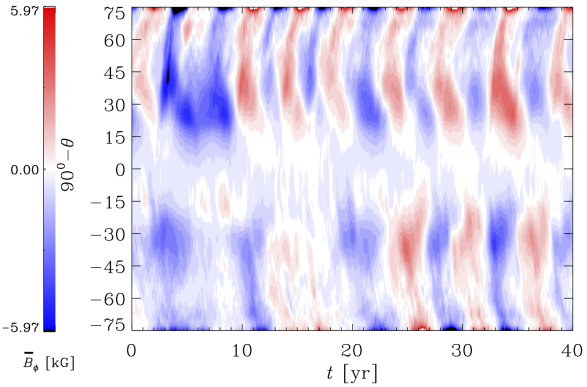

(c) R3[0.75R]

Figure 5.4: Azimuthal magnetic field for Run R3 at different depths.

Run	$E^{dec}_{mag,tot}$	E^{dec}_0	E^{dec}_1	E^{dec}_2	E^{dec}_3	E^{dec}_4	E^{dec}_5	$E^{dec}_{l,m>5}$
R1	1.4(-2)	4.9(-3)	1.6(-3)	8.2(-4)	7.5(-4)	8.0(-4)	8.5(-4)	4.5(-3)
R2	1.8(-2)	5.4(-3)	8.2(-3)	1.2(-3)	7.5(-4)	5.2(-4)	4.4(-4)	1.0(-3)
R3	5.0(-2)	1.2(-2)	2.6(-2)	3.4(-3)	1.7(-3)	1.2(-3)	1.0(-3)	4.2(-3)

Table 5.2: Magnetic energy from the decomposition in the first 11 spherical harmonics ($0 \leq l, m \leq 10$) of the near-surface ($r = 0.98R$) radial magnetic field. The labels E^{dec}_m indicate the energy in the corresponding m mode, in units of 10^5 J m^{-3}. We define $0 \leq l, m \leq 5$ the large scale field. The numbers in parenthesis represent the power of ten.

magnetic field, but also a significant contribution from the small-scale field ($l, m > 5$). The strength in the first non-axisymmetric large-scale mode is weak. This is opposite to the case in Viviani et al. (2018), where the same model with a fixed heat conduction profile was the slowest rotating one showing a substantial $m = 1$ component.

Run R2 is in a regime where the axisymmetric and the first non-axisymmetric mode have comparable strength, and this is reflected in the weak azimuthal dynamo wave in Figure 5.5, left panel, where we plot the reconstructed $m = 1$ mode at 45^o above the equator close to the surface as a function of time and longitude. The black-white dashed line represents the pattern of differential rotation at the same latitude. In the absence of a dynamo wave, the magnetic field would follow the propagation speed. Instead, in Figure 5.5, the magnetic field does not fall on the line for most of the time, hence, it has

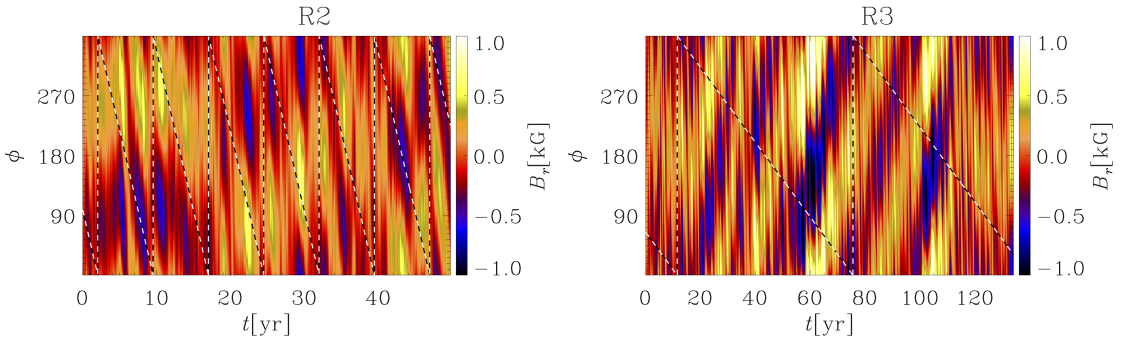

Figure 5.5: Azimuthal dynamo wave for Runs R2 and R3 as a function of longitude and time, at latitude $\theta = +45^o$ and depth $r = 0.98R$. The black and white dashed line represents the differential rotation at the same latitude.

its own motion as a wave, travelling in the prograde direction. The weak ADW in the case of Run R2 is a characteristic of simulations close to the axi- to non-axisymmetric transition (see, also Viviani et al. 2018). When the energy in the modes $m = 0$ and $m = 1$ is comparable, the wave can be affected by the differential rotation and it is advected for some time intervals (see Figure 5.5, left panel, 0 yr $\leq t \leq$ 15 yr). ADWs were already found in other numerical studies (Käpylä et al. 2013, Cole et al. 2014, Viviani et al. 2018), but their direction was mostly retrograde, in contrast with observational results (see, e.g., Lehtinen et al. 2016).

A stronger prograde ADW is also present in Run R3. The wave does not persist at all times, but there are periods when it disappears. The same behaviour was also observed, for example, in the temperature maps of the active star II Peg in Lindborg et al. (2011). We attribute the change in the ADW direction to the different heat conduction prescription in these runs.

5.3.4 Conclusions

In this paper we studied the effect of a dynamically adapting heat conduction prescription, based on Kramers opacity law, on semi-global MHD simulations. The main aim was to determine its effect on the two main transitions reported in numerical studies (e.g., Gastine et al. 2014, Viviani et al. 2018): the transition from accelerated poles and decelerated equator to a solar-like profile, with faster equator, and the transition from an axisymmetric magnetic field, as in the Sun, to a non-axisymmetric one, found in more rapid rotators. Previous studies (Viviani et al. 2018) reported these transitions occurring at the same rotation rate, in contrast with the current interpretation of observations. The fact that simulations usually produce anti-solar differential rotation for the solar rotation rate could indicate that the Sun is in a transitional regime (e.g., Käpylä et al. 2014, Metcalfe et al. 2016), or it could also mean that simulations still cannot fully capture the right rotational influence of the Sun. The study of Lehtinen et al. (2016) reported on strong non-axisymmetric fields and, therefore, places an upper limit for the transition to non-axisymmetric magnetic fields, that could actually happen at lower rotation rates but be out of range of the current detection methods. The fact that we do not see active longitudes on the Sun (Pelt et al. 2006), though, indicates that these two transitions should not

be located at the same rotation rate.

In low rotation runs, the rotation profile is significantly affected by the Kramers opacity law and, as a result, solutions with less solar-like characteristics, like an almost rigid body rotation and a minimum at mid-latitudes, develop. The different heat conduction prescription also promotes the formation of a stably stratified layer, rather isotropic in latitude, in the lower quarter of the domain. For faster rotating runs, the rotation profile is solar-like, but still maintains the minimum at mid-latitudes, and a latitudinally changing subadiabatic region is formed near the equator and the surface. Also, the Coriolis number is lower than in the corresponding cases using fixed profiles for heat conduction.

The convective transport is efficient, isotropic and almost radial everywhere in the convective region of Run R1, while is concentrated near the equator for Runs R2 and R3. Also, the BZ becomes shallower close to the tangent cylinder in the latter two cases. Run R3 presents a visibly equatorially asymmetric BZ profile.

The large-scale magnetic field is axisymmetric in Run R1, while for Run R2 and Run R3 the first non-axisymetric mode is dynamically important. Both the fast rotating runs have a hemispherically asymmetric oscillating magnetic field, with a periodicity of $\sim$ 2 years. The strong magnetic field in all the runs originates in the subadiabatic layer. In Run R3 a high-frequency mode is present in the southern hemisphere. This component is generated at the bottom boundary of the BZ. This is consistent with previous studies (e.g., Käpylä et al. 2016), using prescribed profiles for heat conduction. In the latter case, the high-frequency mode was generated near the surface, while the low-frequency one in the middle of the CZ.

In the non-axisymmetric runs, ADWs are present: a weak one for Run R2 and a stronger one for Run R3. In both cases, the direction is prograde, in agreement with photometric observations (Lehtinen et al. 2016). We remark here that in the previous numerical study using a prescribed heat conduction profile (Viviani et al. 2018), we found a preference for retrograde ADWs. The ADWs also show time variations. For Run R2, the ADW is rather weak and the differential rotation can advect it for some time, changing the direction of the wave. This could be caused by the comparable relative energies in the $m = 0$ and $m = 1$ modes. In Run R3 the stronger ADW disappears at certain times. This is also what is observed for active stars (e.g., Lindborg et al. 2011), where the active longitudes disappear or have the same velocity as the surface rotation.

In the presence of a Kramers opacity law, the flow and the magnetic field are both affected. The velocity field is more affected near the anti-solar to solar-like differential rotation transition, but all the runs are still in Taylor-Proudman balance, with almost cylindrical isocontours. For the same rotation rates, the Coriolis numbers are lowered, resulting in an anticipated transition to anti-solar differential rotation, in contrast with observations. The transition to non-axisymmetric magnetic fields is shifted at higher rotation rates. The direction of the ADW is reverted with respect to previous studies, producing a better agreement with observations.

6 Discussion and Conclusions

E quindi uscimmo a riveder le stelle.
Dante Alighieri, Inferno, XXXIV, 139, Divina Commedia

In this thesis, we investigated how the dynamo solutions in solar-like stars change as a function of different stellar parameters. In Section 5.1, we examined the effect of rotation. When the rotation rate is increased, the large-scale magnetic field shifts from an axisymmetric to a non-axisymmetric configuration. The transition is also accompanied by the appearance of azimuthal dynamo waves. This transition had already been observed for stars more active than the Sun (e.g., Lehtinen et al. 2016), but the numerical threshold in Co is lower than the one from observations. It has to be said that Lehtinen et al. (2016) detected highly non-axisymmetric magnetic fields, therefore, their transition point should be considered as an upper limit. Non-axisymmetric magnetic fields could be present also in less active stars than reported in Lehtinen et al. (2016), but they may be more difficult to detect with the current instrumentation. In our study, however, we detected non-axisymmetric fields at a too low rotation rate, the first non-axisymmetric solution being also the first one showing a solar-like rotation profile. This contrasts with solar observations not showing active longitudes (Pelt et al. 2006). An important aspect that emerged from Section 5.1 is that sufficiently high resolution is needed in order to maintain the same degree of supercriticality of convection: at fast rotation, runs with lower resolution revert to an axisymmetric configuration. Such a transition has not been observed and, therefore, could be a numerical artifact. Although the non-axisymmetric solutions fall on the superactive or transitional branch (Saar and Brandenburg 1999, Distefano et al. 2017) in the rotation-to-cycle-period-ratio versus rotation rate, the behaviour of the inactive branch is not captured. This seems to be a failure of many numerical models (for a more complete discussion, see Olspert et al. 2018), thus hinting towards a need for a revision of the current dynamo paradigms.

In Section 5.2, we analysed, by means of the test-field method, a simulation of the set of runs in Section 5.1, presenting an unusual combination of oscillating magnetic field and anti-solar differential rotation. By analysing the turbulent transport coefficients, we ruled out the possibility of an $\alpha\Omega$ dynamo as the cause of the oscillating field. Instead, the α-effect seems to be important in the regeneration of the toroidal field in this case, but also the δ-effect could be relevant. We reported on poleward migrating oscillating magnetic field for anti-solar differential rotation also in Section 5.3 (Run R1). This combination of rotational profile and magnetic field configuration, which we found for the first time, seems to be characteristic of solutions close to the differential rotation transition. Our results are important in the light of numerical (Gastine et al. 2014, Käpylä et al. 2014) and observational (Metcalfe et al. 2016) studies suggesting that the Sun could be close

to switching its rotation profile, and could also hint to a change in the operating dynamo mode accompanying the change in differential rotation.

As another defining parameter for simulations, we discussed the effect of a heat conduction profile depending on density and temperature in Section 5.3. The purpose of this study was to check if a Kramers opacity law, according to which the heat conductivity depends on temperature and density, instead of a fixed MLT-motivated profile could help in alleviating the discrepancies between observations and simulations known as *convective conundrum*. We expected an influence on the rotation profile and a more radially aligned countours of differential rotation profile, but the main difference in the flow was the more rigid rotation for a simulation close to the transition in differential rotation. Regarding the magnetic field, we found that the storage of strong field in the stably stratified layer leads to a high-latitude, poleward migrating, oscillating magnetic field for the slow rotating run. For the two runs rotating 3 and 6 times faster than the Sun, we detected equatorward propagating oscillating fields, found also in previous studies (e.g., Käpylä et al. 2012b, Warnecke et al. 2014). The dynamo periods do not seem to depend on the rotation rate, being similar (~ 2 yr) in both cases. In the fastest rotating run, a hemispherical high-frequency dynamo mode is present, and its origin seems to be at the bottom of the buoyancy zone. Also the presence of different dynamo modes at different depths is in agreement with previous studies (e.g., Käpylä et al. 2016, 2019b). We also considered the effect of Kramers opacity law on the transition to non-axisymmetric magnetic fields. The transition is moved to a higher rotation rate. The azimuthal dynamo waves move in the prograde direction, in agreement with the photometric study of Lehtinen et al. (2016).

The transition to non-axisymmetric magnetic fields needs to be studied further in full spherical models. Our setup without polar caps does not allow for polar concentrations of magnetic field to develop. These structures are characteristic of active, rapidly rotating stars, that present a dominant poloidal magnetic field component (see, e.g., See et al. 2016).

In order to better understand the results, additional analysis is required, for example, through the use of the test-field method. Since this method is based on axisymmetric averaging procedure, a complete re-design of the method to utilize non-Reynolds rules is necessary. Such kind of additional analysis of DNS should become customary, so to be able to interpret and clarify complex simulations.

The existence and the behaviour of stellar activity branches is still enigmatic: if at the beginning it looked like there were three of them (Inactive, Active and Superactive, see, Saar and Brandenburg 1999), more recent studies, considering longer time-series, question the existence of the Active branch (Distefano et al. 2017, Boro Saikia et al. 2018, Olspert et al. 2018). In particular, Olspert et al. (2018) focus their attention on the persistence of the Inactive branch and its inexplicable (using present theories) positive inclination. Indeed, according to mean-field estimates and if the α and the Ω effects increase with rotation, the slope of the Inactive branch should be negative, instead of the observed positive slope. The incapability of numerical models to capture the Inactive branch could be a consequence of low supercriticality of convection or the lack of shear layers, the tachocline and also the near surface shear layer. As stated in Chapter 3, the onset of convective instability increases as a function of rotation. This leads to more laminar solutions at fast rotation, a consequence of which could be the axisymmetric configuration for the large-scale magnetic field seen in Section 5.1. A better modeling strategy would involve

keeping the supercriticality fixed by scaling the other parameters, such as viscosity, as a function of increasing rotation. For less laminar models, the dependence of the cycle period on rotation could change, moving numerical results closer to observations.

Another issue for which an explanation is lacking is the predicted existence of giant cells from MLT, while only weak energy at their length scales is observed in heliosiesmic measurements. An explanation in the form of part of the solar convection zone being sub-adiabatic, which is not allowed by standard MLT, has been proposed. This could imply that convection is "driven from above" (Spruit 1997), and there is increasing evidence that this is the case (e.g., Brandenburg 2016, Käpylä et al. 2017). These studies extended MLT to include fluctuations in entropy. Recent models used Kramers opacity law (e.g., Käpylä et al. 2017), and reproduced the phenomenon of *entropy rain* described in Brandenburg (2016). The velocity spectra in Käpylä et al. (2019b) show less power at large length scales, but the decrease is not enough to solve the conundrum. Moreover, the shift to higher rotation rates of the axi- to non-axisymmetric transition found in Section 5.3, using Kramers law for opacity, is also accompanied by the shift to faster rotation of the transition in differential rotation, therefore to less realistic scenarios. Hence, prescribing a heat conduction dynamically adapting to the changes in temperature and density, is not sufficient to reduce the inconsistencies between numerical models and observational results. One more extension would be an even more realistic treatment of radiative transfer.

However, we stress again that the simulations are not in the same parameter regime as stellar convection, using enhanced values for viscosity and diffusivity, nor will they be in any foreseeable future. Still, we expect that next generation computers and new computing paradigms, such as accelerator platforms, allowing for computations with larger mesh sizes, will bring to a more relevant parameter regime. Thus, hopefully, also asymptotic behavior, in which the obtained results no longer depend on the mesh size used, will be reached. In the meantime, extensions (or revisions) of the classical theories of convection and dynamo seem to be necessary, in order for the next generation of numerical models to bring about an enhanced understanding of stellar interiors.

Bibliography

Augustson, K., Brun, A. S., Miesch, M., and Toomre, J.: 2015, *ApJ* **809**, 149

Augustson, K. C., Brun, A. S., and Toomre, J.: 2019, *ApJ* **876(1)**, 83

Babcock, H. W.: 1961, *ApJ* **133**, 572

Baliunas, S. L., Donahue, R. A., Soon, W. H., Horne, J. H., Frazer, J., Woodard-Eklund, L., Bradford, M., Rao, L. M., Wilson, O. C., Zhang, Q., Bennet, W., Briggs, J., Carrol, S. M., Duncan, D. K., Figueroa, D., Lanning, H. H., Misch, A., Mueller, J., Noyes, R. W., Poppe, D., Porter, A. C., Robinson, C. R., Russel, J., Shelton, J. C., Soyumer, T., Vaughan, A. H., and Whitney, J. H.: 1995, *ApJ* **438**, 269

Barekat, A. and Brandenburg, A.: 2014, *A&A* **571**, A68

Basu, S. and Antia, H. M.: 1997, *MNRAS* **287**, 189

Benomar, O., Bazot, M., Nielsen, M. B., Gizon, L., Sekii, T., Takata, M., Hotta, H., Hanasoge, S., Sreenivasan, K. R., and Christensen-Dalsgaard, J.: 2018, *Science* **361(6408)**, 1231

Berdyugina, S. V. and Tuominen, I.: 1998, *A&A* **336**, L25

Bogart, R. S., Baldner, C. S., and Basu, S.: 2015, *ApJ* **807(2)**, 125

Böhm-Vitense, E.: 1958, *ZAp* **46**, 108

Boro Saikia, S., Marvin, C. J., Jeffers, S. V., Reiners, A., Cameron, R., Marsden, S. C., Petit, P., Warnecke, J., and Yadav, A. P.: 2018, *A&A* **616**, A108

Brandenburg, A.: 2016, *ApJ* **832**, 6

Brandenburg, A., Nordlund, Å., and Stein, R. F.: 2000, *Astrophysical Convection and Dynamos*, pp 85–105, Gordon and Breach Science Publishers

Brandenburg, A., Rädler, K.-H., and Schrinner, M.: 2008, *A&A* **482**, 739

Brandenburg, A., Saar, S. H., and Turpin, C. R.: 1998, *ApJ* **498**, L51

Brandenburg, A. and Sokoloff, D.: 2002, *GAFD* **96**, 319

Brandenburg, A. and Subramanian, K.: 2005, *Phys. Rep.* **417**, 1

Browning, M. K., Miesch, M. S., Brun, A. S., and Toomre, J.: 2006, *ApJ* **648**, L157

Brun, A. S., Miesch, M. S., and Toomre, J.: 2004, *ApJ* **614**, 1073

Brun, A. S., Miesch, M. S., and Toomre, J.: 2011, *ApJ* **742**, 79

Bumba, V.: 1970, *Sol. Phys.* **14(1)**, 80

Cameron, R. H. and Schüssler, M.: 2017, *A&A* **599**, A52

Canuto, V. M.: 1989, *A&A* **217(1-2)**, 333

Carrington, R. C.: 1863, *Observations of the spots on the Sun*, London

Cattaneo, F., Brummell, N. H., Toomre, J., Malagoli, A., and Hurlburt, N. E.: 1991, *ApJ* **370**, 282

Cattaneo, F. and Hughes, D. W.: 1996, *Phys. Rev. E* **54**, 4532

Chandrasekhar, S.: 1961, *Hydrodynamic and hydromagnetic stability*

Charbonneau, P.: 2013, *Solar and Stellar Dynamos, Saas-Fee Advanced Courses, Volume 39. ISBN 978-3-642-32092-7. Springer-Verlag Berlin Heidelberg, 2013, p. 187* **39**, 187

Choudhuri, A. R., Schüssler, M., and Dikpati, M.: 1995, *A&A* **303**, L29

Christensen, U. R., Aubert, J., Cardin, P., Dormy, E., Gibbons, S., Glatzmaier, G. A., Grote, E., Honkura, Y., Jones, C., Kono, M., Matsushima, M., Sakuraba, A., Takahashi, F., Tilgner, A., Wicht, J., and Zhang, K.: 2001, *Physics of the Earth and Planetary Interiors* **128(1-4)**, 25

Christensen-Dalsgaard, J., Duvall, T. L., J., Gough, D. O., Harvey, J. W., and Rhodes, E. J., J.: 1985, *Nature* **315(6018)**, 378

Christensen-Dalsgaard, J., Monteiro, M. J. P. F. G., and Thompson, M. J.: 1995, *MNRAS* **276**, 283

Cole, E., Brandenburg, A., Käpylä, P. J., and Käpylä, M. J.: 2016, *A&A* **593**, A134

Cole, E., Käpylä, P. J., Mantere, M. J., and Brandenburg, A.: 2014, *ApJL* **780**, L22

Cossette, J.-F. and Rast, M. P.: 2016, *ApJ* **829**, L17

Cowling, T. G.: 1933, *MNRAS* **94**, 39

Deardorff, J. W.: 1961, *J. Atmosph. Sci.* **18**, 540

Deardorff, J. W.: 1966, *J. Atmosph. Sci.* **23**, 503

Deardorff, J. W.: 1972, *J. Geophys. Res.* **77**, 5900

Dikpati, M. and Charbonneau, P.: 1999, *ApJ* **518**, 508

Distefano, E., Lanzafame, A. C., Lanza, A. F., Messina, S., and Spada, F.: 2017, *A&A* **606**, A58

Duarte, L. D. V., Wicht, J., Browning, M. K., and Gastine, T.: 2016, *MNRAS* **456**, 1708

Duvall, Jr., T. L.: 1979, *Sol. Phys.* **63**, 3

Featherstone, N. A. and Hindman, B. W.: 2016a, *ApJ* **830**, L15

Featherstone, N. A. and Hindman, B. W.: 2016b, *ApJ* **818**, 32

Gastine, T., Yadav, R. K., Morin, J., Reiners, A., and Wicht, J.: 2014, *MNRAS* **438**, L76

Ghizaru, M., Charbonneau, P., and Smolarkiewicz, P. K.: 2010, *ApJ* **715**, L133

Gizon, L. and Birch, A. C.: 2012, *PNAS* **109**, pp.11896

Greer, B. J., Hindman, B. W., Featherstone, N. A., and Toomre, J.: 2015, *ApJ* **803**, L17

Guerrero, G., Smolarkiewicz, P. K., de Gouveia Dal Pino, E. M., Kosovichev, A. G., and Mansour, N. N.: 2016, *ApJ* **819**, 104

Guerrero, G., Smolarkiewicz, P. K., Kosovichev, A. G., and Mansour, N. N.: 2013, *ApJ* **779**, 176

Guerrero, G., Zaire, B., Smolarkiewicz, P. K., de Gouveia Dal Pino, E. M., Kosovichev, A. G., and Mansour, N. N.: 2019, *ApJ* **880**, 6

Hale, G. E., Ellerman, F., Nicholson, S. B., and Joy, A. H.: 1919, *ApJ* **49**, 153

Hanasoge, S. M., Duvall, T. L., and Sreenivasan, K. R.: 2012, *Proc. Natl. Acad. Sci.* **109**, 11928

Hathaway, D. H.: 1996, *ApJ* **140**, 1027

Hathaway, D. H.: 2011, p. arXiv:1103.1561

Hathaway, D. H., Upton, L., and Colegrove, O.: 2013, *Science* **342**, 1217

Hotta, H., Rempel, M., and Yokoyama, T.: 2015a, *ApJ* **803**, 42

Hotta, H., Rempel, M., and Yokoyama, T.: 2015b, *ApJ* **798**, 51

Hotta, H., Rempel, M., Yokoyama, T., Iida, Y., and Fan, Y.: 2012, *A&A* **539**, A30

Hubbard, A. and Brandenburg, A.: 2009, *ApJ* **706(1)**, 712

Jackson, A., Sheyko, A., Marti, P., Tilgner, A., Cébron, D., Vantieghem, S., Simitev, R., Busse, F., Zhan, X., Schubert, G., Takehiro, S., Sasaki, Y., Hayashi, Y. Y., Ribeiro, A., Nore, C., and Guermond, J. L.: 2014, *Geophysical Journal International* **196(2)**, 712

Jetsu, L.: 1996, *A&A* **314**, 153

Jones, C. A., Boronski, P., Brun, A. S., Glatzmaier, G. A., Gastine, T., Miesch, M. S., and Wicht, J.: 2011, *Icarus* **216(1)**, 120

Jouve, L., Brown, B. P., and Brun, A. S.: 2010, *A&A* **509**, A32

Jouve, L. and Brun, A. S.: 2007, *A&A* **474**, 239

Käpylä, M. J., Käpylä, P. J., Olspert, N., Brandenburg, A., Warnecke, J., Karak, B. B., and Pelt, J.: 2016, *A&A* **589**, A56

Käpylä, P. J.: 2018, *submitted to A&A,* p. arXiv:1812.07916

Käpylä, P. J., Brandenburg, A., Kleeorin, N., Mantere, M. J., and Rogachevskii, I.: 2012a, *MNRAS* **422**, 2465

Käpylä, P. J., Gent, F. A., Olspert, N., Käpylä, M. J., and Brandenburg, A.: 2019a, *GAFD (in press)*

Käpylä, P. J., Käpylä, M. J., and Brandenburg, A.: 2014, *A&A* **570**, A43

Käpylä, P. J., Korpi, M. J., Brandenburg, A., Mitra, D., and Tavakol, R.: 2010, *AN* **331**, 73

Käpylä, P. J., Korpi, M. J., Ossendrijver, M., and Stix, M.: 2006, *A&A* **455**, 401

Käpylä, P. J., Mantere, M. J., and Brandenburg, A.: 2012b, *ApJ* **755**, L22

Käpylä, P. J., Mantere, M. J., Cole, E., Warnecke, J., and Brandenburg, A.: 2013, *ApJ* **778**, 41

Käpylä, P. J., Rheinhardt, M., Brandenburg, A., Arlt, R., Käpylä, M. J., Lagg, A., Olspert, N., and Warnecke, J.: 2017, *ApJ* **845**, L23

Käpylä, P. J., Viviani, M., Käpylä, M. J., Brandenburg, A., and Spada, F.: 2019b, *GAFD* **133**, p.149

Karak, B. B., Käpylä, P. J., Käpylä, M. J., Brandenburg, A., Olspert, N., and Pelt, J.: 2015, *A&A* **576**, A26

Karak, B. B., Miesch, M., and Bekki, Y.: 2018, *Physics of Fluids* **30(4)**, 046602

Kitchatinov, L. L. and Rüdiger, G.: 1995, *A&A* **299**, 446

Kitchatinov, L. L. and Rüdiger, G.: 1999, *A&A* **344**, 911

Krause, F. and Rädler, K.-H.: 1980, *Mean-field Magnetohydrodynamics and Dynamo Theory*, Pergamon Press, Oxford

Ledoux, P.: 1947, *ApJ* **105**, 305

Lehtinen, J., Jetsu, L., Hackman, T., Kajatkari, P., and Henry, G. W.: 2016, *A&A* **588**, A38

Leighton, R. B.: 1969, *ApJ* **156**, 1

Lindborg, M., Korpi, M. J., Hackman, T., Tuominen, I., Ilyin, I., and Piskunov, N.: 2011, *A&A* **526**, A44

Mabuchi, J., Masada, Y., and Kageyama, A.: 2015, *ApJ* **806**, 10

Metcalfe, T. S., Egeland, R., and van Saders, J.: 2016, *ApJ* **826**, L2

Mitra, D., Tavakol, R., Brandenburg, A., and Moss, D.: 2009, *ApJ* **697**, 923

Moffatt, H. K.: 1978, *Magnetic Field Generation in Electrically Conducting Fluids*, Cambridge University Press, Cambridge

Monteiro, M. J. P. F. G., Christensen-Dalsgaard, J., and Thompson, M. J.: 1994, *A&A* **283(1)**, 247

Nordlund, Å., Stein, R. F., and Asplund, M.: 2009, *Living Reviews in Solar Physics* **6(1)**, 2

Noyes, R. W., Hartmann, L. W., Baliunas, S. L., Duncan, D. K., and Vaughan, A. H.: 1984a, *ApJ* **279**, 763

Noyes, R. W., Weiss, N. O., and Vaughan, A. H.: 1984b, *ApJ* **287**, 769

Olspert, N., Käpylä, M. J., Pelt, J., Cole, E. M., Hackman, T., Lehtinen, J., and Henry, G. W.: 2015, *A&A* **577**, A120

Olspert, N., Lehtinen, J. J., Käpylä, M. J., Pelt, J., and Grigorievskiy, A.: 2018, *A&A* **619**, A6

O'Mara, B., Miesch, M. S., Featherstone, N. A., and Augustson, K. C.: 2016, *Advances in Space Research* **58**, 1475

Parker, E. N.: 1955a, *ApJ* **122**, 293

Parker, E. N.: 1955b, *ApJ* **121**, 491

Passos, D. and Charbonneau, P.: 2014, *A&A* **568**, A113

Pelt, J., Brooke, J. M., Korpi, M. J., and Tuominen, I.: 2006, *A&A* **460**, 875

Racine, É., Charbonneau, P., Ghizaru, M., Bouchat, A., and Smolarkiewicz, P. K.: 2011, *ApJ* **735**, 46

Rädler, K.-H.: 1969, *Veroeffentlichungen der Geod. Geophys* **13**, 131

Rast, M. P., Ortiz, A., and Meisner, R. W.: 2008, *ApJ* **673(2)**, 1209

Reinhold, T. and Gizon, L.: 2015, *A&A* **583**, A65

Rempel, M.: 2005, *ApJ* **622**, 1320

Rheinhardt, M. and Brandenburg, A.: 2012, *AN* **333**, 71

Rüdiger, G.: 1989, *Differential Rotation and Stellar Convection. Sun and Solar-type Stars*, Akademie Verlag, Berlin

Saar, S. H. and Brandenburg, A.: 1999, *ApJ* **524**, 295

Scheiner, C.: 1630, *Rosa Ursina*

Schou, J., Antia, H. M., Basu, S., Bogart, R. S., Bush, R. I., Chitre, S. M., Christensen-Dalsgaard, J., di Mauro, M. P., Dziembowski, W. A., Eff-Darwich, A., Gough, D. O., Haber, D. A., Hoeksema, J. T., Howe, R., Korzennik, S. G., Kosovichev, A. G., Larsen, R. M., Pijpers, F. P., Scherrer, P. H., Sekii, T., Tarbell, T. D., Title, A. M., Thompson, M. J., and Toomre, J.: 1998, *ApJ* **505**, 390

Schrinner, M., Rädler, K.-H., Schmitt, D., Rheinhardt, M., and Christensen, U.: 2005, *AN* **326**, 245

Schrinner, M., Rädler, K.-H., Schmitt, D., Rheinhardt, M., and Christensen, U. R.: 2007, *GAFD* **101**, 81

Schwarzschild, K.: 1906, *Nach. Kgl. Ges. Wiss. Göttingen, Math-Phys.* **195**, p. 41

See, V., Jardine, M., Vidotto, A. A., Donati, J.-F., Boro Saikia, S., Bouvier, J., Fares, R., Folsom, C. P., Gregory, S. G., Hussain, G., Jeffers, S. V., Marsden, S. C., Morin, J., Moutou, C., do Nascimento, J. D., Petit, P., and Waite, I. A.: 2016, *MNRAS* **462**, 4442

Simard, C., Charbonneau, P., and Bouchat, A.: 2013, *ApJ* **768**, 16

Skumanich, A.: 1972, *ApJ* **171**, 565

Smolarkiewicz, P. K. and Charbonneau, P.: 2013, *J. Comp. Phys.* **236**, 608

Spruit, H.: 1997, *Mem. Soc. Astron. Italiana* **68**, 397

Steenbeck, M., Krause, F., and Rädler, K.-H.: 1966, *Zeitschrift Naturforschung Teil A* **21**, 369

Stein, R. F. and Nordlund, A.: 1989, *ApJ* **342**, L95

Stix, M.: 2002, *The Sun: An Introduction*, Springer, Berlin

Strugarek, A., Beaudoin, P., Charbonneau, P., Brun, A. S., and do Nascimento, J.-D.: 2017, *Science* **357**, 185

Tilgner, A., Belmonte, A., and Libchaber, A.: 1993, *Phys. Rev. Lett.* **47(4)**, R2253

Tuominen, I., Berdyugina, S. V., and Korpi, M. J.: 2002, *Astronomische Nachrichten* **323**, 367

Vainshtein, S. I. and Cattaneo, F.: 1992, *ApJ* **393**, 165

Vaughan, A. H. and Preston, G. W.: 1980, *PASP* **92**, 385

Vitense, E.: 1953, *ZAp* **32**, 135

Viviani, M., Käpylä, M. J., Warnecke, J., Käpylä, P. J., and Rheinhardt, M.: 2019, *arXiv e-prints* p. arXiv:1902.04019

Viviani, M., Warnecke, J., Käpylä, M. J., Käpylä, P. J., Olspert, N., Cole-Kodikara, E. M., Lehtinen, J. J., and Brandenburg, A.: 2018, *A&A* **616**, A160

Warnecke, J.: 2018, *A&A* **616**, A72

Warnecke, J., Käpylä, P. J., Käpylä, M. J., and Brandenburg, A.: 2014, *ApJ* **796**, L12

Warnecke, J., Rheinhardt, M., Tuomisto, S., Käpylä, P. J., Käpylä, M. J., and Brandenburg, A.: 2018, *A&A* **609**, A151

Wright, N. J. and Drake, J. J.: 2016, *Nature* **535**, 526

Wright, N. J., Drake, J. J., Mamajek, E. E., and Henry, G. W.: 2011, *ApJ* **743**, 48

Yoshimura, H.: 1975, *ApJ* **201**, 740

Zahn, J.-P.: 1991, *A&A* **252**, 179

Zhi-Chao, L., Gizon, L., Birch, A. C., Duvall, Jr., T. L., and Rajaguru, S. P.: 2018, *A&A* **619**, A99

Publications

Refereed publications

- **M. Viviani**, J. Warnecke, M. J. Käpylä, P. J. Käpylä, N. Olspert, E. M. Cole-Kodikara, J. J. Lehtinen and A. Brandenburg, 2018, A&A, 616, A160
- P. J. Käpylä, **M. Viviani**, M. J. Käpylä, A. Brandenburg and F. Spada, 2019, GAFD, 113, p.149-183.
- **M. Viviani**, M. J. Käpylä, J. Warnecke, P. J. Käpylä and M. Rheinhardt, Stellar dynamos in the transition regime: multiple dynamo modes and anti-solar differential rotation, ApJ, in press.

Conference contributions

Talks

1. Studying the transition from axi- to nonaxisymmetric dynamos using semi-global convection models, *14th Potsdam Thinkshop, Stellar magnetism: Challenges, Connections, and Prospects*, AIP, Potsdam, Germany, 12-16 June 2017.
2. The influence of rotation in the transition from axi-to nonaxisymmetric dynamos, *Rocks & Stars II Conference*, MPS, Göttingen, Germany, 13-16 September 2017.
3. Axi- to nonaxisymmetric dynamo transition in stellar models with varying rotation rate, *AG2017*, Göttingen, Germany, 18-22 September 2017.
4. Cyclic solutions and anti-solar differential rotation: can a Parker Dynamo Wave explain them?, *MHD Days and GdRI Dynamo Meeting*, Dresden, Germany, 26-28 November 2018.
5. Solar-like stars' models at increasing rotation rates: magnetic field, velocity field and helicities, *Solar Helicities in Theory and Observations: Implications for Space Weather and Dynamo Theory*, Stockholm, Sweden, 4-29 March 2019.
6. Dynamo transitions in simulations of Sun-like stars and understanding them, *IAU Symposium 354, Solar and Stellar Magnetic Fields: Origins and Manifestations*, Copiapo, Chile, 30 June - 6 July 2019.

Posters

1. Electrostatic waves in a weakly collisional plasma: analytical and numerical study, *Vlasovia 2016: Fifth International Workshop on the Theory and Applications of the Vlasov equation*, Copanello (Calabria), Italy, 30 May - 2 June 2016.

2. Studying the transition from axi- to nonaxisymmetric dynamos using semi-global convection models, *17th MHD Days*, Göttingen, Germany, 30 November - 2 December 2016.

3. Solar-like stars at various rotation rates: a comparison between observations and simulations, *IAU Symposium 340: Long-term datasets for the understanding of solar and stellar magnetic cycles*, Jaipur, India, 19-23 February 2018. Best poster award in the category “Solar and Stellar Dynamo”

Acknowledgements

I would like to thank the International Max Planck Research School for Solar System Science at the University of Göttingen (IMPRS) and the Max Planck Institute for Solar System Research (MPS) where I carried on my PhD work, for providing a stimulating environment.

A huge thank you goes to my supervisor, Maarit Käpylä, for guiding me in a field that was new to me when I started, for encouraging and setting deadlines when I needed a little push. You were not just a supervisor, but also a mentor and example to follow.

I would like to thank my other two Thesis Advisory Committee members, Robert Cameron and Ansgar Reiners, for advising me on how to contextualize my work with respect to other models and stellar observations.

Thank you to Ameya and Joern, that went through the thesis over and over again, to check the sense (and grammar) of the text. I would also like to thank Petri and Matthias for the help with the numerical part of my work. Thank you all for your support.

Thank you to the Band-Crew because with you all the Sun was shining even in the (many) cloudy days in Göttingen, and for making me feel home far away from home.

Lastly, I would like to thank my family, for always supporting my choices, even when they were leading me away from them.